# Dynamic Fracture of Adhesively Bonded Composite Structures Using Cohesive Zone Models

by Dhaval P. Makhecha

Dissertation submitted to the Faculty of the
Virginia Polytechnic Institute and State University
in partial fulfillment of the requirements for the degree of

Doctor of Philosophy
in
Aerospace Engineering

Rakesh K. Kapania (Committee Chair)
Eric R. Johnson Romesh Batra
Surot Thangjitham Raymond H. Plaut

September 5th, 2005
Blacksburg, Virginia

Keywords: dynamic fracture, adhesively bonded joints, composite, interface damage mechanics, extended finite element method, functionally graded material
Copyright ©2005, Dhaval P. Makhecha

# Dynamic Fracture of Adhesively Bonded Composite Structures Using Cohesive Zone Models

Dhaval P. Makhecha

## (ABSTRACT)

Using experimental data obtained from standard fracture test configurations, theoretical and numerical tools are developed to mathematically describe non-self-similar progression of cracks without specifying an initial crack. A cohesive-decohesive zone model, similar to the cohesive zone model known in the fracture mechanics literature as the Dugdale-Barenblatt model, is adopted to represent the degradation of the material ahead of the crack tip. This model unifies strength-based crack initiation and fracture-mechanics-based crack progression.

The cohesive-decohesive zone model is implemented with an interfacial surface material that consists of an upper and a lower surface that are connected by a continuous distribution of normal and tangential nonlinear elastic springs that act to resist either Mode I opening, Mode II sliding, Mode III sliding, or a mixed mode. The initiation of fracture is determined by the interfacial strength and the progression of the crack is determined by the critical energy release rate. The adhesive is idealized with an interfacial surface material to predict interfacial fracture. The interfacial surface material is positioned within the bulk material to predict discrete cohesive cracks. The interfacial surface material is implemented through an interface element, which is incorporated in ABAQUS using the user defined element (UEL) option.

A procedure is established to formulate a rate dependent model based on experiments carried out on compact tension test specimens. The rate dependent model is incorporated into the interface element approach to capture the unstable crack growth observed in experiments under quasi-static loading conditions. The compact tension test gives the variation of the fracture toughness with the rate of loading, this information is processed and a relationship between the fracture toughness and the rate of the opening displacement is established.

The cohesive-decohesive zone model is implemented through a material model to be used in an explicit code (LS-DYNA). Dynamic simulations of the standard test configurations

for Mode I (Double Cantilever Beam) and Mode II (End Load Split) are carried out using the explicit code. Verification of these coupon tests leads to the crash analysis of realistic structures like the square composite tube. Analyses of bonded and unbonded square tubes are presented. These tubes shows a very uncharacteristic failure mode: the composite material disintegrates on impact, and this has been captured in the analysis.

Disadvantages of the interface element approach are well documented in the literature. An alternative method, known as the Extended Finite Element Method (XFEM), is implemented here through an eight-noded quadrilateral plane strain element. The method, based on the partition-of-unity, is used to study simple test configuration like the three-point bend problem and a double cantilever beam. Functionally graded materials are also simulated and the results are compared to the experimental results available in the literature.

# Dedication

***To my parents Pravin and Ila Makhecha for their love and support***

# Acknowledgments

I would like to thank my advisor Dr. Rakesh Kapania for his constant support and patience, invaluable guidance and excellent suggestions. Also I would like to thank Dr. Eric Johnson for the numerous discussions we have had on both technical and non technical issues. Both of them have met with me on a regular basis to discuss and refine the theoretical and computational aspects of this research. I take this opportunity to thank Dr. Romesh Batra, Dr. Raymond Plaut and Dr. Surot Thangjitham for serving on my committee and for the technical suggestions to this dissertation.

This research has been sponsored, in part, by the Automotive Composite Consortium's Department of Energy Cooperative Agreement No. DE-FC05-95OR22363. Such support does not constitute an endorsement by the Department of Energy of the views expressed herein. I wish to thank Dr. Naveen Rastogi, the project montior, for the technical discussions held with him.

I am grateful to the research group of Dr. David Dillard from the Department of Engineering Science and Mechanics (ESM) for providing the experimental results and the invaluable discussions over these experiments. I thank Vinay Goyal for his technical assistance with the finite element implementation using ABAQUS.

On the computational side I would like to express my sincere thanks to the complete computational staff, especially Luke Scharf and Jeffery Kuhn who have provided the necessary computational tools in spite of my constant nagging. I thank the entire administrative staff of the Aerospace and Ocean Engineering Department, for taking care of all the paper work especially Ms. Williams and Gail.

I express my thanks to Dr. Manickam Ganapathi, my advisor during my Master's in India, for introducing me to research and encouraging me to pursue my doctorate studies

My friends have contributed considerably by supporting me and helping me in the last four years at Blacksburg. I would like to extend my thanks particularly to Suhas Subramanya, Sameer Mulani, Prateep Chatterjee, Konda Reddy, Ramya Ramanath and Omprakash Seresta. I am indebted to Dr. Edwin Robinson and Valarie Robinson, who have been more than friends, for their hospitality, support, advice and treating me like family.

I thank my family who has given me infinite moral support and encouragement over the years. I just can't begin to thank my parents enough for everything they have done for me. I extend my thanks to my sisters Meeta and Vishakha along with their husbands Meghadri and Shrihari, and my nephew Chinamy, for being there for me whenever I needed them.

# Contents

**Title Page** i

**Abstract** ii

**Dedication** iv

**Acknowledgments** v

**Table of Contents** vii

**List of Figures** viii

**List of Tables** ix

**1 Introduction** 1

1.1 Bonded Composite Structures . . . . . 1

1.2 Background . . . . . 3

1.3 Adhesive Characterization Tests for Fracture . . . . . 7

1.3.1 Double Cantilever Beam (DCB) . . . . . 7

1.3.2 End Load Split (ELS) . . . . . 8

1.3.3 Stick-Slip Behavior . . . . . 10

1.4 Cohesive Zone Model . . . . . 15
1.4.1 Constitutive Laws . . . . . 20
1.4.2 Fracture Tests for CZM Modeling . . . . . 23
1.5 Computational Difficulties . . . . . 23
1.5.1 Extended Finite Element Method . . . . . 25
1.6 Objectives of the Dissertation . . . . . 28
1.7 Outline of the Dissertation . . . . . 29

**2 Rate Independent CZM Modeling** **32**
2.1 Introduction . . . . . 32
2.2 Static Fracture Analysis . . . . . 33
2.2.1 Formulation . . . . . 34
2.2.2 Validation . . . . . 51
2.3 Behavior of Polymer Based Adhesives . . . . . 57
2.4 Dynamic Fracture Analysis . . . . . 65
2.4.1 Formulation . . . . . 66
2.4.2 Validation . . . . . 68
2.5 Detailed Modeling of Bulk Adhesive Including Dynamic Effects . . . . . 69
2.6 Difficulties in Detailed Modeling of Bulk Adhesive . . . . . 72

**3 Rate Dependent CZM Modeling** **74**
3.1 Introduction . . . . . 74
3.2 Compact Tension Tests . . . . . 77
3.3 Compact Tension Test Simulation in ABAQUS . . . . . 81
3.3.1 Finite Element Model for CT . . . . . 83

3.4 Formulation of Rate Dependent Models . . . . . 87
3.4.1 Rate Dependent Model I ($\Delta_c = F(\dot{\Delta})$) . . . . . 88
3.4.2 Rate Dependent Model II ($\beta = F(\dot{\Delta})$) . . . . . 90
3.5 Implementation of Rate Dependent Model **I** in ABAQUS . . . . . 92
3.6 Results and Discussion . . . . . 96

**4 Dynamic Fracture Using Explicit Methods 99**
4.1 Introduction . . . . . 99
4.2 User Defined Material (UMAT) . . . . . 100
4.3 Formulation . . . . . 103
4.4 A Beginner's Guide to Writing UMAT in LS-DYNA . . . . . 104
4.5 Rate Dependent Model . . . . . 107
4.6 Mode I Results . . . . . 108
4.6.1 Aluminum DCB . . . . . 110
4.6.2 Composite DCB . . . . . 111
4.7 Mode II Simulations . . . . . 118

**5 Modeling of an Unbonded/Bonded Square Composite Tube 124**
5.1 Introduction . . . . . 124
5.2 Square Tubes . . . . . 126
5.3 LS-DYNA Modeling . . . . . 129
5.3.1 Circular Tubes . . . . . 129
5.3.2 Square Composite Tubes . . . . . 132
5.4 Unbonded Composite Square Tubes Tested at ORNL . . . . . 138
5.5 Bonded Composite Square Tubes Tested at ORNL . . . . . 144

**6 Fracture Analysis Using Extended Finite Element (X-FEM) 149**

6.1 Introduction . . . . . 149

6.2 Formulation . . . . . 152

6.2.1 Shape functions based on the partitions of unity . . . . . 154

6.2.2 Discontinuities in the enhanced basis . . . . . 156

6.2.3 Variational Formulation . . . . . 157

6.2.4 Discretized Weak Equations . . . . . 160

6.2.5 Traction-Separation Relations . . . . . 162

6.3 Implementation . . . . . 164

6.4 Numerical Examples . . . . . 166

6.4.1 Three-point bending test . . . . . 166

6.4.2 Single-edge Notched (SEN) beam . . . . . 167

6.4.3 Dynamic Fracture of Functionally Graded Material . . . . . 171

6.4.4 Double Cantilever Beam . . . . . 176

**7 Concluding Remarks and Future Work 184**

7.1 Concluding Remarks . . . . . 185

7.1.1 Interface element approach for CZM . . . . . 185

7.1.2 Material Definition approach for CZM . . . . . 187

7.1.3 Extended Finite Element . . . . . 188

7.2 Future Work . . . . . 189

7.2.1 Stochastic Response . . . . . 189

7.2.2 Extended Finite Element Method . . . . . 190

**Biblography 192**

**Vita** **206**

# List of Figures


1.1 Tubular composite structure . . . . . 4

1.2 Deformed shape of the square tubular composite structure. . . . . 4

1.3 Cross section of a bonded square composite tube. . . . . 5

1.4 Modes of Failure. . . . . 6

1.5 DCB configuration. . . . . 7

1.6 DCB quasi-static testing in Instron in Adhesion Science Laboratory, ESM. 9

1.7 DCB dynamic testing using a drop tower in Adhesion Science Laboratory, ESM . . . . . 9

1.8 Schematic representation of the ELS . . . . . 11

1.9 Experimental setup for the dynamic ELS in Adhesion Science Laboratory, ESM. . . . . 11

1.10 Tip reaction force history for an aluminum DCB bonded using LESA at an applied opening displacement of 0.1 mm/min. . . . . 12

1.11 Computed crack length for the aluminum DCB bonded with LESA. . . . 13

1.12 Schematics of typical non-monotonic fracture toughness-crack velocity curve. 15

1.13 Tip reaction force history for a aluminum DCB bonded using SIA with an opening displacement of 1 mm/min. . . . . 16

1.14 Crack length for the DCB bonded with SIA with an opening displacement of 1 mm/min . . . . . 16

1.15 Adhesive layer modeled as discrete continuous springs . . . . . 18

1.16 Bilinear traction displacement constitutive law for the spring . . . . . 19

1.17 Bilinear traction displacement constitutive law for the spring . . . . . 21

1.18 Comparison between Reversible and Irreversible laws . . . . . 22

1.19 Possible crack paths at a given node with bulk and interface modeling . . 26

1.20 Body $\Omega$ crossed by a discontinuity $\Gamma_d$ . . . . . 27

2.1 Interface surface deformation . . . . . 36

2.2 Traction components acting at the interface midsurface. . . . . 36

2.3 Interfacial surface traversing a body of material. . . . . 42

2.4 Loading conditions of the DCB configuration. . . . . 52

2.5 Finite element model of the DCB configuration. . . . . 54

2.6 Comparison of the load history for DCB bonded with LESA adhesive. . . 56

2.7 Crack growth history for DCB bonded with LESA adhesive. . . . . 56

2.8 Tip reaction force history for a aluminum DCB bonded using SIA with an opening displacement of 1 mm/min . . . . . 59

2.9 Crack length for the DCB bonded with SIA with an opening displacement of 1 mm/min. . . . . 59

2.10 Traction-Displacement law for different values of $\beta$. . . . . 61

2.11 Reaction histories for different values of $\beta$. . . . . 61

2.12 Reaction histories for different values of $\beta$. . . . . 62

2.13 Arrangement of the interface element and the bulk element used to model the adhesive. . . . . 64

2.14 Possible crack growth paths with detailed modeling of adhesive. . . . . 64

2.15 Reaction histories obtained using detailed modeling of the adhesive. . . . 65

2.16 Dynamic crack growth comparison with semi-analytical results. . . . . 69

2.17 Tip reaction history compared to experimental load histories. . . . . 71

2.18 Oscillations in tip reaction when crack growth occurs. . . . . 71

2.19 Snapshots taken at an interval of $1\mu s$ to show the crack jumps. . . . . 72

3.1 Schematics of typical non-monotonic fracture toughness-crack velocity curve. 76

3.2 Working drawing of the compact tension test specimen prepared at Oak Ridge National Laboratory (ORNL), all dimensions are in mm. . . . . 78

3.3 Photographs of the compact tension test specimen before and after testing. 79

3.4 Fracture toughness variation obtained using the compact tension test at ORNL. . . . . 80

3.5 Log-Log plot of the fracture toughness $K$ with the test speed, along with the polynomial fit. . . . . 81

3.6 Placement of the interface element in the compact tension test in a finite element simulation performed using ABAQUS®. . . . . 83

3.7 Maximum opening velocity measured at Gauss points in the compact tension test simulations. . . . . 85

3.8 Data for $G_{I_c}$ as function of $\dot{\Delta}$ obtained from finite element simulation of a compact tension test and the curve fit. . . . . 87

3.9 Rate dependent model I with $\Delta_c = F(\dot{\Delta})$. . . . . 89

3.10 $\beta$ as a function of $G_{I_c}$. . . . . 90

3.11 Rate Dependent Model II ($\beta = F(\dot{\Delta})$). . . . . 91

3.12 Effect on the brittleness parameter in the rate dependent model **II**. . . . 92

3.13 Surface plot of the derivative term for rate dependent model **I**. . . . . 95

3.14 Surface plot of the derivative term for rate dependent model **II**. . . . . 95

3.15 Comparison between experimental and numerical results of the tip reaction force for an aluminum DCB. . . . . 97

4.1 Calculation of the opening displacements in a plane strain element. . . . 102

4.2 Reference orientation for the three fracture modes in a standard brick element. . . . . 102

4.3 DCB dynamic testing using a drop tower in Adhesion Science Laboratory, ESM. . . . . 109

4.4 Crack length comparison for aluminum DCB in a drop tower test. . . . . 112

4.5 Crack length for a composite DCB test in the drop tower. . . . . 113

4.6 Snapshots of the composite DCB simulation a) t = 0s b) t = 0.01s. . . . 114

4.7 Tip displacement observed from test. . . . . 116

4.8 Tip displacement observed from test and a linear regression fit. . . . . 116

4.9 Crack length comparison for composite DCB. . . . . 117

4.10 The ELS configuration for Mode II testing. . . . . 118

4.11 ELS specimen in a drop tower. . . . . 119

4.12 Snapshots of the ELS in a drop tower. . . . . 121

4.13 Snapshots of the ELS simulation in LS-DYNA. . . . . 122

4.14 Crack growth history from the ELS simulation using LS-DYNA and a rate independent CZM law. . . . . 123

5.1 Deformed specimens corresponding to collapse Modes I-III: (a) Mode I; (b) Mode II; (c) Mode III. . . . . 127

5.2 Deformed specimen of tube tested at ORNL. . . . . 128

5.3 Geometry of the circular tube. . . . . 130

5.4 Initial champering for the circular tube at the crushing end. . . . . 131

5.5 Deformation mode of the circular tube from two numerical simulations. . 132

5.6 Cross section of the composite square tubes. . . . . 133

5.7 Snapshots of the square composite tube under dynamic load. . . . . 139

5.8 Snapshots of the square composite tube under dynamic load in LS-DYNA. 142

5.9 Comparison of force histories for the unbonded tube under an impact velocity of 4 m/s. . . . . 143

5.10 Schematic diagram of the bonded square composite tube. . . . . 144

5.11 Approximated overlap joint for numerical analysis in a bonded tube. . . . 145

5.12 Force history for the bonded tube under an impact velocity of 4 m/s. . . 147

6.1 Body $\Omega$ crossed by a discontinuity $\Gamma_d$. . . . . 152

6.2 Elements crossed by discontinuity and the enhanced nodes. . . . . 164

6.3 Geometry of three-point bend test. All dimensions in millimeters. . . . . 167

6.4 Crack path for a three-point bending test. . . . . 168

6.5 Load-displacement response for three-point bending test. . . . . 168

6.6 Single-Edge Notched (SEN) beam. All dimensions in millimeters. . . . . 169

6.7 Crack path for an SENB. The crack is shown by a heavy red line. . . . . 170

6.8 Load-opening displacement for SENB for experimental and numerical results 170

6.9 Property variations in graded foam with monotonic volume fraction variation. . . . . 172

6.10 Crack growth comparison in a graded foam specimen under impact loading. 174

6.11 Variation of elastic modulus and elastic impedance along the specimen height. . . . . 175

6.12 Crack growth comparison for conventional and graded sandwich beams. . 177

6.13 Aluminum DCB bonded with LESA adhesive. Adhesive thickness 0.8mm. 178

6.14 Reaction forces history for aluminum DCB bonded with LESA. . . . . 179

6.15 Crack path with functionally graded properties for the adhesive. Adhesive thickness 0.8mm. . . . . 181

6.16 Crack growth history for a aluminum DCB simulated under dynamic conditions. . . . . 182

# List of Tables


2.1 Mechanical properties for aluminum. . . . . 54

2.2 Interface properties for the LESA adhesive. . . . . 54

2.3 Interface properties for the SIA adhesive. . . . . 60

4.1 Additional arguements in LS-DYNA. . . . . 105

4.2 Mechanical properties for aluminum for dynamic testing. . . . . 110

4.3 Material properties for the SIA adhesive as defined in the UMAT. . . . . 110

4.4 Material properties for composite adherends (11-ply symmetric). . . . . 113

5.1 Comparison of peak loads and energy for dynamic tube crush of aluminum circular tubes. . . . . 131

5.2 Geometric and material data for the square tubes. . . . . 133

5.3 Geometric and material data for the square tubes. . . . . 134

5.4 Comparison of peak loads and energy for dynamic tube crush of square composite tubes. . . . . 138

5.5 Material data for the square woven composite tubes. . . . . 141

5.6 Material properties for the SIA adhesive as defined in the UMAT. . . . . 146

5.7 Peak loads for the bonded and unbonded square composite tubes. . . . . 148

# Chapter 1

# Introduction

## 1.1 Bonded Composite Structures

Adhesively bonded composite structures are becoming increasingly popular in the aerospace and automotive industries. Composite materials are very attractive due to their high strength to weight and high stiffness to weight ratios. Their use can significantly reduce structural weight of the vehicle. However composite materials tend to be brittle, and are consequently vulnerable to impact; more so than the metallic components, which develop tell-tale signs of damage under impact loads, and can be replaced. Due to their ductility, the metallic structures can absorb a considerable amount of impact energy. The impact induced damage in composites, on the other hand, is often hidden within the laminate and can greatly reduce both the strength and the stiffness of the given structure.

Joints in composite structures can be mechanically fastened or bonded with adhesives. Mechanical fastening results in considerable stress concentration and relatively poor fatigue properties in addition to increasing the weight and the manufacturing cost. Adhesive bonding can provide an improved fatigue life, and potentially lower life-cycle cost due to reduced maintenance requirements and part count, eliminate drilling and machining of components, enhance damping characteristics, and an increase flexibility in design and also reduce weight ( Eckold (1994), Ashcroft *et al.* (2001)). Adhesives have been, for the most part, used for secondary structures or for primary structures under light loads. Now, however, adhesives are increasingly being used for structures subjected to heavy loads ( Potter (2001)). Most joint design procedures aim for failure of the adherends at the lowest static failure load, so that the bonded region is not the weak link. Failure of laminated composite adherends is either by intralaminar or interlaminar mechanisms. Intralaminar failures constitute the micro-mechanical mechanisms such as fiber-breakage, matrix cracking, and debonding of the fiber-matrix interface. Interlaminar failure is by delamination.

To achieve improved energy absorption of lightweight vehicle structures under impact loading, the joint should not be the weak link so that the energy absorbed by the impact occurs by crushing of adherends. The design against joint failure requires the capability to predict the failure of the joint. A literature survey showed that there are very few numerical studies conducted on the progressive degradation response of adhesively bonded composite structures under impact loads.

## 1.2 Background

The objective of this dissertation is the analysis and computational modeling of the response and failure of adhesively bonded automotive composite structures under impact loads. It is part of a project funded by the Department of Energy (DOE) under the United States Automotive Materials Partnership. The partnering organization with DOE is the Automotive Composites Consortium (ACC). The ACC members primarily consist of personnel from three major US automobile companies: Daimler-Chrysler, Ford and General Motors Corporations. Monitoring the technical work of the project are the Energy Management Working Group (EMWG) and the Joining Group of the ACC. The second part of this project is the experimental characterization of the dynamic fracture properties of bonded joint configurations under various mode mixities. The experimental part is being conducted in the Adhesion Science Laboratory, Engineering Science and Mechanics Department, under the direction of Dr. Dillard. Additionally, experimental characterization of the bulk adhesive material is being conducted at the Oak Ridge National Laboratory (ORNL) of the Department of Energy.

The generic composite structure of interest to EMWG is a thin-walled tube, which is considered representative of a component to be used in an automobile to absorb energy under crash. The aim of energy management is to characterize and improve the energy

absorption per unit mass of a tube under impact loads. A tube with a square cross section under axial impact is shown in Figure 1.1. The graphic in Figure 1.1 is from a finite element model of a composite tube with a square cross section that does not contain an adhesive joint. The dimensions and material properties of the textile composite tube are those of a test selected by the ACC. The simulation of the dynamic response of this tube without a joint is relatively easy for any experienced user of commercial finite element packages, namely ABAQUS and LS-DYNA. The impact simulation depicted in the figure was carried out in LS-DYNA, and Fig. 1.2 shows the deformed state of the crushed tube. However, in practice a built-up structure will contain joints. So a bonded tubular section is the focus of this study to compare its response to the unbonded counterpart. The discontinuity at the bonded joint causes stress raisers, and the interface between the adhesive and the composite wall is another possible location of fracture in the structure. Fig. 1.3 shows the cross section of the bonded square composite tube. For modeling the adhesive one needs to know the mechanical properties of the adhesive, its maximum strength, and its fracture characteristics as represented by the critical energy release rates, denoted by $G$ (after A. A. Griffith), in the three basic modes of fracture shown in Fig. 1.4. Numerical simulations of these fracture tests are necessary to verify the fracture model implemented in the simulation. These fracture tests and their simulations are discussed, but the details of the test procedures and the finer points of the experiments are omitted as they are well documented in the Master's Thesis of Simón (2004)

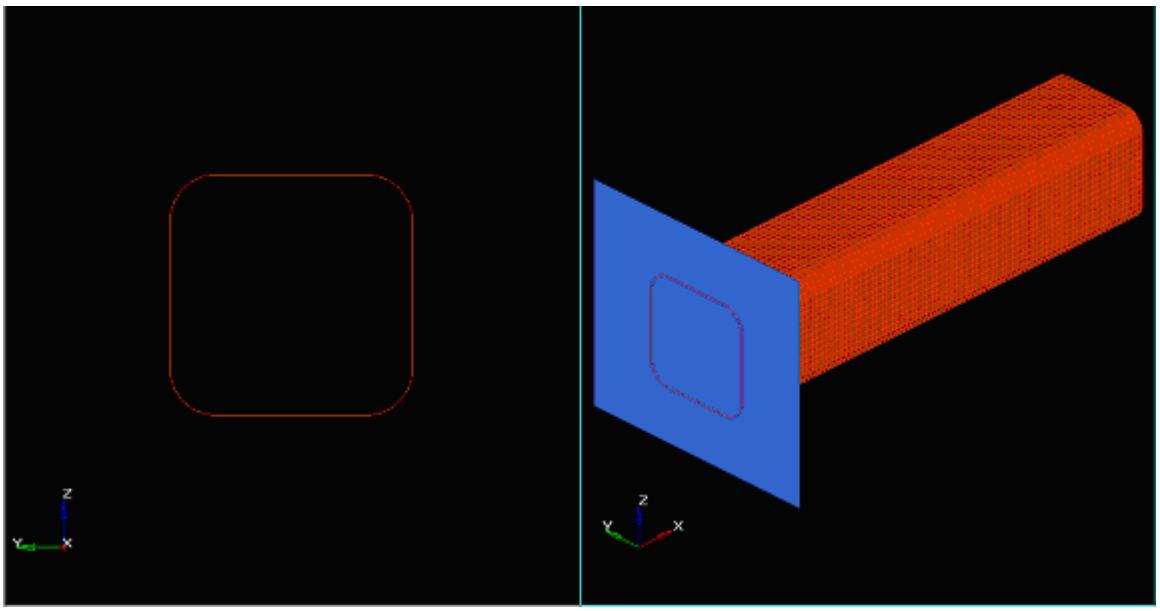

Figure 1.1: Tubular composite structure

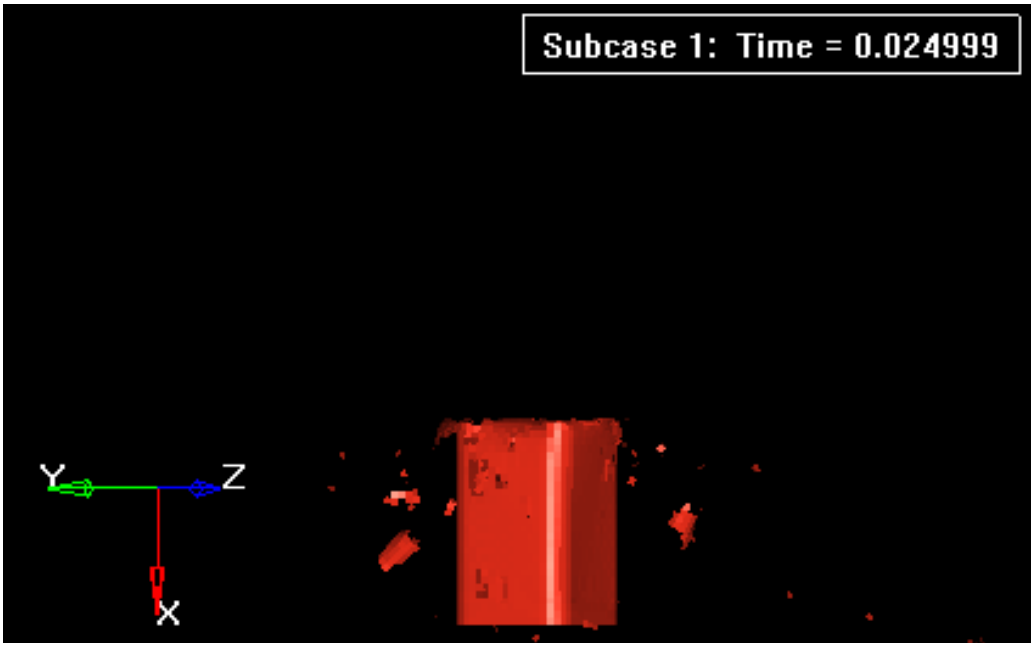


Figure 1.2: Deformed shape of the square tubular composite structure.

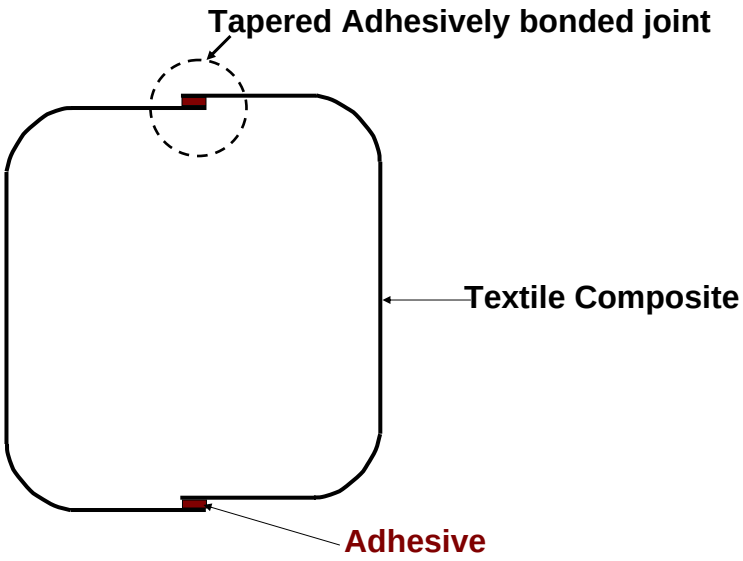


Figure 1.3: Cross section of a bonded square composite tube.

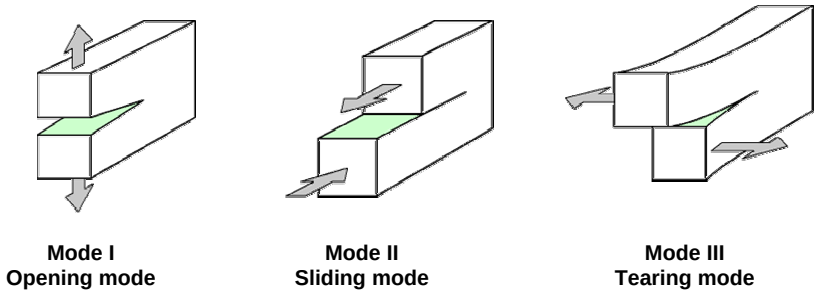


Figure 1.4: Modes of Failure.

The materials used for this study were the ones specified by the Automotive Composite Consortium (ACC). ACC specified a textile composite for the adherends manufactured by Advanced Composites Group. It is designated as MTM49/CF0501 and uses the Toray fiber T300B-40B embedded in an epoxy resin with a resin content of 42% . The specified adhesive is a two-part epoxy produced by Sovereign Speciality Chemical, Inc, and is designated SIA PL731. Occasionally verification of our numerical models with the

response of other bonded joints reported in the literature that use different adhesives and adherends are discussed.

## 1.3 Adhesive Characterization Tests for Fracture

The properties of the adhesive need to be determined in all the three modes of fracture and also under mixed mode conditions. This section will discuss briefly the tests and the qualitative results for the SIA adhesive. First the Double Cantilever Beam (DCB) test used for determining properties under Mode I fracture will be discussed and then the End Load Split (ELS) will be discussed. The peculiar observations made during these tests and the effect it has on the numerical modeling will be presented.

### 1.3.1 Double Cantilever Beam (DCB)

The DCB test configuration is recommended by ASTM Standard D3433 ( ASTM (1999)) to determine the fracture characteristic of bonded joints. A schematic figure of the DCB is shown in the Fig. 1.5. The test can be conducted under both quasi-static loading and dynamic loading and has been performed earlier by many researchers such as Blackman and co-workers ( Blackman *et al.* (1995), Blackman *et al.* (1996), Blackman *et al.* (1996)). An Instron machine was used for the quasi-static loading and the drop tower was used for dynamic studies of the DCB. Photographs of the test specimens in the

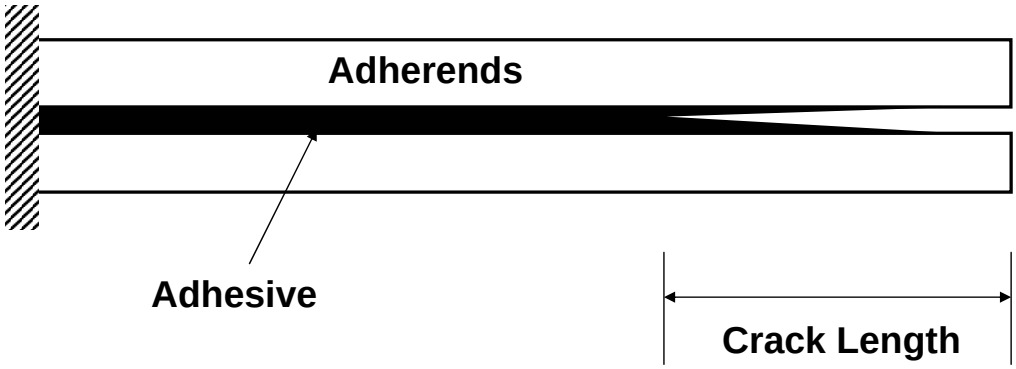


Figure 1.5: DCB configuration.

Instron setup and the drop tower apparatus (located in the Adhesion Science Laboratory in the ESM department) are shown in Fig. 1.6 and Fig. 1.7 respectively. Under the static test conditions the reaction force at the tip is measured along with the crack length. The force measurement is quite erratic under the dynamic condition and is generally not reported for these experiments. The critical energy release rate is estimated using the following equation:

$$G_{I_c} = \frac{12\ F\ P_c^2\,(a + \chi_1\ h)^2}{B^2\ h^3\ E} \tag{1.1}$$

where $F$ is a correction factor for stiffening due to the end loading blocks, $P_c$ is the critical load at the initiation of crack growth, $a$ is the crack length, $B$ is the width of the specimen, $h$ is the thickness of one arm, $E$ is the modulus of elasticity, and the variable $\chi_1$ accounts for the root rotation and deflection at the crack tip. The value of $\chi_1$ is deduced by taking the intercept of a plot of $(C/N)^{1/3}$ versus crack length, where $C$ is the compliance of the DCB specimen and $N$ is the end-block correction factor (Blackman *et al.* (1995)).

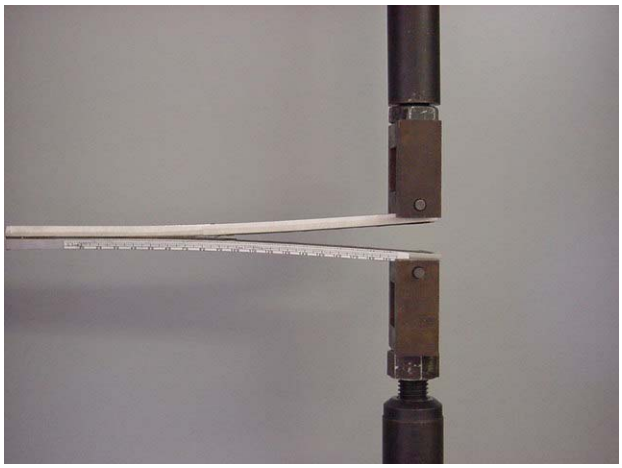

Figure 1.6: DCB quasi-static testing in Instron in Adhesion Science Laboratory, ESM.

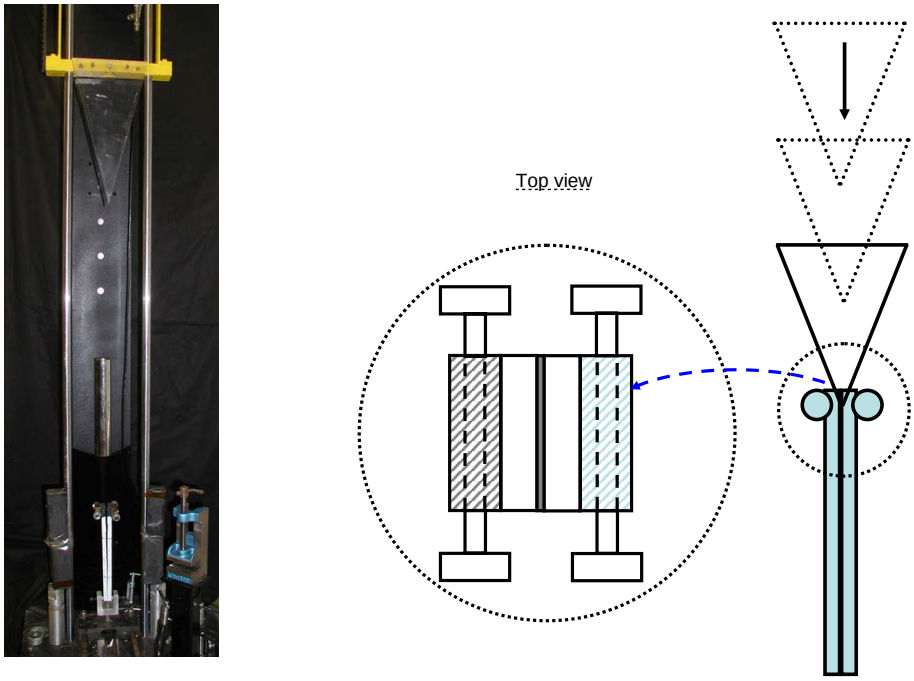


Figure 1.7: DCB dynamic testing using a drop tower in Adhesion Science Laboratory, ESM

### 1.3.2 End Load Split (ELS)

The pure forward shearing mode characterized as the second mode quite often significantly contributes to the fracture process. This type of loading is characterized by the idea of two plates sliding past one another, often causing a hackled fracture pattern within the adhesive as a result of the shear deformations. The End Load Split is quite often used to characterize the properties in the second mode; the other test used is the end-notched flexure (ENF). In this study the Adhesion Science Laboratory at Virginia Tech used the ELS for determining the Mode II properties. Figure 1.8 shows a schematic representation of the ELS configuration, and Fig. 1.9 shows the experimental setup used for the impact testing. The discussion of the ELS tests is brief since the experimental tests are still in progress as of the time this is written.

### 1.3.3 Stick-Slip Behavior

The knowledge of the behavior of the adhesive under different types of loading is very important for formulating a numerical constitutive model. Propagation of the crack through the adhesive may be stable or unstable.

Crack growth is considered to be stable if the rate of change of crack length with respect to time under constant load rate is fairly constant, that is, the crack velocity is fairly constant and it does not display any sudden jumps with respect to load history. In a static test where the tip reaction forces are measured, the force reduces slowly once the

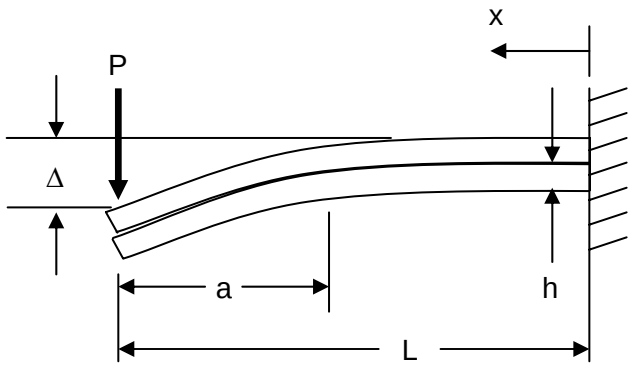


Figure 1.8: Schematic representation of the ELS

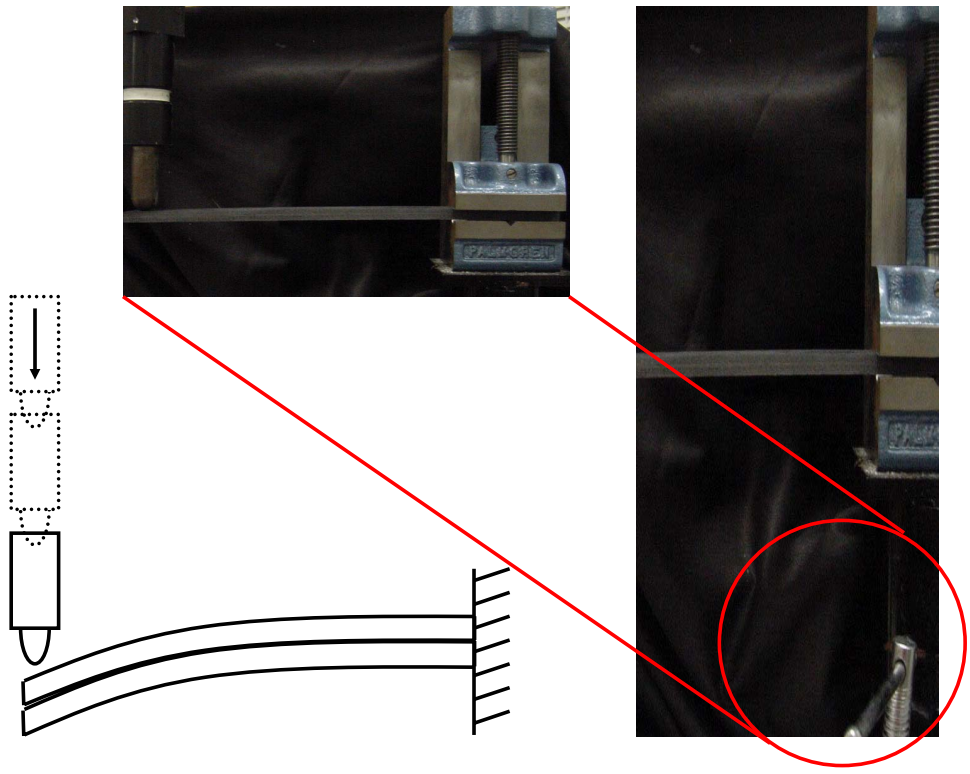

Figure 1.9: Experimental setup for the dynamic ELS in Adhesion Science Laboratory, ESM.

degradation of the adhesive has started and it shows no sudden jumps and follows a trend similar to the analytical solution given by Linear Elastic Fracture Mechanics (LEFM) as

$$\Delta_o = \frac{2}{3\ E\ I\ P^2} \left(B\ G_c\ E\ I\right)^{3/2} \tag{1.2}$$

The experiments showed that LESA, the adhesive marketed by DOW Automotive, degraded progressively and exhibited a steady crack growth. A quasi-static test was carried out using the Instron machine on an aluminum DCB at an opening velocity of $0.1 mm/min$ with LESA used for bonding. Reaction forces were measured at the tip and Fig. 1.10 shows this measurement. As can be seen from the figure, the later portion of the curve

Figure 1.10: Tip reaction force history for an aluminum DCB bonded using LESA at an applied opening displacement of 0.1 mm/min.

in which the force starts to reduce is more or less steadily reducing. Figure 1.11 shows

the numerically computed crack length as a function of time. This curve also does not display any significant jumps in the crack length.

An unstable crack growth, on the contrary, displays sudden jumps in crack length,

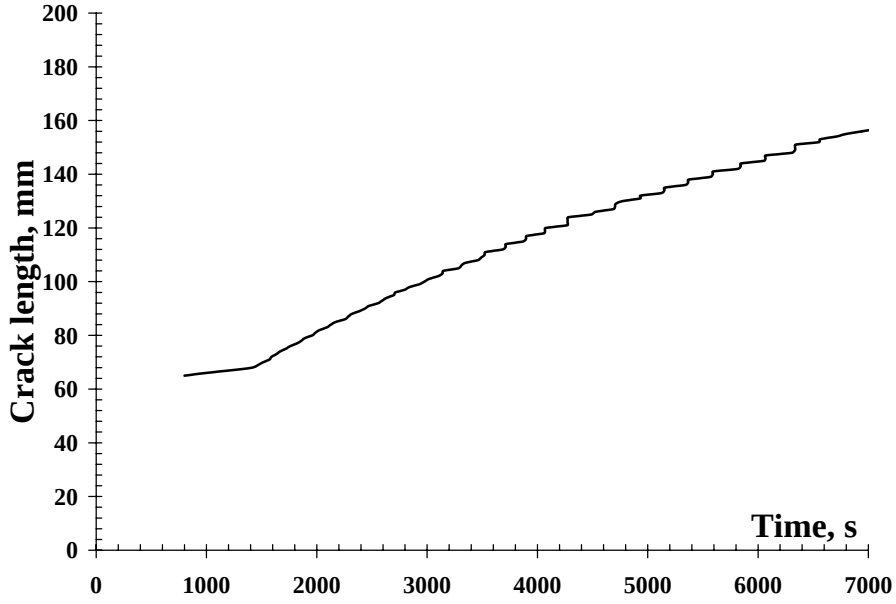


Figure 1.11: Computed crack length for the aluminum DCB bonded with LESA.

and therefore a sudden drop in the tip reaction force. This type of behavior has mostly been observed in polymer based adhesives. Physically the way the structure debonds can be segregated into two phases known as the arrest and propagation of cracks. The propagation of the crack is quite fast and this is followed by a phase where the crack tip is stationary and this phenomenon is also called the "Stick-Slip" behavior. Stick-slip fracture can occur on both microscopic and macroscopic scales and is characterized by an oscillatory crack tip velocity and crack growth jumps. Microscopic level stick-slip behavior indicates that the size of the crack jump increments is comparable with the

size of the fracture process zone and the crack tip oscillations and their effects are usually "averaged" out in the experiments. This type of oscillation have been studied by Fineberg *et al.* (1991) and Fineberg *et al.* (1992). Stick-slip behavior on a macroscopic level is the case where the size of the crack jump increments are much larger than the size of the fracture process zone and cannot be easily "averaged" out in experiments. Various groups over the years have observed these kind of macroscopic jumps in different polymers and polymeric adhesives. Prominent contributions are from Atkins *et al.* (1975), Hakeem and Phillips (1979) and Ravi-Chandar and Balzano (1988) who studied the stick-slip behavior in polymethylmethacrylate (PMMA). Leevers (1986) studied thermosetting polyesters. Epoxy resins were studied by Selby and Miller (1975), Kobayashi and Dally (1977), Yamini and Young (1977), Phillips *et al.* (1978), Kinloch and Williams (1980) and Scott *et al.* (1980). Stick-slip behavior was also studied in the peeling test of polymeric adhesives by Gardon (1963), Aubery *et al.* (1969), Aubrey (1978), Maugis and Barquins (1987), Kim and Kim (1988), Kinloch and Yuen (1989a) and Kinloch and Yuen (1989b).

Stick-slip behavior on a macroscopic scale cannot be interpreted using the fracture process zone model since the size of the crack jump increment is significantly larger than the process zone length. This behavior has been associated with the negative slope region of a macroscopic non-monotonic fracture toughness versus velocity slope. A schematic of non-monotonic fracture toughness-velocity curve is shown in Fig. 1.12. A brief review of the analytical methods used to solve this problem and a study of the double torsion test

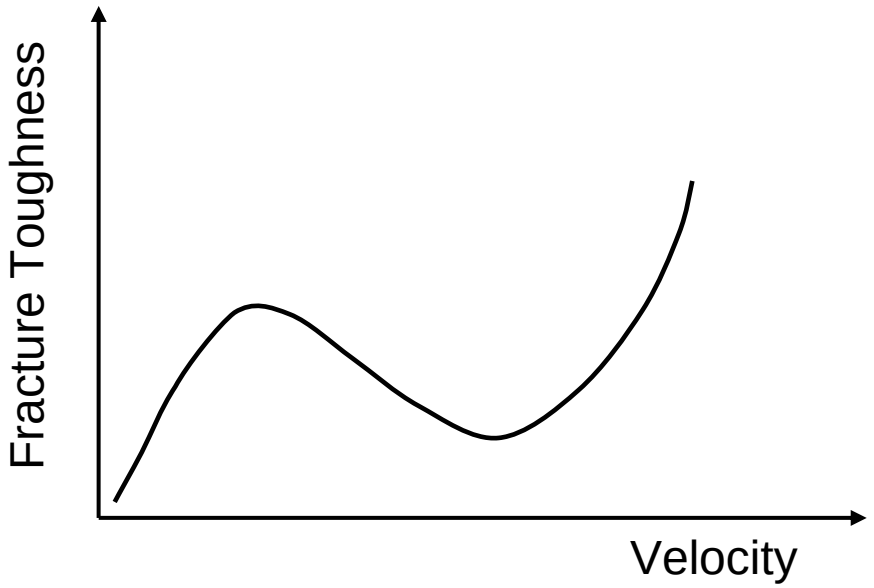


Figure 1.12: Schematics of typical non-monotonic fracture toughness-crack velocity curve.

specimen using polymers has been given by Webb and Aifantis (1995).

The SIA adhesive used in this study is a polymer based adhesive, and it displays the stick-slip behavior under a quasi-static DCB test. A quasi-static test under a loading rate of 1 $mm/min$ was carried out at the adhesion science lab in ESM and Fig. 1.13 shows the tip reaction force measured during this test. Figure 1.14 shows the crack length plotted during the course of the experiments. Sudden jumps observed in both the force plot and the crack length plot are typical for unstable crack growth. One reason for this kind of behavior may be because the ultimate failure strength of some materials is rate sensitive as was found by Lankford (1981). To further investigate the presence of this kind of behavior in the SIA adhesive, Oak Ridge National Laboratory (ORNL) conducted

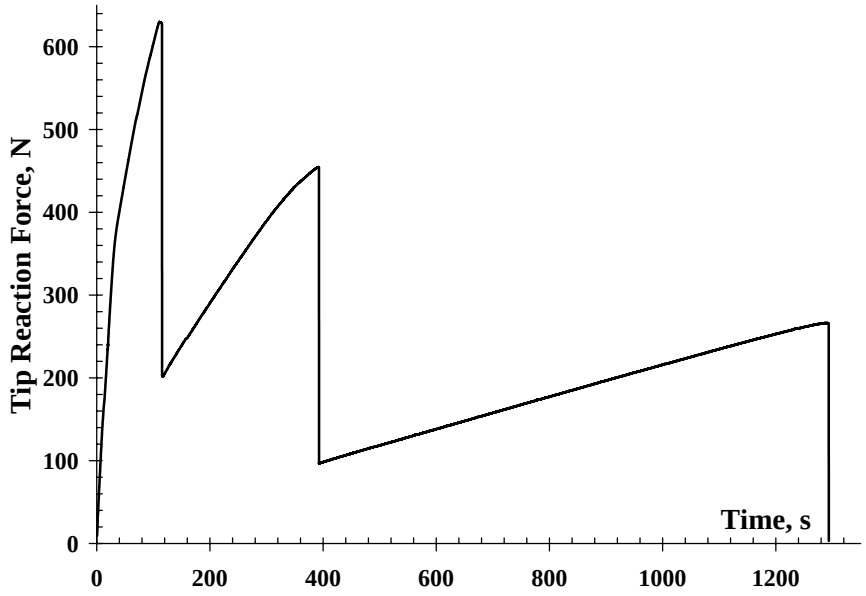


Figure 1.13: Tip reaction force history for a aluminum DCB bonded using SIA with an opening displacement of 1 mm/min.

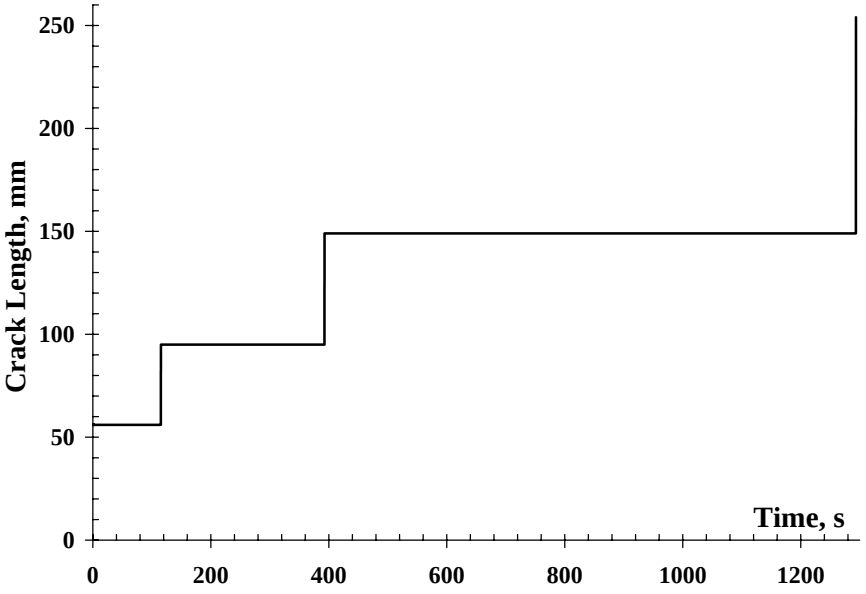


Figure 1.14: Crack length for the DCB bonded with SIA with an opening displacement of 1 mm/min

a series of compact tension tests to determine the fracture toughness at different testing rates. The specimens were fabricated using the SIA adhesive. The results indicated a negative slope, consistent with what has been reported in the literature.

## 1.4 Cohesive Zone Model

Cohesive zone modeling has been emerging as the alternative to linear elastic fracture mechanics. The technique is developed by extending and combining the concepts of continuum mechanics and linear elastic fracture mechanics. In this approach the crack propagation is studied between two surfaces, *i.e.* the interface, by using a continuous distribution of unconnected normal and tangential springs. Based on the concept of continuum modeling, the interfacial damage mechanics takes into account the irreversible damage consistent with the laws of thermodynamics. The advantage over the continuum modeling is the ability of the technique to allow two or more material points to coexist in the same location of the undeformed body. A difference between the two techniques is the formulation: the continuum model formulates the work conjugacy based on the stresses and strains, whereas tractions and displacement jumps are used to calculate the work conjugacy in the interfacial damage mechanics.

The problem of the interface was solved under the assumption of a thin adhesive layer using the continuum approach by Wang (1980), Wu (1987) and Allix and Ladevèze (1992). The interface approach would treat the adhesive layer as an idealized interfacial surface

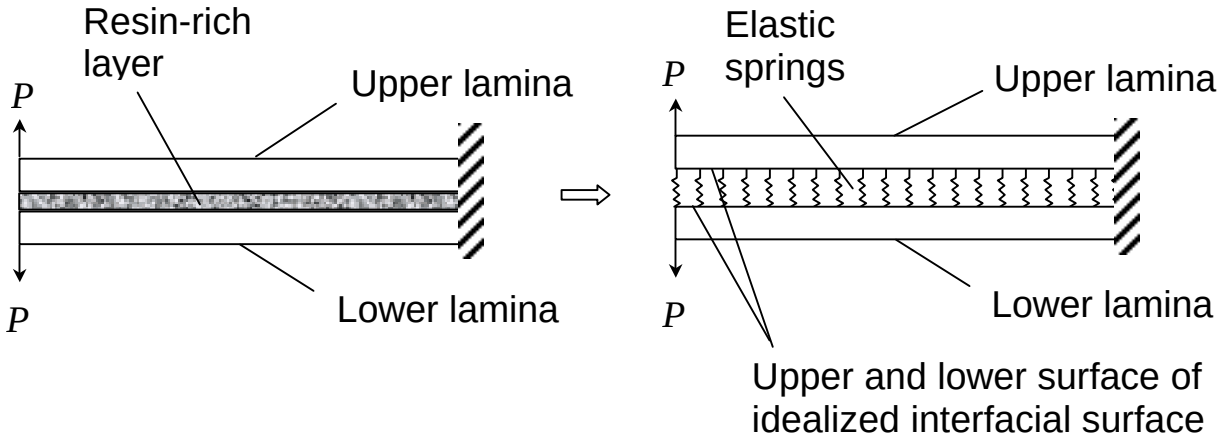


Figure 1.15: Adhesive layer modeled as discrete continuous springs

material consisting of an upper and lower surface connected by a continuous distribution of normal and tangential disconnected springs.

The adhesive layer bounded by the upper adherend and the lower adherend modeled as a discrete continuous distribution of springs in the interfacial model is shown in Fig. 1.15. The assumption here is that if the thickness of the adhesive layer is very small (which is generally the case) the stress distribution through the thickness of the layer is negligible. Mathematically, this can be stated as: as the limit of the thickness tends to zero, the tractions at the upper and lower interfaces must be equal. This leads to the simplification that the tractions acting in the spring are uniform across the thickness. A gap between the two structures is drawn to show the springs, but there is no gap between them in the unloaded configuration. Also the tangential springs are not shown so as to enhance the clarity of the figure. One side of the DCB specimen is clamped and the other end is subjected to the specified equal and opposite lateral forces that open the crack.

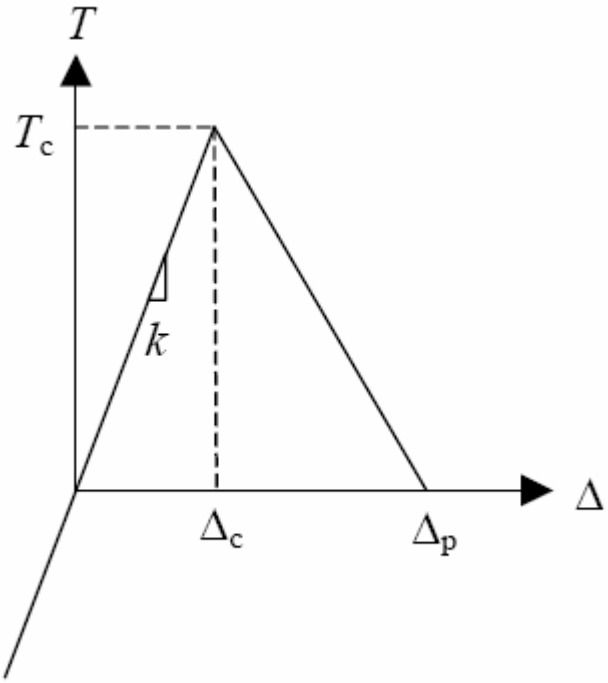


Figure 1.16: Bilinear traction displacement constitutive law for the spring

Symmetry of the DCB allows one to neglect the tangential tractions and also makes the analysis similar to the beam on elastic foundation attributed to Winkler. The traction $T$ offered by the spring can be related to the displacement jump $\Delta$ in more than one way. The simplest way is the bilinear form as shown in Fig. 1.16. The bilinear traction displacement law, also called the cohesive decohesive law, is a modification of the early work of Dugdale (1960) and that of Barenblatt (1962). Both of them independently proposed a nonlinear crack tip zone model for perfectly brittle fracture to determine the extent of the plastic zone ahead of the crack tip. The stress singularity was eliminated by choosing the appropriate size of the plastic zone from linear elastic fracture mechanics.

The plastic zone size $\rho$ was calculated by superposition of a through crack under remote tension stress $K_I$ and crack stresses applied at the crack tip $\sigma_y$. The plastic zone size was obtained as

$$\rho = \frac{\pi}{8}\left(\frac{K_I}{\sigma_y}\right)^2 \tag{1.3}$$

The softening law or the cohesive-decohesive zone law, with reference to an arbitrary interfacial crack with the zones in front of the crack tip, is shown in Fig. 1.17. The figure also shows two distinctive zones in the cohesive zone. The first region enclosed by $B$ and $C$ have large but finite tractions due to resistance to crack propagation. The point $C$ is assumed to have low magnitude tractions. Material degradation occurs in the region marked by $A$ and $B$. The presence of the crack tip is a matter of interpretation; both points $A$ and $B$ could be used to define the crack tip. We shall define the crack tip at $A$ where the tractions are numerically negligible. The material parameters needed to form a constitutive behavior are the maximum interfacial strength and the fracture toughness of the material. A crack is initiated when the interfacial traction attains the maximum strength, and the crack is advanced when the work of fracture equals the material's resistance to crack propagation.

### 1.4.1 Constitutive Laws

The maximum interfacial strength and the critical fracture energy are the two important criteria which a constitutive law needs to represent. Mathematical form (*i.e.* the shape

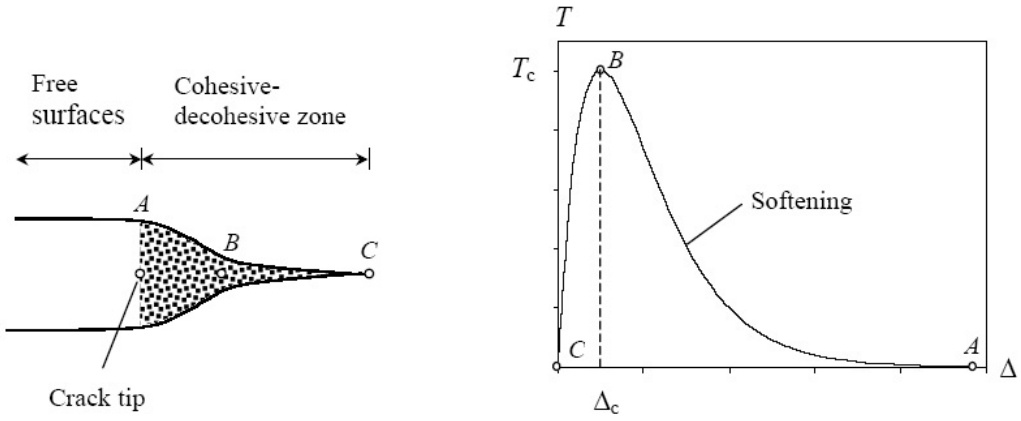


Figure 1.17: Bilinear traction displacement constitutive law for the spring

of the law) is not uniquely defined as has been shown by Knauss (1974) and Rice (1978). The only reason we have chosen to use the exponential traction displacement jump relations is due to the fact that its derivative is continuous and there are resulting numerical advantages associated in calculating tangential stiffness. In addition to this numerical advantage, it also represents the physical behavior involved in atomic separation better, as reported by Rose *et al.* (1981)

Needleman (1987) studied the debonding of composite structures using a polynomial softening constitutive law. He concluded that the cohesive-decohesive models are well suited when the interface strength is relatively low compared to the surrounding material as is the case in a bimaterial system. Xu and Needleman (1993) proposed an exponential constitutive law and implemented it subsequently ( Xu and Needleman (1994), Xu and Needleman (1995), Xu and Needleman (1996)) to study the dynamic crack growth in bimaterial systems. The law was developed for plane strain and plane stress con-

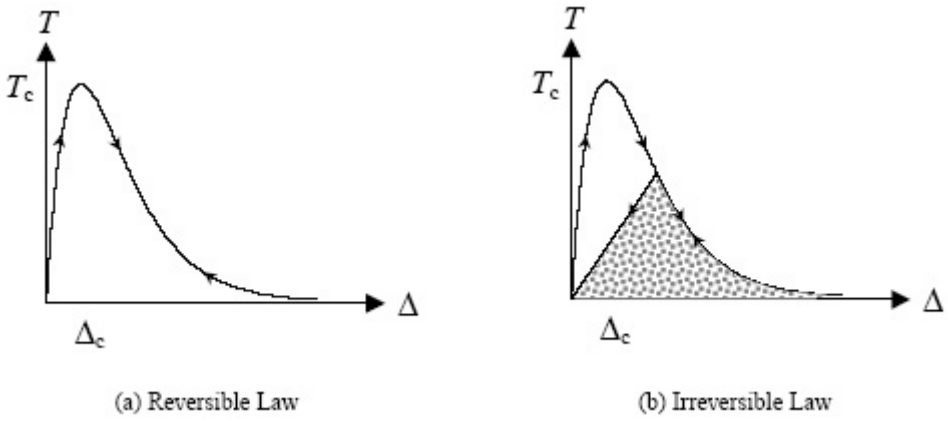


Figure 1.18: Comparison between Reversible and Irreversible laws

ditions, with mixed mode coupling between normal and shear tractions. Rahul-Kumar *et al.* (1999) extended Xu-Needleman's law to predict normal and interfacial fracture in three-dimensional structures. They studied the polymer interfacial fracture mechanics and later ( Rahul-Kumar *et al.* (2000a)) augmented the model to include resistance to interpenetration of surfaces. Furthermore, a dynamic case was studied for glass/polymer composites (Rahul-Kumar *et al.* (2000b)) on a compressive shear strength test.

The softening law is based on the fact that after the maximum interfacial strength is attained, the material starts to degrade. This assumption leads to an irreversible law which was developed by Ortiz and Pandolfi (1999). A comparison between the irreversible and the reversible law is shown in Fig. 1.18. The major drawbacks of the method suggested by Ortiz and Pandolfi (1999) is that the strain energy release rates and the maximum interfacial strength for different modes cannot be specified separately, whereas the law proposed by Xu-Needleman does not have this restriction. Both these laws however do not satisfy the empirical fracture criteria for the initiation and propagation of cracks.

Recent work by Goyal *et al.* (2002) has included these empirical criteria in the formulation. This formulation will be described subsequently in Chapter 2.

### 1.4.2 Fracture Tests for CZM Modeling

A few parameters in the CZM need to be determined experimentally for the specific adhesive. The ultimate tensile strength is one of these parameters, which is experimentally obtained using the "Dog-Bone" test on bulk polymer. The critical energy release rates for various modes are obtained using different test configurations; $G_{I_c}$ is determined using the DCB test configuration, for Mode II the ELS configuration is used, and also some shear test are being planned at Oak Ridge National Laboratory (ORNL). Physical bonds degrade under the combined effect of the fracture modes and therefore it is necessary to study the characteristics of the material under mixed mode loading.

## 1.5 Computational Difficulties

Several computational issues arise when softening constitutive laws are used. The interpenetration of the surfaces is the biggest numerical difficulty reported by Needleman (1990a) and Needleman (1990b). The laws generate a resistive compressive normal force to avoid interpenetration. However, there is no limit on this resistive force, and the compressive stiffness increases with interfacial penetration, which often leads to numerical

problems related to ill-conditioning.

Interface elements are known to be susceptible to mesh sensitivity. Mi *et al.* (1998) demonstrated that if a coarse mesh is used ahead of the crack tip, the softening portion of the constitutive law causes an oscillatory load-deflection structural response. Since a coarse mesh cannot represent properly the large stress gradients ahead of the crack tip, the numerical solutions are highly oscillatory. To obtain a relatively smooth solution, they recommended that the mesh should be fine enough to contain at least two decohesion elements in the cohesive-decohesive zone ahead of the crack tip.

Researchers using bilinear constitutive laws have reported numerical difficulties in nonlinear solution methods. These numerical difficulties are not so severe in the case of an exponential constitutive law. In some structural problems, when the bilinear softening constitutive law is used, a converged solution cannot be obtained because the residual force in the Newton-Raphson procedure oscillates cyclicly. A recent compilation of the numerical difficulties has been done by de Borst (2003). The mesh dependency of the cohesive zone models implemented through the interface element, along with the ill-posedness of the rate boundary value problem that arises with the smeared formulation (crack tends to propagate along the interelement boundaries), has been addressed. In addition there is a numerical difficulty associated with the rate dependency being modeled in the unstable region of the schematic shown in Fig. 1.12.

Chen *et al.* (1999) used two different techniques to obtain converged solutions: displacement control in conjunction with line search algorithm and the modified cylindrical

arc-length method. However, with linear and quadratic decohesion elements, convergence difficulties were still encountered. As suggested by Mi *et al.* (1998), the convergence difficulties were overcome by reducing the interlaminar strength while maintaining the same critical fracture energy. de Borst and Rots (1989) suggested an alternative method for convergence of the nonlinear problem. The residual force slowly converges to zero with this modification, but in general, a converged solution is guaranteed. Goyal-Singhal and Johnson (2001) and Goyal *et al.* (2002) employed a Newton-Raphson method and modification of the Xu-Needleman for the interpenetration.

### 1.5.1 Extended Finite Element Method

To overcome some of the problems discussed in the previous section, another method to formulate the crack propagation problem using a partition-of-unity method is attempted. The modeling of a propagating crack has been restricted to the interelement boundaries or the time adaptive finite element meshing, both of which are computationally expensive. The direction of the crack propagation in the interface element is limited locally, *i.e.*, it is confined to the interface element. Figure 1.19 shows the modeling of bulk elements surrounded by interface finite elements. For this configuration, if the crack tip is located near a node, then it has five possible paths on which it can grow and which are shown in Fig. 1.19. Recently a new approach has been adopted to circumvent the mesh dependency of the interface method and the numerical difficulties associated with it. The method is based on the partition-of-unity approach of finite elements developed

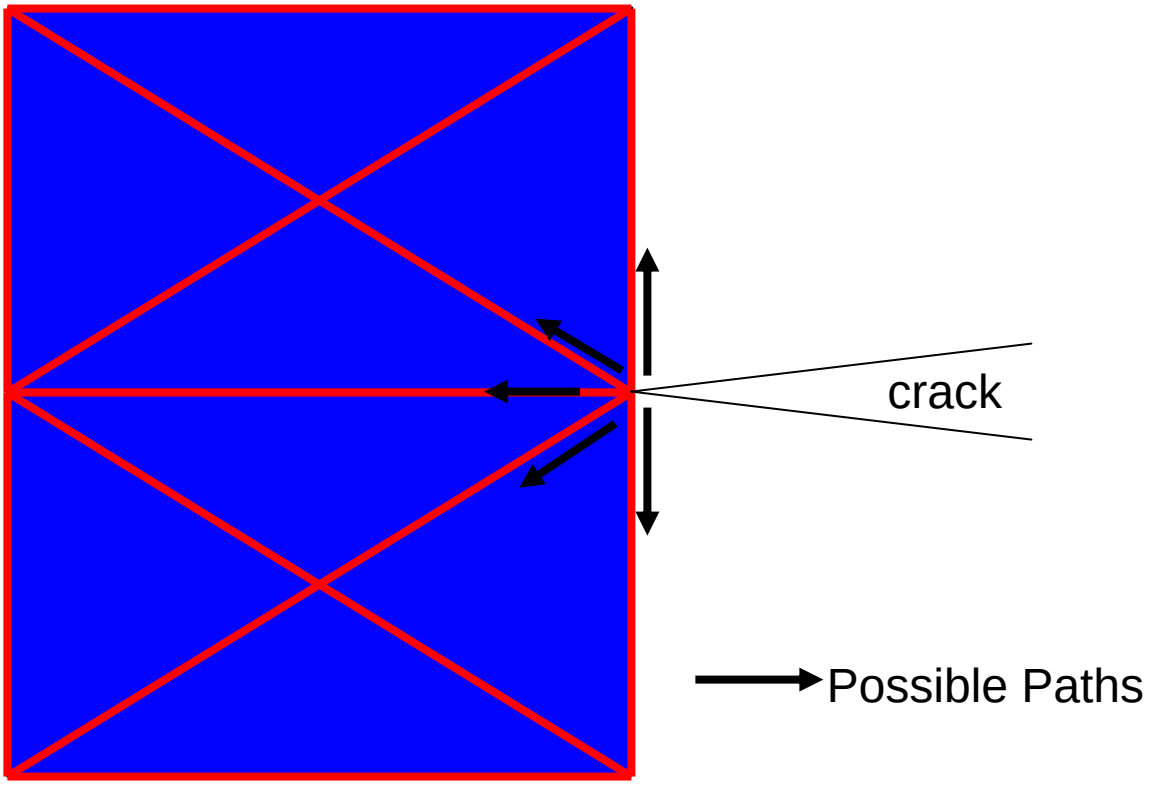


Figure 1.19: Possible crack paths at a given node with bulk and interface modeling

first by Melenk and Babuska (1996). This method, known as the extended finite element approach or the enhanced finite element approach, has been developed simultaneously by two groups. One group consists of researchers at the Delft University leaded by Prof. G. N. Wells and the other is the group led by Prof. Ivo Babuska at The University of Texas at Austin. The advantage of this method is that it allows the crack to pass through the element, thereby reducing mesh dependency. Moës *et al.* (1999) presented the technique as an alternative to remeshing for crack propagation. Propagation of a crack in this approach was determined based on linear elastic fracture mechanics. The

basic idea in this approach is adding additional degrees of freedom or what is known as enriching the nodes once a crack has gone through the element. The domain $\Omega$ with a crack $\Gamma_d$ shown in Fig. 1.20 is divided into two domains using the Heaviside function. The complete derivation of this method will be described in Chapter 6.

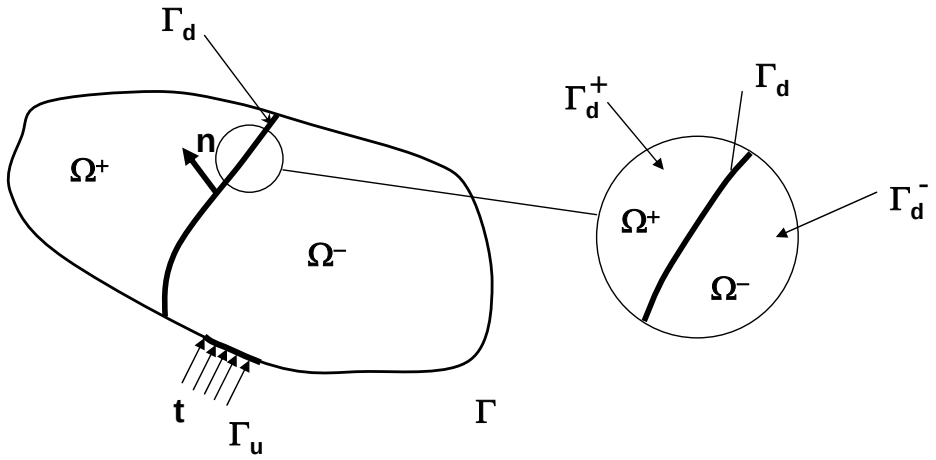


Figure 1.20: Body $\Omega$ crossed by a discontinuity $\Gamma_d$

Moës and Belytschko (2002) later extended their preliminary work to study the cohesive crack growth in concrete. They studied the effects of a linear and rectangular traction-displacement law across the crack surface. A similar approach to study the cohesive crack growth based on the partition-of-unity method was developed by Wells and Sluys (2001a). An exponential cohesive law was employed to study the crack growth in homogeneous material in a simple test like the three-point bend test. In a series of papers, the group studied this method in softening solids (Wells and Sluys (2001b)), and in strain-softening materials with both Mode I and Mode II being studied (Wells *et al.* (2002)). Mathematical studies have been carried out to study the mesh dependency and interpo-

lation requirements ( Alfaiate *et al.* (2002), Simone *et al.* (2003), Simone *et al.* (2003)). A study by Alfaiate *et al.* (2003) is devoted to a comparison of the results of this method with the traditional fracture mechanics approach and the interface element approach. One basic difference between the two approaches discussed here is the method by which the crack is propagated. The method suggested by Wells and group (at Delft University) assumes that when the failure criterion is met, the crack will propagate through the complete element, whereas the approach suggested by Moës and Belytschko allows the crack to arrest within the element itself. This basic difference makes the approach of Moës and Belytschko theoretically more mesh independent. However, a numerical study done by Wells and Sluys (2001a) has shown the numerical difficulties in establishing equilibrium at each load increment when the crack is arrested within the element.

## 1.6 Objectives of the Dissertation

The overall aim of this thesis can be classified into the following main objectives:

**Develop a rate dependent CZM law from fracture testing of the SIA adhesive to model its unstable crack growth behavior**

The polymer based adhesive, SIA, used in this study exhibits stick-slip behavior and as shown here, the rate independent interface elements are incapable of predicting such behavior. With the help of the experiments performed on compact tension tests at ORNL,

a rate dependent dynamic interface element is developed.

**Implement the rate dependent law in LS-DYNA and simulate the impact response and dynamic fracture of adhesively bonded composite tubes**

LS-DYNA does not allow the user to incorporate new elements in it, but it does allow the incorporation of a user defined material. The CZM law is therefore simulated using a user defined material. This formulation is further extended to incorporate the rate dependent behavior of SIA. The complete formulation will allow us to model the adhesively bonded composite tube, the main objective of the study.

**Intitial preliminary investigations to develop a separate numerical simulation of progressive fracture using the extended finite element method**

The mesh dependency and the modeling difficulties in the case of the bulk modeling has made the extended finite element method an attractive alternative. However, until now, the method has only been tested for crack propagation in homogeneous materials under quasi-static conditions. Formulation and extension of the method to simulate crack propagation in bimaterial systems and functionally graded materials *under dynamic conditions* is one of the other objectives.

## 1.7 Outline of the Dissertation

The first topic discussed is the cohesive zone model and the implementation through an interface element approach. Chapter 2 gives a brief description of the cohesive zone model that is being used and the dynamic formulation of the interface element based on this CZM. Static and dynamic problems have been simulated and compared to results from experiments conducted at the Adhesion Science Lab in ESM and other results given in the literature. The limitations of the rate independent interface elements while simulating the aluminum DCB bonded with the SIA adhesive are discussed and a detailed model used to capture the unstable crack growth is presented.

A rate dependent model is formulated based on the compact tension test experimental data, and the step by step procedure is explained in Chapter 3. The two rate dependent models that are developed are discussed in detail along with their implementation in the interface element approach. Numerical results for the aluminum DCB bonded with the SIA adhesive are presented and compared to experimental results.

Chapter 4 gives the details of the CZM implementation in an explicit code (LS-DYNA) through the user defined material model (UMAT) option. The implementation is discussed in detail because it is not available in the open literature. The UMAT formulated is verified against experimental results of the aluminum and composite DCB. The consequences of the assumption of constant velocity imparted from the falling wedge to the adherends in a drop tower test are examined closely and numerical results for composite

DCBs are discussed. Preliminary Mode II simulations are also presented.

Square composite tubes are studied under axial compression in Chapter 5. Both the bonded and the unbonded tubes are studied. The unique failure mode observed in the experiments has been captured in the numerical simulations. Cohesive zone models implemented through the user defined material models have been used to simulate the bond in the composite tube.

An alternative technique to model crack growth known as the Extended Finite Element based on the partition-of-unity approach is formulated and implemented in Chapter 6. The formulation has been augmented to include the inertia effects under dynamic loading and the formulation has been verified with various experimental results for isotropic, functionally graded, and bimaterial systems.

The last chapter gives a summary of all the methods developed and implemented to study crack growth in composite materials and some suggestions for future work are made.

# Chapter 2

# Rate Independent CZM Modeling

## 2.1 Introduction

Interfaces are ubiquitous in engineering, and often play a dominant role in mechanical performance. During the past decade, the field of interfacial damage mechanics has emerged as an innovative technique combining the fields of Linear Elastic Fracture Mechanics (LEFM) and continuum mechanics. To study the crack growth within the interface, the ideas of Dugdale (1960) and Barenblatt (1962) are applied extensively and the resulting model called the Cohesive Zone Model (CZM) has been employed. In this model, a softening traction-displacement jump relationship with finite strength is used to characterize the interaction of the cohesive surfaces. When incorporating it in a crack formulation, the problem is well posed, and the singularity appearing in conventional

fracture mechanics can be eliminated completely. The CZM is implemented in the finite element approach by interface elements which model the interface with a pair of surfaces with no volume between them in the undeformed configuration. The exact mathematical form of the cohesive zone model is less significant than the capability of the model to represent the maximum interfacial strength and critical fracture energy. This leads to an important feature that the dependence of the traction field on the displacement jump across the interface is not unique; this has been concluded from the detailed studies performed by Knauss (1973) and Rice (1978). The exponential law has certain computational advantages since the function is smooth and is continuously differentiable. The computational advantages of the exponential law were studied in detail by Goyal *et al.* (2002).

One of the pioneers in implementing the CZM in finite element analysis has been Needleman. He proposed the exponential constitutive law,( Xu and Needleman (1993)) and later used it to study the dynamic crack growth along interfaces in a bimaterial system ( Xu and Needleman (1995) and Xu and Needleman (1996)). The exponential law was further augmented by many researchers, mainly to prevent interpenetration ( Rahul-Kumar *et al.* (2000b)) and to account for damage due to fatigue by introducing an irreversible law ( Goyal *et al.* (2002)).

## 2.2 Static Fracture Analysis

Discretization of the idealized interfacial surface material to implement in finite element analysis is referred to as interface elements. Based on the constitutive law used, they have also been referred to as joint elements and decohesion elements for the bilinear and exponential law, respectively. Interface elements have been used to study crack growth in isotropic materials as well as rocks and concrete.

Beer (1985) developed a general isoparametric element applicable to three-dimensional solid elements and two-dimensional shell elements. In this formulation, the geometric interfacial nonlinearities were not considered. Approximations based on the von-Karman plate theory were taken into consideration by Ortiz and Pandolfi (1999) and Allix and Corigliano (1999). A consistent tangent stiffness matrix including all the geometric terms was formulated by Goyal (2002). This is the formulation followed in this dissertation.

Discussing the complete detailed formulation of the interface element and its implementation in ABAQUS for quasi-static analysis is not the primary objective of this dissertation. The details are well documented in the open literature. The details of this formulation have been meticulously given in Goyal (2002). However, for the sake of completeness of this dissertation, the basic principles and theory will be discussed very briefly.

### 2.2.1 Formulation

The discussion of the cohesive zone model for a single mode, along with the effects of various parameters, will be done in detail for understanding, and the mixed mode laws and initiation and progression of a crack under mixed mode conditions will be given. A brief outline of the finite element formulation along with the solution procedure will conclude this section.

#### 2.2.1.1 Exponential Law for CZM

This section focuses on the exponential law for a single mode based on the cohesive zone model. Figure 2.1 shows the basic concept of the interface element. The surface $S^0$ in the undeformed configuration consists of two surfaces $S^+$ and $S^-$ overlaying on each other to form the single surface. The two surfaces $S^+$ and $S^-$ separate from each other on loading and can be seen in the deformed configuration. The tractions are evaluated on the mid-surface depicted as $\bar{S}$ in Fig. 2.2. Consider an arbitrary point $\bar{P}$ on the mid-surface with nonlinear springs connecting the points $P^+$ and $P^-$ on the interfacial surfaces. The stretching of the springs under applied loading is resisted by the traction force $T$ given by

$$T(\Delta) = T_c \; \bar{\Delta} \; Exp\left(\frac{1-\bar{\Delta}^{\beta}}{\beta}\right) \tag{2.1}$$

where $\bar{\Delta} = \Delta/\Delta_c$, and $T_c$ is the maximum force of that spring that occurs at the

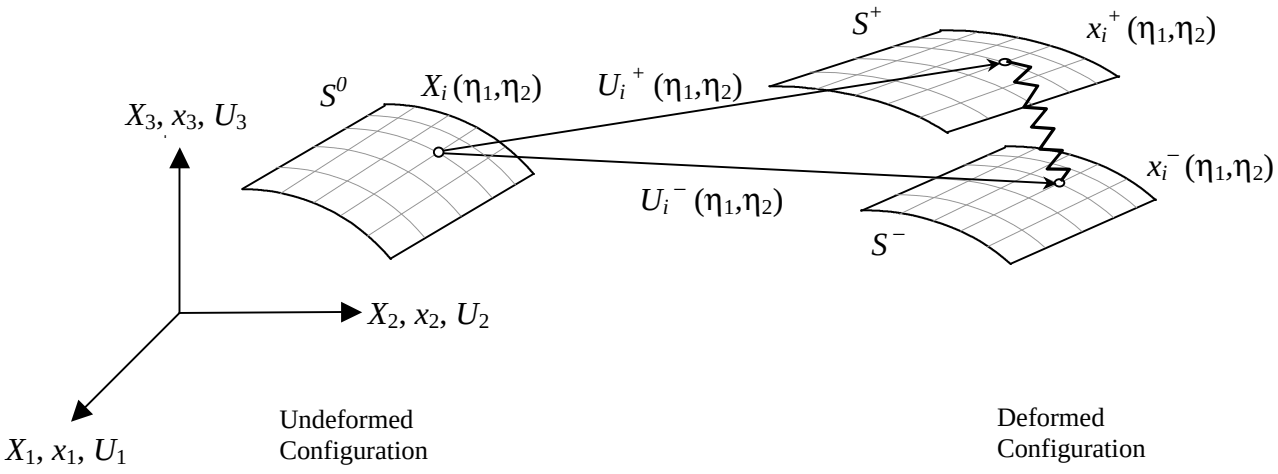


Figure 2.1: Interface surface deformation

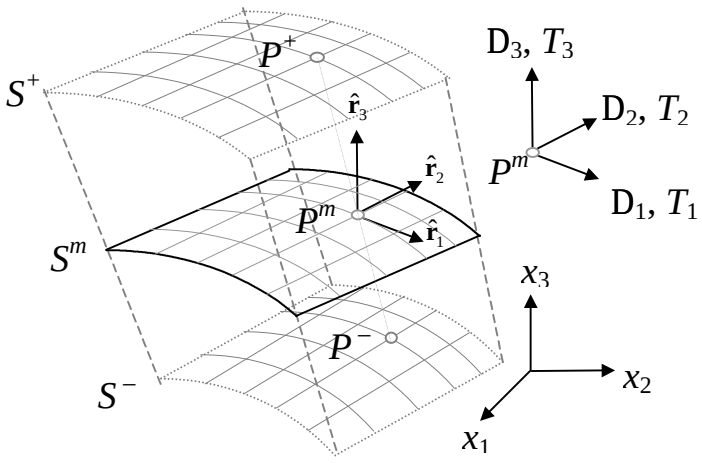


Figure 2.2: Traction components acting at the interface midsurface.

critical separation value of $\Delta_c$. The parameter $\beta$ controls the numerical value of $\Delta_c$ and the softening portion of the exponential law. $\beta$ is quite often referred as the brittleness parameter since it controls the time to complete degradation once the element has started to soften. The effect of $\beta$ will be discussed in detail in this chapter. A high value of $\beta$ idealizes brittle fracture, and a low value of $\beta$ idealizes ductile fracture. From Eq. 2.1, the work of fracture $G_c$ is obtained as the area under the exponential traction-separation law, which is given by

$$G_c \;=\; \int_0^{\infty} T\left(\Delta\right)\; d\Delta \;=\; T_c\;\Delta_c\;\psi\left(\beta\right) \tag{2.2}$$

where the $\psi\left(\beta\right)$ factor is defined as

$$\psi\left(\beta\right) \;=\; \beta^{(2-\beta)\;/\beta}\,\Gamma\left[\frac{2}{\beta}\right]\;Exp\left(\frac{1}{\beta}\right) \tag{2.3}$$

and $\Gamma[z]$ is the Euler gamma function of argument $z$ and is given by

$$\Gamma[z] \;=\; \int_0^{\infty} t^{z-1} Exp\;(-t)\;dt \tag{2.4}$$

The parameters to be specified in the exponential constitutive law are the maximum spring force $T_c$, the critical energy release rate $G_c$, and the brittleness parameter $\beta$. Equation 2.4 is only valid for monotonically increasing opening displacement because the work due to opening is recoverable on unloading. To account for the irreversible process,

an internal state variable $d$ that tracks the damage state of the spring is included:

$$T\ (\Delta) = T_c\ \bar{\Delta} Exp\left(\frac{2 - \left(\left[\bar{\Delta}^{\beta}\right]\ /\ d\right) - d}{\beta}\right) \tag{2.5}$$

$d$ must increase as a function of time and it must be sem-positive. An equivalent mathematical expression at discrete time $t\ +\ \delta t$ is

$$^{t+\delta t}d = max\left(1,\ ^{t}d,\ ^{t+\delta t}\bar{\Delta}^{\beta}\right) \quad \text{with initial value} \quad ^{0}d = 1 \tag{2.6}$$

At the undamaged state at $t = 0$, the initial condition for the damage variable is $^{0}d = 1$. Unloading will occur with an exponential form.

The formulation thus far lacks the capability of resisting interpenetration, *i.e.* the upper and lower surfaces of the interface element coming into contact. A resistive compressive normal traction $T_3$ prevents interpenetration of these two surfaces. Here the assumption is that the compressive force does not contribute to the interfacial damage. The constitutive law for Mode I crack growth is slightly modified to take into consideration the mechanical behavior of the interfacial surface when the two surfaces comes into contact with each other. We include an interpenetration law in Eq. 2.5 as follows:

$$T = T^c\left\langle\bar{\Delta}\right\rangle Exp\left(\frac{2 - \left(\left[\left\langle\bar{\Delta}\right\rangle^{\beta}\right]\ /\ d\right) - d}{\beta}\right) + T^c\left\langle-\bar{\Delta}\right\rangle Exp\left(\frac{1 + \kappa|\bar{\Delta}|^{\beta}}{\beta}\right) \tag{2.7}$$

The operator $\langle l \rangle$ is defined as

$$\langle l \rangle = \begin{cases} |l| & \text{if} \quad l > 0 \\ 0 & \text{if} \quad l \leqslant 0 \end{cases} \tag{2.8}$$

The operator $|l|$ is the absolute value of $l$, and $\kappa$ is an interpenetration factor with $\kappa \geqslant 1$ to magnify the repulsive force $T_3$.

The conditions for pure Mode II loading are $\Delta_1 \neq 0$, $\Delta_2 = 0$, and $\Delta_3 \leqslant 0$. The tangential traction $T_1$ resists the sliding displacement jump $\Delta_1$. Under pure Mode II there are two sliding possibilities: (i) the top surface slides in the positive direction relative to the lower surface, and (ii) the top surface slides in the negative direction relative to the lower surface. The constitutive laws are slightly modified to take into account the tangential traction sign reversal as follows:

$$T_1 = T_1^c \bar{\Delta}_1 \, Exp\left( \frac{2 - \left[ |\bar{\Delta}_1|^\beta \right] / d - d}{\beta} \right) \tag{2.9}$$

Similarly, the conditions for pure Mode III are $\Delta_2 \neq 0$, $\Delta_1 = 0$, and $\Delta_3 \leqslant 0$. The modified constitutive law for Mode III loading is obtained by the same arguments discussed for the Mode II loading.

To satisfy the multi-axial stress criterion for the nucleation of cracks given by

$$\bar{T} = \left( \left( \frac{T_1}{T_1^c} \right)^\theta + \left( \frac{T_2}{T_2^c} \right)^\theta + \left( \frac{\langle T_3 \rangle}{T_3^c} \right)^\theta \right)^{\frac{1}{\theta}} \tag{2.10}$$

with $\theta = \alpha$, and the mixed mode fracture criterion given by

$$\left(\frac{G_I}{G_{I_c}}\right)^{\lambda_3} + \left(\frac{G_{II}}{G_{II_c}}\right)^{\lambda_1} + \left(\frac{G_{III}}{G_{III_c}}\right)^{\lambda_2} = 1 \tag{2.11}$$

with $\lambda_1 = \lambda_2 = \lambda_3 = \alpha/2$, we postulate the following functions:

$$\Theta_1 = \Theta_2 = \Theta_3 = Exp\left(\frac{2 - \left(\mu^\beta/d\right) - d}{\beta}\right) = \Theta \tag{2.12}$$

The mixed mode parameter $\mu$ is defined such that it couples the normalized displacement jumps for the opening and the sliding modes; mathematically $\mu$ can be written as

$$\mu = \left(\left|\bar{\Delta}_1\right|^\alpha + \left|\bar{\Delta}_2\right|^\alpha + \left\langle\bar{\Delta}_3\right\rangle^\alpha\right)^{1/\alpha} \tag{2.13}$$

The material parameter $\alpha$ defines the shape of the failure surface for the onset and progression of delamination. Including the interpenetration term, we obtain the final form of the mixed mode constitutive laws as follows:

$$\left\{\begin{array}{c}\bar{T}_1\\ \bar{T}_2\\ \bar{T}_3\end{array}\right\} = \left\{\begin{array}{c}\bar{\Delta}_1\\ \bar{\Delta}_2\\ \bar{\Delta}_3\end{array}\right\}\Theta + \left\{\begin{array}{c}0\\ 0\\ -\left\langle-\bar{\Delta}_3\right\rangle\end{array}\right\} Exp\left(\frac{1+\kappa\left|\bar{\Delta}_3\right|^\beta}{\beta}\right) \tag{2.14}$$

Equation 2.14 is also referred to as the *Power Constitutive Law.*

#### 2.2.1.2 Principle of Virtual Work

Consider an interface element sandwiched between two external bodies. Let the body force per unit volume be denoted by $b_i$ and the surface tractions per unit external surface area be denoted by $\tilde{T}_i$, which are prescribed as acting on a body of material $\Omega$ in its deformed state. The external virtual work $\delta W_{ext}$ of the body forces and the surface tractions is

$$\delta W_{ext} = \int\int_{\partial\Omega} \tilde{T}_i \delta u_i dS + \int\int\int_{\Omega} b_i \delta u_i d\Omega \tag{2.15}$$

where $\partial\Omega$ is the entire surface area of the body. The prescribed surface tractions are acting on $\partial\Omega_\sigma$, and over the remaining part of the boundary, $\partial\Omega_u$, we prescribe the displacement field $u_i$. Since $\delta u_i = 0$ on $\partial\Omega_u$, we have extended the surface integral in the external virtual work expression to cover the entire surface $\partial\Omega = \partial\Omega_\sigma + \partial\Omega_u$. The boundary conditions are:

$$\sigma_{ij} n_j = \tilde{T}_i \quad \text{on} \quad \partial\Omega_\sigma \quad \text{and} \quad u_i = \tilde{u}_i \quad \text{on} \quad \partial\Omega_u \tag{2.16}$$

where $n_j$ is the unit outward normal component to the external surface, $\sigma_{ij}$ are the Cauchy stress components, and the tilde denotes a prescribed quantity. The internal virtual work in the deformed state due to the stress field $\sigma_{ij}$ is

$$\delta W_{int} = \int\int\int_{\Omega} \sigma_{ij} \delta\epsilon_{ij} d\Omega \tag{2.17}$$

where $\epsilon_{ij}$ are the infinitesimal strain tensor components. For every statically admissible stress field, the internal virtual work is equal to the external virtual work done by the external forces on any kinematically admissible field, that is

$$\delta W_{int} = \delta W_{ext} \tag{2.18}$$

If the displacement is discontinuous across an interior surface of the body, the principle of virtual work cannot be applied to the whole body, but can be written for each subregion in which the derivatives are continuous Malvern (1969). Figure 2.3 shows a material $\Omega$ separated into two subdomains $\Omega^+$ and $\Omega^-$ by a strong discontinuous surface $S$. The surface $S$ is defined by the outward normal $\hat{r}$. There are two surfaces that bound the

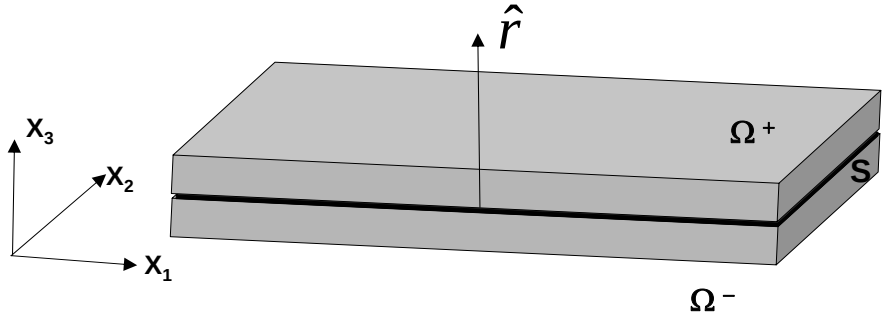


Figure 2.3: Interfacial surface traversing a body of material.

surface $S$, the lower surface of $\Omega^+$ denoted by $S^+$ and the upper surface of $\Omega^-$ denoted by $S^-$. Each of the surfaces $S^\pm$ is defined by its respective unit outward normal $\hat{r}^\pm$. The interfacial surface is an internal surface that consists of the upper and lower surfaces $S^\pm$. $S^0$ denotes the mid-surface $S$ in the undeformed configuration. The surfaces $S$,

$S^+$, and $S^-$ are assumed to coincide with the reference surface $S^0$ in the undeformed configuration, which allows us to state the assumption that in the unloaded state, the interfacial surface has zero thickness. In the context of a formed crack, $S^+$ and $S^-$ are the crack faces. The principle of virtual work for each continuous subdomain $\Omega^{\pm}$ is

$$\begin{aligned}
\iiint_{\Omega^+} b_i \delta u_i d\Omega + \iint_{\partial\Omega^+} \tilde{T}_i \delta u_i dS + \iint_{S^+} T_i^+ \delta u_i^+ dS^+ &= \iiint_{\Omega^+} \sigma_{ij} \delta\epsilon_{ij} d\Omega \\
\iiint_{\Omega^-} b_i \delta u_i d\Omega + \iint_{\partial\Omega^-} \tilde{T}_i \delta u_i dS + \iint_{S^-} T_i^- \delta u_i^- dS^- &= \iiint_{\Omega^-} \sigma_{ij} \delta\epsilon_{ij} d\Omega
\end{aligned} \tag{2.19}$$

The resultants due to the traction components acting on any interior surface must be continuous by Newton's Third Law. However, the stress components are not necessarily continuous. Hence the balance equation at the interfacial surface boundaries is

$$T_i^+ dS^+ + T_i^- dS^- = 0 \ \forall \ x_i^{\pm} \in S^{\pm} \tag{2.20}$$

Adding the equations in Eq. 2.19 and replacing $T_i^- dS^-$ with $-T_i^+ dS^+$, we obtain

$$\iiint_{\Omega} b_i \delta u_i d\Omega + \iint_{\partial\Omega} \tilde{T}_i \delta u_i dS = \iiint_{\Omega} \sigma_{ij} \delta\epsilon_{ij} d\Omega - \iint_{S^+} T_i^+ \left( \delta u_i^+ - \delta u_i^- \right) dS^+ \tag{2.21}$$

We assume that the traversing surface $S$ coincides with the interfacial midsurface $\bar{S}$ throughout the history of deformations. Therefore, the normal and the tangential components of the traction and displacement jump vectors are determined by the local unit

outward normal $\hat{r}$. Therefore, the boundary conditions acting at the interfacial midsurface can be written as:

$$T_i^+ dS^+ = -T_i^- dS^- = -\hat{T}_i d\bar{S} \ \forall \ x_i^\pm \in S^\pm \text{ and } \bar{x} \in \bar{S} \tag{2.22}$$

The principle of virtual work equation for the discontinuous system is

$$\iiint_\Omega b_i \delta u_i d\Omega + \iint_{\partial\Omega} \tilde{T}_i \delta u_i dS = \iiint_\Omega \sigma_{ij} \delta \epsilon_{ij} d\Omega + \iint_{\bar{S}} \hat{T}_i \delta [\![u_i]\!] d\bar{S} \tag{2.23}$$

where $\hat{T}_i$ are the interfacial traction components acting on a unit deformed interfacial midsurface area conjugate to the displacement jump $[\![u_i]\!]$, and $\bar{S}$ is the midsurface area. Define a local midsurface coordinate system such that the basis vectors are normal and tangential to the midsurface. Since the mechanical laws to be postulated relate the normal and the tangential traction components acting at the interfacial midsurface to the normal and tangential displacement jumps, we rewrite the principle of virtual work as:

$$\iiint_\Omega b_i \delta u_i d\Omega + \iint_{\partial\Omega} \tilde{T}_i \delta u_i dS = \iiint_\Omega \sigma_{ij} \delta \epsilon_{ij} d\Omega + \iint_{\bar{S}} R_{ij} T_j \delta [\![u_i]\!] d\bar{S} \tag{2.24}$$

$R_{ij}$ is the rotation tensor relating the midsurface local coordinate system to the fixed coordinate system. $T_1$ and $T_2$ are the tangential traction components to the interfacial midsurface and $T_3$ is the normal traction component.

We replace the expression of the internal virtual work with the integral over the reference

volume for standard displacement based finite element analysis as follows:

$$\iiint_{\Omega} b_i \delta u_i d\Omega + \iint_{\partial\Omega} \tilde{T}_i \delta u_i dS = \iiint_{\Omega_0} S_{ij} \delta E_{ij} d\Omega_0 + \iint_{\bar{S}} T_j R_{ij} \delta [\![u_i]\!] d\bar{S} \tag{2.25}$$

$S_{ij}$ are the PK2 stress tensor components and $E_{ij}$ are the Green Lagrange strain tensor components. The displacement field $u_i$ is interpolated with the shape functions as:

$$u_i = N_{ik}\ q_k \tag{2.26}$$

where $N_{ik}$ is the interpolation function matrix and $q_k$'s are the nodal displacements. The continuum variational statement is approximated by a variation over a finite set $\delta q_k$:

$$\delta q_k \left\{ \iiint_{\Omega} b_i N_{ik} d\Omega + \iint_{\partial\Omega} \tilde{T}_i N_{ik} dS - \iiint_{\Omega_0} S_{ij} \frac{\partial E_{ij}}{\partial q_k} d\Omega_0 - \iint_{\bar{S}} T_j R_{ij} \frac{\partial [\![u_i]\!]}{\partial q_k} d\bar{S} \right\} = 0 \tag{2.27}$$

Since $\delta q_k$ are independent variables, we can choose each one to be nonzero and all others to be zero. Thus, for each $\delta q_k$ there is an associated equation $f_k = 0$ with $k = 1, 2, ..., n$ given as

$$f_k = \iiint_{\Omega} b_i N_{ik} d\Omega + \iint_{\partial\Omega} \tilde{T}_i N_{ik} dS - \iiint_{\Omega_0} S_{ij} \frac{\partial E_{ij}}{\partial q_k} d\Omega_0 - \iint_{\bar{S}} T_j R_{ij} \frac{\partial [\![u_i]\!]}{\partial q_k} d\bar{S} = 0 \tag{2.28}$$

This system of equations forms the basis for the assumed displacement finite element procedure which consists of $n$ equations and $n$ unknowns. Each equilibrium equation in

Eq. 2.28 obtained by discretizing the virtual work equation is written as follows:

$$f_k\left(q_1, q_2, ..., q_n\right) = 0, \qquad k = 1, 2, ..., n \tag{2.29}$$

In the most general form, the above equation is materially and geometrically nonlinear. The stress-strain and the traction-displacement jump relations are nonlinear, and the strains and the displacement jumps are nonlinear functions of the nodal displacements. The nonlinear solution methods are discussed in detail by Goyal (2002) and the reader is referred to it for the complete formulation.

#### 2.2.1.3 Element Formulation

We proceed to derive the interface element tangent stiffness matrix $\mathbf{K}$ and the interface element internal force vector ${}^{int}\mathbf{f}$ required in the nonlinear solution procedure. The expressions for $\mathbf{K}$ and ${}^{int}\mathbf{f}$ are complex due to geometrical and material nonlinearities. The geometric nonlinearities are due to the stretching and the rotation of the upper and lower surfaces of the interface element, and the material nonlinearity is due to the nonlinear traction-displacement jump constitutive law.

Based on the assumptions made in the development of the interface element, the three-dimensional formulation is described here briefly. The eight-noded interface element has three translation degrees of freedom at each node and the nodal coordinates of the

undeformed element can be represented as a vector $\mathbf{C}$ as

$$\mathbf{C} = \{X_1, Y_1, Z_1, ..., X_8, Y_8, Z_8\}^T \tag{2.30}$$

where $(X_i, Y_i, Z_i)$ is the coordinate of the $i$th node. The nodes of the lower interface element surface are numbered first, and the nodes of the upper interface element surface are numbered next. This allows us to split the vector $\mathbf{C}$ in two parts $\mathbf{C}^-$ and $\mathbf{C}^+$ as follows:

$$\mathbf{C}^- = \{X_1, Y_1, Z_1, ..., X_4, Y_4, Z_4\}^T, \quad \mathbf{C}^+ = \{X_5, Y_5, Z_5, ..., X_8, Y_8, Z_8\}^T \tag{2.31}$$

The material coordinate $(X, Y, Z)$ in the interior of the upper surface or the lower surface is interpolated with the shape function matrix $\mathbf{N}$ as

$$\tilde{\mathbf{C}}^- = \mathbf{N}\mathbf{C}^-, \quad \tilde{\mathbf{C}}^+ = \mathbf{N}\mathbf{C}^+ \tag{2.32}$$

where $\tilde{\mathbf{C}} = \{X(\eta_1, \eta_2), Y(\eta_1, \eta_2), Z(\eta_1, \eta_2)\}^T$. The shape function matrix $\mathbf{N}$ is given as

$$\mathbf{N} = \begin{bmatrix} L_1 & 0 & 0 & L_2 & 0 & 0 & L_3 & 0 & 0 & L_4 & 0 & 0 \\ 0 & L_1 & 0 & 0 & L_2 & 0 & 0 & L_3 & 0 & 0 & L_4 & 0 \\ 0 & 0 & L_1 & 0 & 0 & L_2 & 0 & 0 & L_3 & 0 & 0 & L_4 \end{bmatrix} \tag{2.33}$$

with

$$L_1 = \tfrac{1}{4}(1-\eta_1)(1-\eta_2), \qquad L_2 = \tfrac{1}{4}(1+\eta_1)(1-\eta_2)$$
$$L_3 = \tfrac{1}{4}(1+\eta_1)(1+\eta_2), \qquad L_4 = \tfrac{1}{4}(1-\eta_1)(1+\eta_2) \tag{2.34}$$

The nodal displacements can be split for the lower and upper surfaces of the interface element and can be written in a vector form as

$$\mathbf{q}^- = \{u_1, v_1, w_1, ..., u_4, v_4, w_4\}, \quad \mathbf{q}^+ = \{u_5, v_5, w_5, ..., u_8, v_8, w_8\} \tag{2.35}$$

Material coordinates for the middle surface of the interface element can be written as

$$\begin{aligned} \tilde{c} &= \frac{1}{2}\left(\tilde{C}^+ + \tilde{C}^- + \tilde{q}^+ + \tilde{q}^-\right) \\ &= \frac{1}{2}N\left(C^+ + C^- + q^+ + q^-\right) \end{aligned} \tag{2.36}$$

The tangential vectors to the interfacial midsurface at $(\eta_1, \eta_2)$ are simply obtained by the following equation:

$$r_\alpha = \frac{\partial \tilde{c}}{\partial \eta_\alpha} = \frac{1}{2}\frac{\partial N}{\partial \eta_\alpha}\left(C^+ + C^- + q^+ + q^-\right) \tag{2.37}$$

The normal vector to the interfacial midsurface is obtained as

$$r_3 = r_1 \times r_2 = \frac{\partial \tilde{c}}{\partial \eta_1} \times \frac{\partial \tilde{c}}{\partial \eta_2} \tag{2.38}$$

The tangential vector $r_2$ is redefined such that it is orthogonal to $r_1$ as $r_2 = r_3 \times r_1$. The unit normal vectors defined as $\hat{r_i} = r_i/|r_i|$ form the rotation tensor $\mathbf{R}$ which is used to transform the global coordinate system to the local coordinate system and can be written as $\mathbf{R}$= $\{r_1, r_2, r_3\}^T$. The displacement jumps are given by

$$\Delta = \mathbf{R}^T \left[-\mathbf{N}_{3\times 8}\ \mathbf{N}_{3\times 8}\right] \mathbf{q} \tag{2.39}$$

The displacement jump matrix $\tilde{\mathbf{B}}$ is the derivative of the displacement jump vector with respect to the nodal displacement vector. We neglect the derivative of the rotation tensor with respect to the nodal displacement vector. Therefore, $\tilde{\mathbf{B}}$ is obtained as follows:

$$\tilde{\mathbf{B}} = \mathbf{R}^T \left[-\mathbf{N}_{3\times 8}\ \mathbf{N}_{3\times 8}\right] \tag{2.40}$$

The internal force vector is obtained by the equation ${}^{int}\tilde{\mathbf{f}} = \left\{-\tilde{\mathbf{f}}, \tilde{\mathbf{f}}\right\}^T$ with $\tilde{f}$ obtained as

$$\tilde{\mathbf{f}} = \int_{-1}^{1}\int_{-1}^{1} \tilde{\mathbf{B}}^T \mathbf{T}\, |r_3|\, d\eta_1 d\eta_2 \tag{2.41}$$

$\mathbf{T}$ is the interfacial traction vector. The tangent stiffness matrix is given as

$$\tilde{\mathbf{K}} = \begin{bmatrix} \mathbf{K}_s & -\mathbf{K}_s \\ -\mathbf{K}_s & \mathbf{K}_s \end{bmatrix} \tag{2.42}$$

with each submatrix $\mathbf{K}_s$ given as

$$\mathbf{K}_s = \int_{-1}^{1}\int_{-1}^{1} \tilde{\mathbf{B}}^T \mathbf{D} \tilde{\mathbf{B}} \left| r_3 \right| d\eta_1 d\eta_2 \tag{2.43}$$

where $\mathbf{D}$ is the interfacial material tangent stiffness matrix.

Further, the interfacial tangent stiffness matrix $\mathbf{D}$ can be written in the form of an incremental expression as

$$\delta T_i = \frac{\partial T_i}{\partial \Delta_j} \delta \Delta_j = D_{ij} \delta \Delta_j \tag{2.44}$$

For the Power Constitutive Law, the components of $\mathbf{D}$ are obtained by differentiation of Eq. 2.14 as follows:

$$D_{ij} = \frac{T_i^c}{\Delta_j^c} \left( \delta_{ij} - \frac{\bar{\Delta}_i \bar{\Delta}_j}{\tilde{w} \mu^{\alpha-\beta}} \left| \bar{\Delta}_j \right|^{\alpha-2} \right) \Theta \tag{2.45}$$

where $\delta_{ij}$ is the Kronecker delta, $\Theta$ is given by Eq. 2.12, and $\tilde{w}$ is defined by

$$\tilde{w} = \begin{cases} 1 & \text{if } \mathrm{d} = \mu^\beta \\ d & \text{if } \mathrm{d} > \mu^\beta \end{cases} \tag{2.46}$$

Considering the interpenetration, that is $\Delta_3 < 0$, the components $D_{13} = D_{23} = D_{32} = D_{31} = 0$, with the nonzero components given by Eq. 2.45. The component $D_{33}$ is related to the interpenetration and is obtained by differentiation of the compressive normal traction with respect to the normal relative displacement as follows:

$$D_{33} = K_0 \left(1 + \kappa \left|\bar{\Delta}_3\right|^{\beta}\right) \; Exp\left(\frac{\kappa \left|\bar{\Delta}_3\right|^{\beta}}{\beta}\right) \tag{2.47}$$

where $K_0 = T_3^c \; Exp\,(1/\beta)/\Delta_3^c$.

Note that the material tangent stiffness is unsymmetric for mixed-mode loading, and it is diagonal for single-mode delamination. The material tangent stiffness matrix has properties of an anisotropic material, one which has strong dependence on the displacement jumps in all the directions.

There are many computational issues associated with the interface element, and Goyal (2002) has written an entire chapter and explained in brief the issues of interpenetration and convergence techniques which have been incorporated in the current formulation, but left out from this thesis for the sake of brevity, a brief summary has been given by de Borst (2003) in which the mesh bias of the interface elements has been discussed with numerical examples.

### 2.2.2 Validation

Numerical simulations are presented for quasi-static loading of the Double Cantilever Beam (DCB) a Mode I fracture test specimen. The response from finite element configurations using interface elements have been compared to analytical solutions by Goyal (2002). To achieve a certain confidence in the current implementation of the interface element, a finite element simulation of the DCB was compared to an experiment carried out on an aluminum DCB under quasi-static loading by Josh Simón and Dr. David Dillard at the Adhesion Science Lab in the Department of Engineering Science and Mechanics (ESM). A detailed description of the instruments and the testing procedure, including the curing cycles for the different kinds of adhesive used in this study, can be found in the Master's Thesis of Josh Simón ( Simón (2004)).

The DCB test specimen is generally used for the characterization of Mode I fracture toughness. The geometry and the loading conditions of the DCB configuration are shown in Fig. 2.4. The experiment consists of a load that is applied at the end blocks jointed

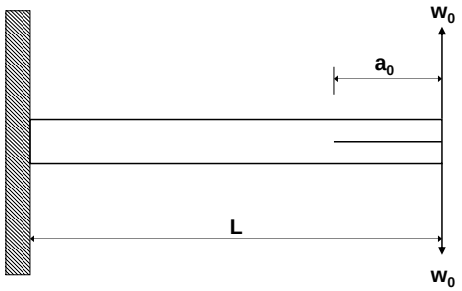


Figure 2.4: Loading conditions of the DCB configuration.

to the DCB specimen. The test is performed in a displacement controlled Instron 4500

series test frame with a 5kN load cell. All data was collected using custom software written with the LabVIEW software package. Specimens were loaded at a constant opening displacement rate of either 0.1mm/min or 1mm/min. Crack length was measured visually using the paper ruler that was bonded to the specimen during the preparation phase. Load and opening displacement were collected using the Instron's built-in data acquisition system. Test data was analyzed using the corrected beam theory approach, which accounts for root rotation, large deflections, and stiffening due to the end blocks. The critical strain energy release rate in Mode I is determined by

$$G_{I_c} = \frac{12\ F\ P_c^2\ (a\ +\ \chi_1\ h)^2}{w^2\ h^3\ E} \tag{2.48}$$

where $F$ is the correction factor for large rotations, $P_c$ is the critical load at the initiation of crack growth, $a$ is the crack length, $w$ is width of the specimen, $h$ is the thickness of one arm, $E$ is the modulus of elasticity of the arms, and the variable $\chi_1$ accounts for root rotation and deflection at the crack tip. The value of $\chi_1$ is deduced by taking the intercept of a plot of $(C/N)^{1/3}$ versus crack length,where $C$ is the compliance of the DCB specimen and $N$ is an end-block correction factor (Blackman *et al.* (1995)). The reaction forces are measured using the load cell.

An aluminum DCB bonded using LESA an adhesive, that is a product of the Dow Adhesive Company, was used in the experiment. The material properties for aluminum are listed in Table 2.1 and the interfacial material properties for LESA are listed in Table 2.2. The geometrical properties are the length L=203mm, the arm thickness $h$ =

Table 2.1: Mechanical properties for aluminum.

| $E_{11}$ | $\nu$ |
|---|---|
| 69 GPa | 0.3 |

Table 2.2: Interface properties for the LESA adhesive.

| $T_1^c = T_c^2$ | $G_{I_c}$ | $\beta$ | $K_a$ |
|---|---|---|---|
| 40 MPa | 1.6 N/mm | 1 | $10^6$N/mm$^3$ |

6.35mm, and width $B = 25.4$mm. The initial crack length $a_0$ is about 55mm.

Interface elements are positioned between the upper and the lower adherends. Crack growth is constrained in the plane between the upper and the lower adherend. Two-dimensional interface elements with contact properties are used to model the initial crack, and the interface elements with the softening law are positioned to simulate crack growth. The finite element model is shown in Fig. 2.5. The adherends are modeled using four-noded plain strain continuum CPE4I elements available in the ABAQUS library. Each

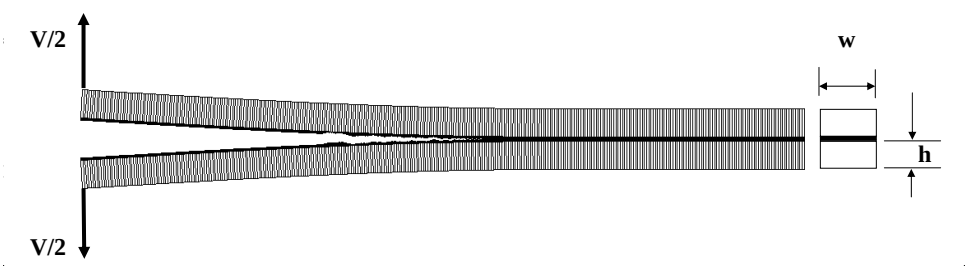


Figure 2.5: Finite element model of the DCB configuration.

adherend is modeled using one element across the thickness and 508 elements along the length. The mesh was chosen so that the length of the two-dimensional interface element does not exceed 0.5mm. The integration of the element internal force vector and element tangent stiffness matrix for the interface element is performed with six Gauss points. An incremental-iterative approach is adopted for the nonlinear finite element analysis and the Newtons method available in ABAQUS is used to trace the loading path of the DCB configuration with a displacement-control analysis. The finite element model of the DCB configuration consists of a total of 1016 CPE4I elements and 508 interface elements.

The load history from the finite element simulation is compared to the experimental results of this DCB configuration tested at a cross head speed of 0.1mm/min. The response of the DCB is shown in Fig. 2.6. For the quasi-static loading, the results are in excellent agreement with the experimental results. The crack growth history obtained from the finite element simulation is shown in Fig. 2.7. The crack tip was defined on the concept of traction free edges and in these finite element simulations, since in the exponential law used for the traction-displacement law the tractions would theoretically never be zero, we define a traction free surface when the traction is numerically negligible ($< 1 \times 10^{-6}$).

Figure 2.7 indicates that the crack growth is not instantaneous. Delving further into the matter, one can suggest by looking at Fig. 2.7 that in the displacement control test environment the crack would cease to grow if the test is stopped, meaning that no further displacement is applied to the arms of the DCB, at any given instant of time. Also, after

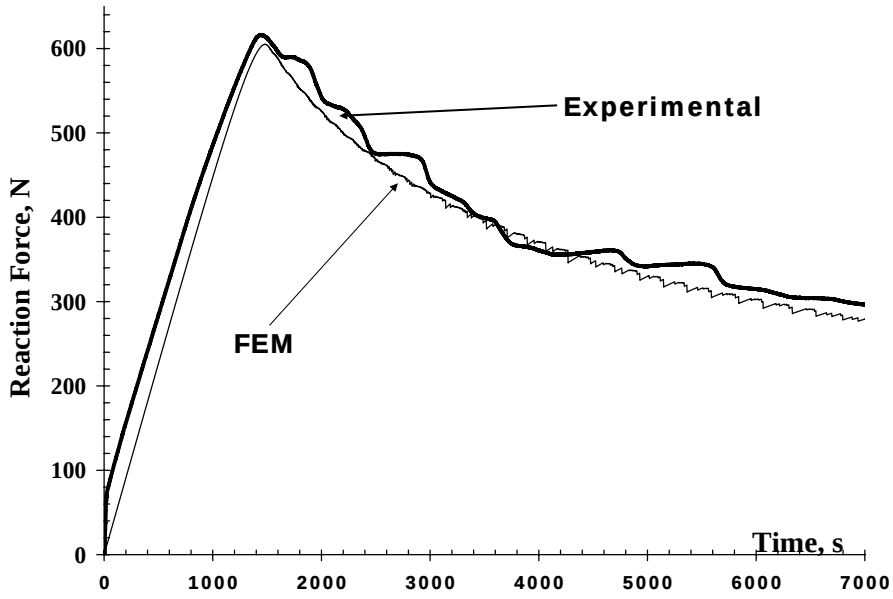


Figure 2.6: Comparison of the load history for DCB bonded with LESA adhesive.

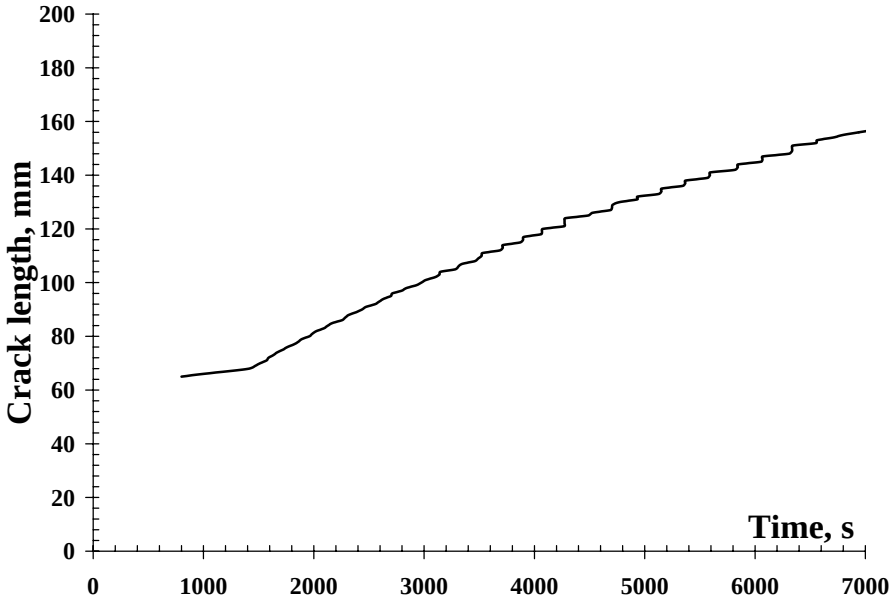


Figure 2.7: Crack growth history for DCB bonded with LESA adhesive.

the crack starts to grow initially it keeps growing for every incremental displacement applied to the arms of the DCB. It is important to understand the behavior of the crack growth, since this will form the basis of the classification of stable and unstable crack growth to be defined in the next section.

## 2.3 Behavior of Polymer Based Adhesives

There exists an entire research field to study the behavior of polymers, and different polymers are known to behave in different manners. Having verified the interface element with one kind of polymer based adhesive (LESA) in the previous section, we proceed to verify the DCB bonded with another kind of adhesive (SIA) manufactured by Sovereign Specialty Adhesives Inc. (Chicago, IL). The adhesive is a hardened epoxy based adhesive and is the one used for this study.

Experimental testing of the DCB configuration, shown in Fig. 2.4, bonded with SIA gave a totally different load history curve when compared to the DCB discussed in the previous section. A load history curve obtained experimentally for the DCB bonded using SIA is shown in Fig. 2.8, and Fig. 2.9 shows the crack growth that was observed visually during the experiment. Before comparing the results from the two different adhesives used, one must note that there is a difference between the cross head speeds in the two tests conducted. For the SIA adhesive, the tests were conducted at 0.1mm/min and 1 mm/min and there is no significant numerical difference in the load history or the crack

growth. Since both the cross head speeds can be considered quasi-static, a comparison is possible. Crack growth observed in the SIA adhesive is significantly different from that in the LESA adhesive. Based on this difference, we shall now attempt to classify stable and unstable crack growth.

Under a displacement-controlled test environment, the crack growth displayed two kinds of pattern, depending on the adhesive used. LESA showed a continuous crack growth and, as we discussed in the previous section, the growth was related to the incremental displacement applied to the arms of the DCB. This can be classified as ***stable*** crack growth. On the other hand, the crack growth was not continuous, but almost instantaneous in SIA over the length of the crack growth. The crack growth was almost instantaneous, or in other words the crack jumped from the initiation point to the arrest point. After each crack jump, the beam had to be opened to initiate the next jump. The two most significant observations here are: 1) at a specified incremental displacement, crack jumps were observed versus an incremental crack growth observed in LESA, 2) after the crack jump, an incremental displacement failed to produce an incremental crack growth. These observations lead to the classification of the crack growth in the SIA adhesive as an ***unstable*** crack growth. This is the definition that will be consistently used in further sections.

A finite element simulation of the aluminum DCB bonded with SIA was tried using only the interface elements in a manner similar to what was done for the DCB bonded with LESA. The geometrical properties are the length L=254 mm, the arm thickness $h$ =

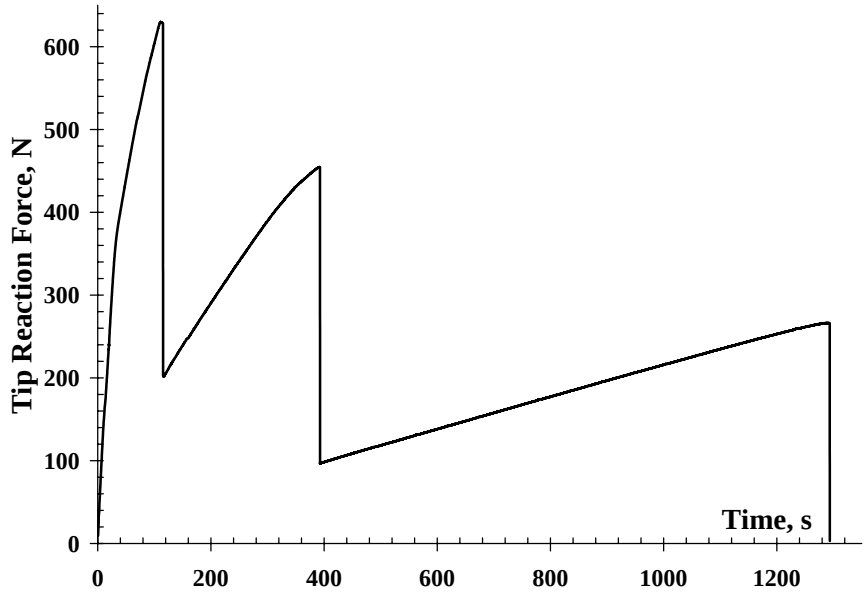


Figure 2.8: Tip reaction force history for a aluminum DCB bonded using SIA with an opening displacement of 1 mm/min

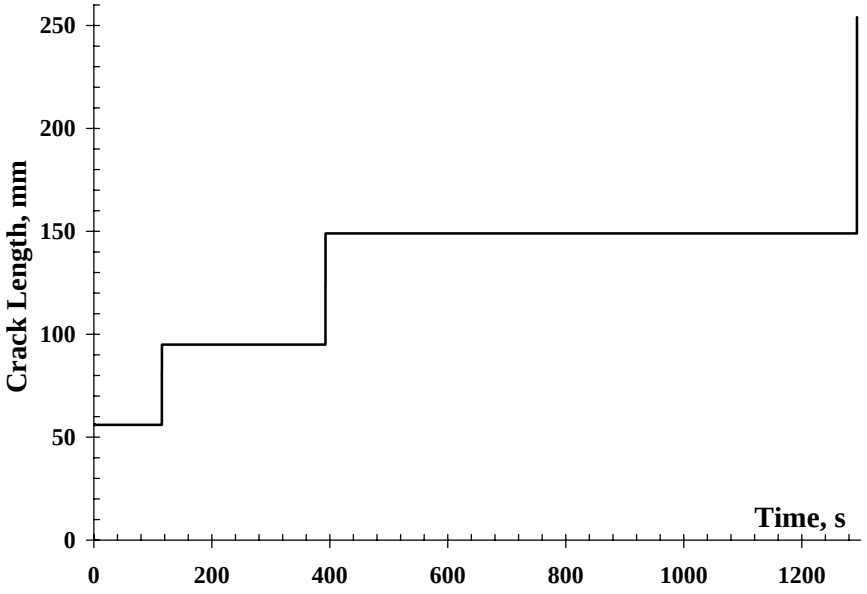


Figure 2.9: Crack length for the DCB bonded with SIA with an opening displacement of 1 mm/min.

6.35 mm, and width $B = 25.4$ mm. The initial crack length $a_0$ is about 55 mm. The material properties for aluminum are the same as shown in Table 2.1 and the material properties for the interface element are shown in Table 2.3. However this simulation

Table 2.3: Interface properties for the SIA adhesive.

| $T_1^c = T_c^2$ | $G_{I_c}$ | $\beta$ | $K_a$ |
|---|---|---|---|
| 47 MPa | 2.2 N/mm | 3 | $10^6$N/mm$^3$ |

failed to predict the unstable crack growth that was observed experimentally. Physically the simulation failed to capture the crack jumps observed in the experiments. Since $\beta$ has been defined as the brittleness, a couple more runs were done with higher values of $\beta$. These simulations too failed to capture the crack jumps. On a closer observation of the CZM, the physical effect of $\beta$ can be explained. In a CZM the critical strain energy $G_{I_c}$ and $\beta$ are specified as inputs and the critical opening displacement $\Delta_c$ is evaluated using Eqs. 2.2 and 2.3. Changing the value of $\beta$ just changes the value of $\Delta_c$, thereby initiating the crack growth at a higher applied displacement to the arms of the DCB. This change in $\Delta_c$ can be seen very clearly only when the traction-displacement law is plotted on a dimensional scale as shown in Fig. 2.10. The reaction histories obtained from the various runs clearly showed that the only effect of changing $\beta$ was the increase in the peak value of the reactions. The results are plotted in Fig. 2.11 along with the experimental results for the sake of complete understanding.

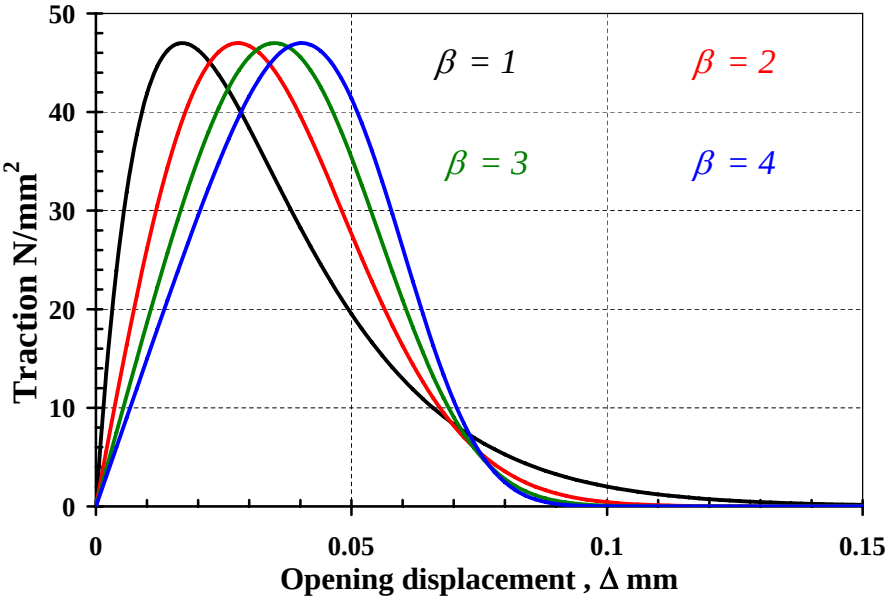


Figure 2.10: Traction-Displacement law for different values of $\beta$.

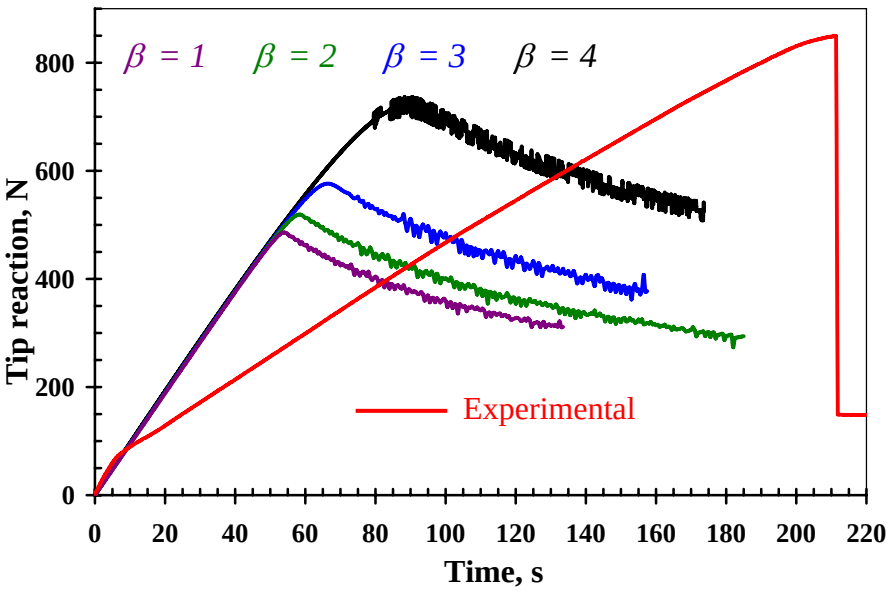


Figure 2.11: Reaction histories for different values of $\beta$.

The traction-displacement model was modified slightly by making an assumption that the $\Delta_c$ remains constant irrespective of the value of $\beta$. This facilitates the gradient of the softening portion to become more steep. Figure 2.12 illustrates this traction displacement law. Simulations run with this formulation allowed us to control the gradient of the softening part of the tip reaction histories, but a vertical drop in the reaction load was not possible to achieve. Furthermore, the crack jumps achieved in this simulations were nowhere near to the crack jumps observed in the experiments.

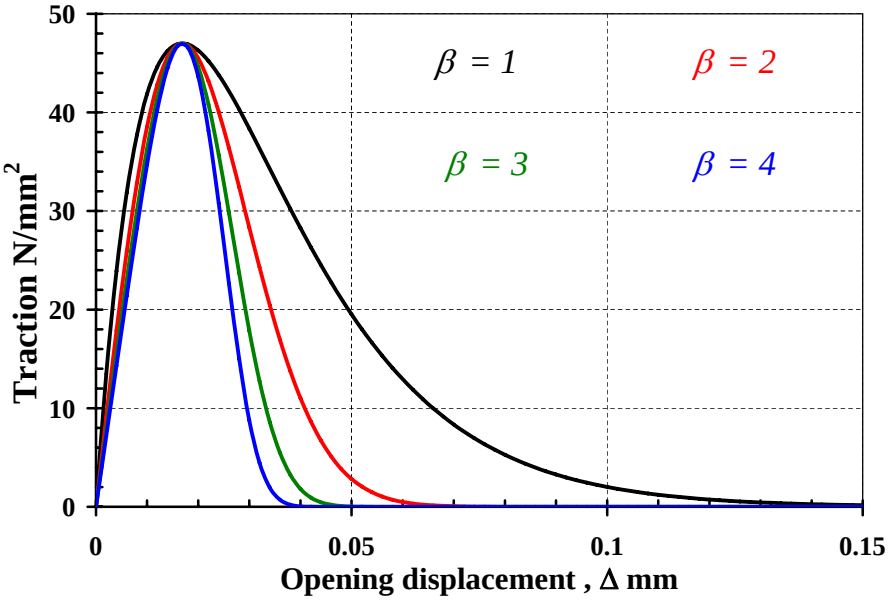


Figure 2.12: Reaction histories for different values of $\beta$.

Results from various models and simulations done led to the possibility that certain features about the crack growth were not being captured with the current model. The crack was allowed to grow along the plane defined by the upper and the lower adherends, which precludes the possibility of the crack moving along the thickness, which has been

reported before, or the possibility of multiple cracks being present in the adhesive at any given instant of time. The presence and growth of multiple cracks adds a completely new dimension to the problem under consideration.

To facilitate the presence of multiple cracks and the possibility of a crack moving along the thickness, a detailed modeling of the adhesive with bulk elements and interface elements has been created. Interface elements are placed along the edges of the bulk elements, as shown in a typical element configuration in Fig. 2.13. Three-noded triangular elements were used to model the adhesive with two-dimensional interface elements along each edge of the triangular elements. This allows the crack to grow from the crack tip in many different ways, as shown in Fig. 2.14. An input file was created with a total of ∼80,000 elements (both bulk and interface) just to model the adhesive. In addition, the detailed model created two interfaces, the first interface between the bulk elements used to model the adhesive and the second interface between the adhesive and the adherends. Considering the fact that a bimaterial interface would be weaker than the interface between a single homogeneous material, the interface properties for the bimaterial interface were reduced by about 20% as compared to the properties for the interface elements used between the bulk elements required to model the adhesive.

Under static simulations, the results were encouraging but not comparable to the experimental results. For different values of $\beta$, the tip reaction histories shown in Fig. 2.15 indicate that the crack propagated at high speeds. This conclusion is supported by the large drops of the reaction forces when the crack starts to propagate. It was encouraging

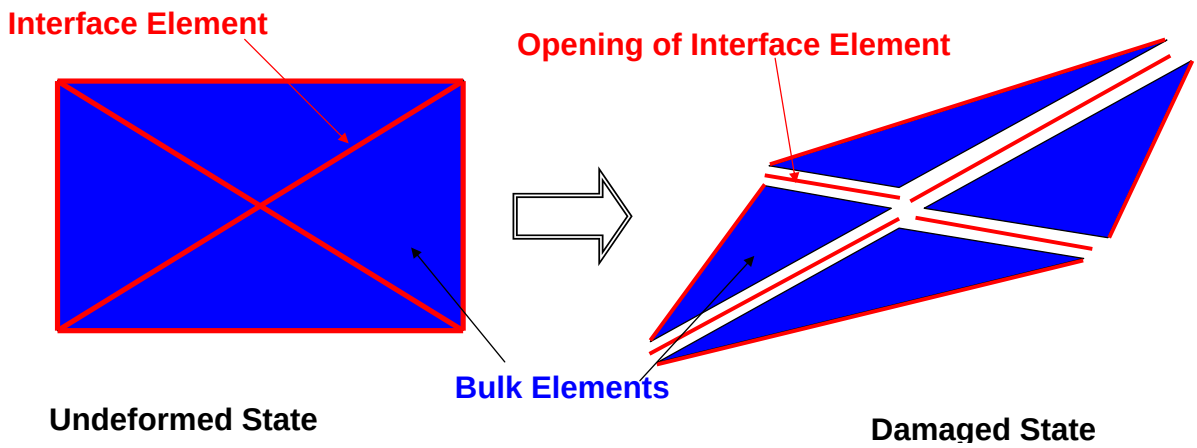


Figure 2.13: Arrangement of the interface element and the bulk element used to model the adhesive.

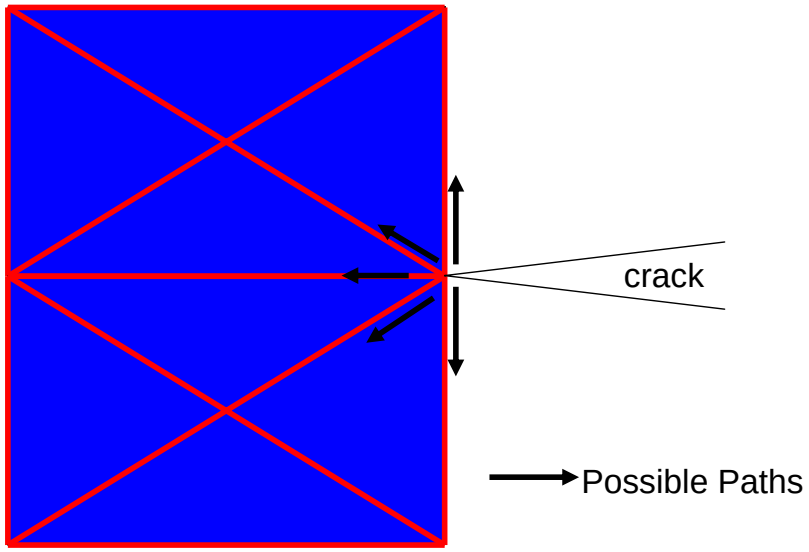


Figure 2.14: Possible crack growth paths with detailed modeling of adhesive.

in the sense that crack propagation at high speeds was achieved, but it was not almost instantaneous as we expected.

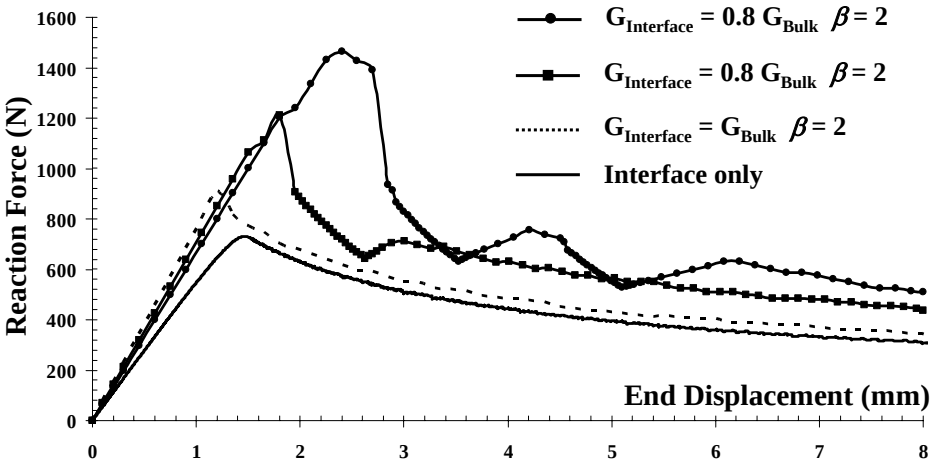


Figure 2.15: Reaction histories obtained using detailed modeling of the adhesive.

The only factor that was not considered in the simulations up till this point is the inertia effects. Since the tests were quasi-static, the inertia effects were neglected. However the instantaneous crack growth could induce certain dynamic effects in the beam. To study the dynamic effects, the formulation of the interface element has to be extended. The formulation and the time marching schemes are explained in the next section.

## 2.4 Dynamic Fracture Analysis

The interface element formulation is extended to facilitate the study of the effects of almost instantaneous crack growth and crack growth under dynamic loading conditions.

As discussed in the previous section, the almost instantaneous crack jump observed in a quasi-static DCB test can induce dynamic (inertia) effects on the adherends. A simple way to explain this would be the concept of a moving support. Consider a DCB specimen with a crack present. The length of the crack $a$ determines the length of the beam for the purposes of calculations. Note that beyond the crack length, the bending moment is zero. When the crack jumps, the length of the beam changes suddenly from $a$ to $a'$. This sudden change in length introduces dynamic effects similar to the ones experienced by a beam with a moving support. This dynamics could assist in the crack growth and this is being investigated here.

### 2.4.1 Formulation

The implementation of the element for use in the implicit dynamic procedure within the nonlinear finite element analysis code ABAQUS was performed by Hilber *et al.* (2001) using an implicit time marching scheme. Consider the finite element discretization discussed in the previous sections at time $t + \Delta t$:

$$M\ \ddot{u} + F^{int} - F^{ext} = 0 \tag{2.49}$$

where $M$ is the mass matrix, $\ddot{u}$ is the vector of nodal accelerations, and $F^{int}$ and $F^{ext}$ are the internal and external force vectors, respectively. The internal force vector consists of the tractions due to the CZM law. Following the procedure given by Hilber, the

equilibrium at time $t + \Delta t$ is replaced by a weighted average of equilibrium statements at times $t$ and $t + \Delta t$, respectively. This can be written as

$$r\left(\alpha, u_{t+\Delta t}\right) = M\ \ddot{u}_{t+\Delta t} + (1+\alpha)\left(F^{int}_{t+\Delta t} - F^{ext}_{t+\Delta t}\right) - \alpha\left(F^{int}_{t} - F^{ext}_{t}\right) = 0 \tag{2.50}$$

$\alpha$ is the intermediate step between the time steps $t$ and $t + \Delta t$, and the displacement at time $t + \Delta t$ is given by $u_{t+\Delta t}$. In addition to the above equation, the Newmark time integration formula forms the basis of the "predictor" and "corrector" step for the Newton-Raphson iterative algorithm. The tangent stiffness matrix, $\bar{K}^i_{t+\delta t}$, and the residual, $r^i\left(\alpha, u_{t+\Delta t}\right)$, used for the current iteration step $i$, are obtained by the linearization of the residual $r\left(\alpha, u_{t+\Delta t}\right)$ for the current iterative configuration as

$$\bar{K}^i_{t+\delta t} = (1+\alpha)\ K^i_{t+\delta t} + \delta\ \ddot{u}_{t+\Delta t} M \tag{2.51}$$

$$r^i\left(\alpha, u_{t+\Delta t}\right) = M\ \ddot{u}^i_{t+\Delta t} + (1+\alpha)\left(F^{int,i}_{t+\Delta t} - F^{ext,i}_{t+\Delta t}\right) - \alpha\left(F^{int,i}_{t} - F^{ext,i}_{t}\right) = 0 \tag{2.52}$$

Since the interface elements relate the tractions to the opening displacements across the nodes, no damping or mass are related to these elements. Also there is no external loading on these elements. Under these conditions, the equilibrium equations can be re-written as

$$\bar{K}^i_{t+\delta t} = (1+\alpha)\ K^i_{t+\delta t} \tag{2.53}$$

$$r^i\left(\alpha, u_{t+\Delta t}\right) = (1+\alpha) F^{int,i}_{t+\Delta t} - \alpha\ F^{int,i}_{t} \tag{2.54}$$

The equations derived above for the implicit time marching scheme are implemented in ABAQUS. Before proceeding to simulate the aluminum DCB with the high fidelity model for the adhesive, a validation of the dynamic code was done with results available in literature. These results are discussed in the next section.

### 2.4.2 Validation

Dynamic crack growth along an elastic double cantilever beam (DCB) has been studied to verify the implicit dynamic cohesive element procedures described. An elastic DCB specimen is opened at its free end at a specified constant velocity, leading to the crack-tip propagating at a nonuniform velocity. An approximate analytical solution under small deformation assumptions using the Euler-Bernoulli beam theory was given by Bilek and Burns (1974). The solution predicts that the quantity $a^2(t)/t$ remains constant, where $a(t)$ is the crack length at time $t$.

The geometry and the material properties used for this analysis are taken from Rahul-Kumar *et al.* (2000b) and are reproduced here for the sake of completeness: height (h) = 0.25m, width(w) = 0.125m, opening velocity = 31.62m/sec, E = 100GPa, and density $\rho$= 2000kg/m$^3$. To achieve a constant value for the ratio of $a^2/t$, we had to model a beam with a length of 20m. The properties of the cohesive elements used are $\Gamma_0 = 10^6$ N/m and $\delta_{cr} = 0.01$m. A 3D model was generated in ABAQUS for the simulation, and

the crack length was evaluated based on the equation:

$$\left[1 - \left(1 + \frac{\Delta_n}{\delta_{cr}}\right) Exp\left(-\frac{\Delta_n}{\delta_{cr}}\right) Exp\left(-\frac{\Delta_{t1}^2 + \Delta_{t2}^2}{\delta_{cr}^2}\right)\right] = 1 - \frac{2}{e} \tag{2.55}$$

where $\Delta_n$ is the normal opening displacement, $\Delta_{t1}$and $\Delta_{t2}$ are the tangential opening displacements, $\delta_{cr}$ is the critical opening displacement, and $e$ is the Euler constant. The converged time step used for this simulation was $\Delta t = 1 \times 10^{-8}$ sec. The ratio of $a^2/t$ is plotted and compared with the semi-analytical results in Fig. 2.16. The results compare well with the semi-analytical results, thus validating the formulation and implementation of the interface element for dynamic simulations.

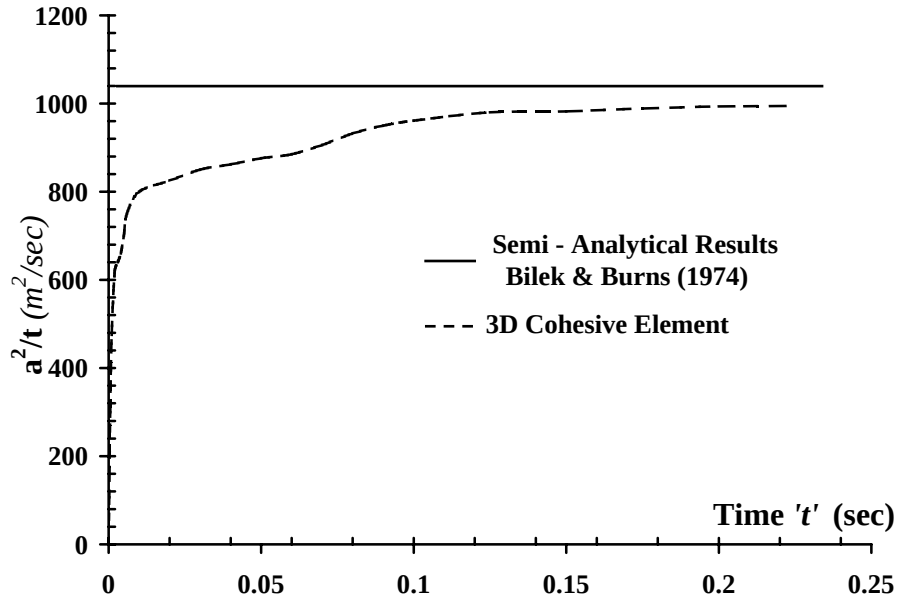


Figure 2.16: Dynamic crack growth comparison with semi-analytical results.

## 2.5 Detailed Modeling of Bulk Adhesive Including Dynamic Effects

In the previous section the dynamic formulation for the interface element has been discussed and validated against semi-analytical results. Having validated the code, attention was refocused on the problem of simulating the aluminum DCB bonded with SIA as discussed in section 2.3. The same simulation was run again including the inertia effects. The crack growth was monitored and as expected the crack jumps were being captured. However, since the crack jumps were almost instantaneous, the time step requried to capture these were very small, of the order of $1 \times 10^{-12}$ sec. This, in addition to the fact that ∼80,000 elements were being used to model the adhesive, made the simulation computationally very expensive. An adaptive time step scheme based on the residual force vector available in ABAQUS was used. The results took about two weeks to generate on a DUAL 64 bit AMD 1800+ processor with 2 GB of RAM working with the LINUX operating system.

The tip reaction obtained from the simulation is compared to the experimental load histories in Fig. 2.17. To capture the load drop, the time steps required are of an order of $1 \times 10^{-12}$ sec as mentioned earlier and the reaction forces are quite oscillatory during this period. As can be seen from Fig. 2.17, the reaction force overshoots by about 80% and drops down to zero. The oscillations can be clearly seen by zooming into the region of interest. This is done by plotting the reaction force for about $1/10^{th}$ of a second after

the crack starts to propagate. This plot is shown in Fig. 2.18. Achieving the drop is just one part of the simulation. The results have to be correlated to the physics of the problem, which means that the simulation should have given the drop in the reaction due to the crack jumps. The crack jumps were verified and two snapshots taken from the post-processing of the simulation at an interval of $1\mu s$ are shown in Fig. 2.19. Also the first snapshot shows that initially there are two crack paths and after a certain time one becomes dominant and begins to grow.

## 2.6 Difficulties in Detailed Modeling of Bulk Adhesive

This chapter has dealt with the difficulties in modeling instantaneous crack growth observed in the SIA adhesive. Various simulations with different parameters were tried to model this and these have been explained here. We saw that the high fidelity modeling of the adhesive including inertia effects was able to capture the crack jumps. However, for reasons which are explained here, the high fidelity modeling is purely an academic solution with little or no practical use.

The first concern one could raise is the size of the model. For a simple configuration like the DCB, about 80,000 elements were used to model just the adhesive. Increasing the size of the problems requires higher computational power, especially the RAM. Problems

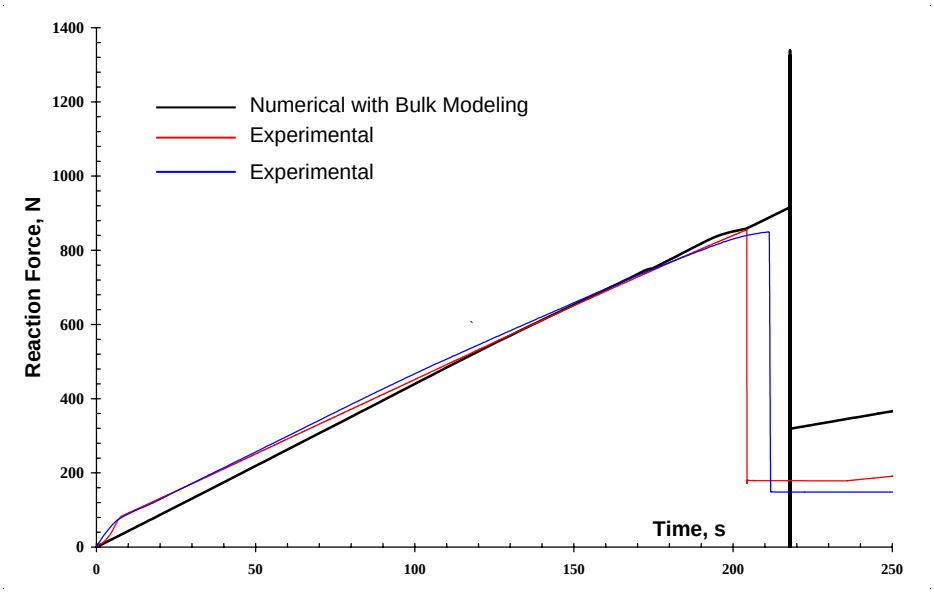


Figure 2.17: Tip reaction history compared to experimental load histories.

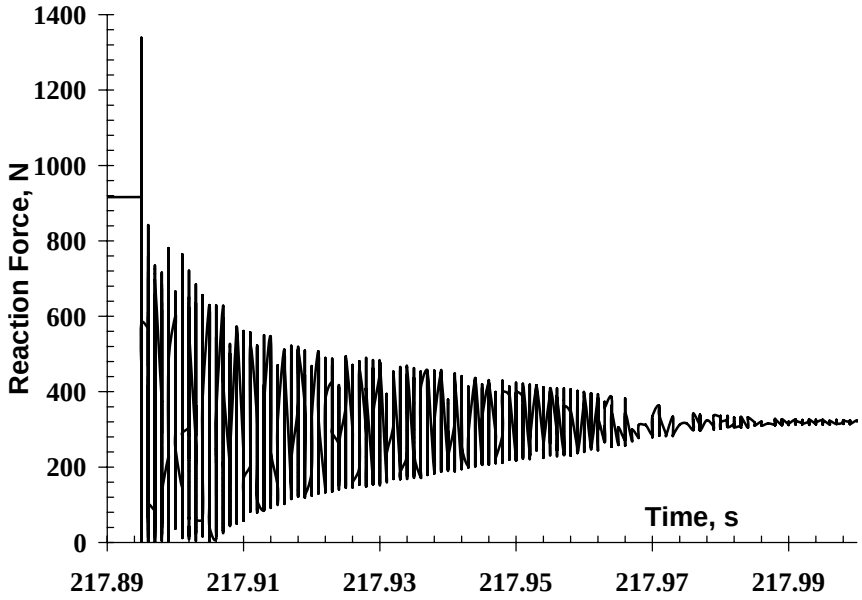


Figure 2.18: Oscillations in tip reaction when crack growth occurs.

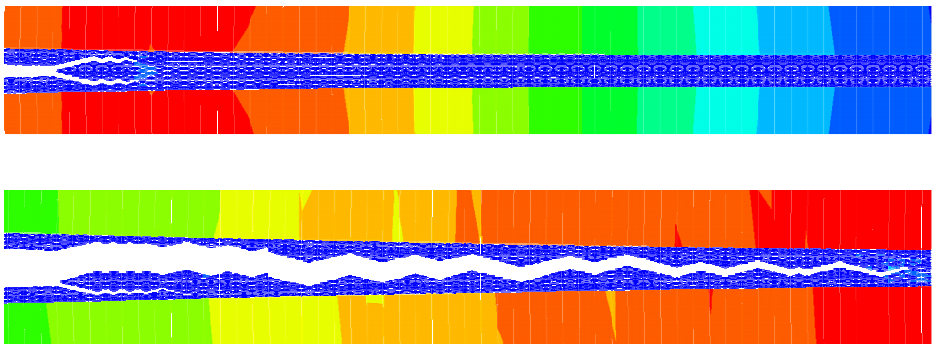

Figure 2.19: Snapshots taken at an interval of $1\mu s$ to show the crack jumps.

of practical importance would become increasingly hard to solve due to the restrictions of the computational power. The second and probably the more important difficulty is the generation of the input file. No available preprocessor allows for the modeling of the bulk elements with interface elements along all the edges. So for the DCB the input file was generated from a FORTRAN code, which took about two weeks to write. This implies that every time the problem is changed, a code would have to be written to create an input file and for complex geometries, meshing is a different field of research all together.

In the next chapter, alternative solution techniques will be proposed and tested to circumvent these difficulties.

# Chapter 3

# Rate Dependent CZM Modeling

## 3.1 Introduction

Polymeric adhesives exhibit viscoelastic behavior and these rate dependent properties can influence the global response to fracture and cause both the type and the extent of damage to depend on the time scale of the applied load, *i.e.*, the rate at which the load is applied ( Popelar and Kanninen (1980)). In the previous chapter, finite element simulations of an adhesively bonded aluminum double cantilever beam (DCB) conducted under quasi-static, displacement controlled loading were presented. Fast crack growth, or stick-slip behavior, resulted in an abrupt decrease in the reaction force. We attempted to account for this stick-slip fracture in the adhesive by including inertia effects, but using a rate independent CZM for the interface elements. Reasonable correlation between the

simulations to the test data was achieved if the adhesive was modeled using both the bulk material elements and interface elements in the epoxy. However, the computational times for these high-fidelity simulations were very long. It is preferable to represent the adhesive with only interface elements to reduce the model size in the anticipation of simulating fracture events in more complex automotive structures. A rate dependent CZM for the epoxy seemed to be a reasonable approach to capture the fundamental fracture behavior, and to simultaneously permit reduced model size.

Extensive studies have been made to incorporate rate dependent models for polymers by Corigliano and co-researchers in a series of papers ( Corigliano and Ricci (2001), Corigliano and Mariani (2001), Corigliano and Mariani (2002), Corigliano *et al.* (2003)). Materials may exhibit increased resistance to fracture under high crack speeds, *i.e.*, the value of $G_{I_c}$ increases with the increasing crack speed or crack opening velocity. Increasing critical strain energy release rate with increasing crack opening velocity has been the basis of most rate dependent CZM models available in the literature including the ones mentioned above and rate dependent models proposed by Landis *et al.* (2000) to study the crack velocity dependence on rate,and Kubair *et al.* (2003), Danyluk *et al.* (1998), Zhang *et al.* (2003), Zhang *et al.* (2003) to study the dynamic crack growth. A comprehensive study both experimentally and numerically has been done in a two series paper by Xu *et al.* (2003a) and Xu *et al.* (2003b). Rate dependent effects have also been studied in composite materials by many authors, namely Cantwell and Youd (1997), Singh and Parameswaran (2003), and Nemes and Randles (1994). The idea of reducing $G_{I_c}$ with

increasing crack speed has been mentioned in literature by Maugis and Barquins (1987) when they discussed peeling of tapes and by Mataga *et al.* (1987) when the authors studied the crack tip plasticity in dynamic fracture, both these studies suggested a schematic variation of the fracture toughness as a function of velocity which is shown in Fig. 3.1. Most of the studies mentioned above develop their models on the initial part of the curve where the slope is positive. The implementation of a model on the negative slope has not been done so far, in view of the author's knowledge.

However, SIA, a two part, elevated cure epoxy, used in this study exhibited a decrease in

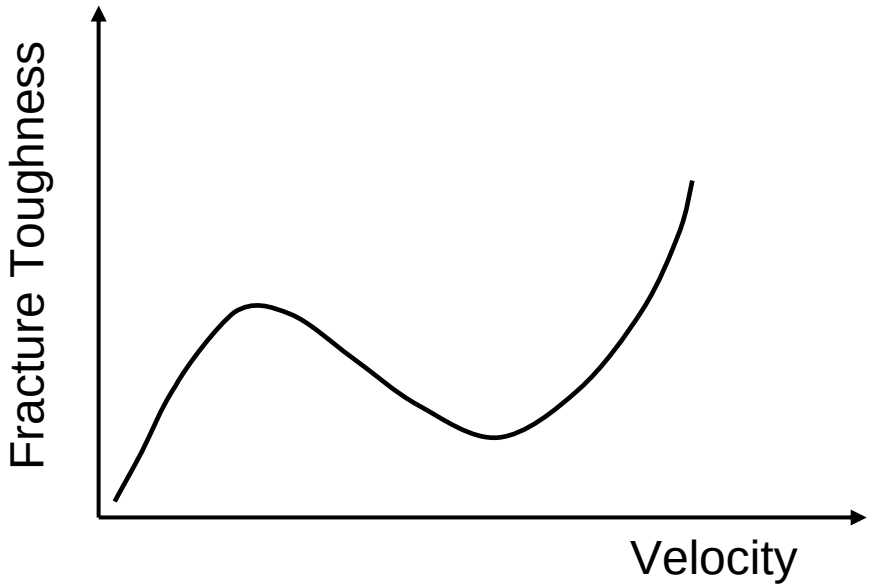


Figure 3.1: Schematics of typical non-monotonic fracture toughness-crack velocity curve.

the critical strain energy release rate with an increase in the loading rate. This behavior was observed when compact tension tests were carried out on the neat adhesive specimens at the Oak Ridge National Laboratory (ORNL). Use of the existing rate dependent

models violates the mechanical behavior of the SIA adhesive, thereby rendering the existing models unsuitable for the SIA adhesive. This leaves us no choice but to develop a rate dependent model which predicts the mechanical behavior of the material accurately. Results of the compact tension test will be the starting point for the formulation of the rate dependent model. The compact tension test and the results will be discussed in detail and the formulation of two rate dependent models based on these results will be explained in further sections. Implementation of one of the rate dependent models to study the quasi-static testing of aluminum DCB bonded with SIA in ABAQUS, and comparison of the results from this simulation with experimental results, will constitute the last section of this chapter.

## 3.2 Compact Tension Tests

A number of test methods have been implemented to measure the fracture energy of adhesives for many applications. Neat resin adhesive samples may be characterized just like other polymers, using common configurations such as the compact tension (CT) or single edge notch bend (SENB) specimens. Quasi-static test standards (ASTM-D5045-99 1999) exist for these geometries, and practitioners have extended the methods to higher rates of testing. The SENB specimen appears to be more popular in the literature for characterizing the impact behavior of polymers, perhaps because of the convenience of doing such tests in drop towers. The CT specimen has also been used in conjunction

with high speed servo-hydraulic test frames, however, when a wider range of test rates is desired ( Béquelin and Kausch (1995); Plummer *et al.* (2004)).

Specimen preparation and the compact tension tests were conducted at the Oak Ridge National Laboratory (ORNL). The adhesive used is designated as PL731SI, a commercially available, two-part epoxy system produced by Sovereign Specialty Adhesives Inc. (Chicago, IL). Compact tension specimens were cut from neat adhesive plaques 8 mm thick and 27 mm square. The plaques were consolidated between stainless steel plates following a curing procedure based on discussions with the manufacturer. Working drawings for the compact tension test specimen are shown in Fig. 3.2, and Fig. 3.3 shows the actual photographs of the specimen before and after the test.

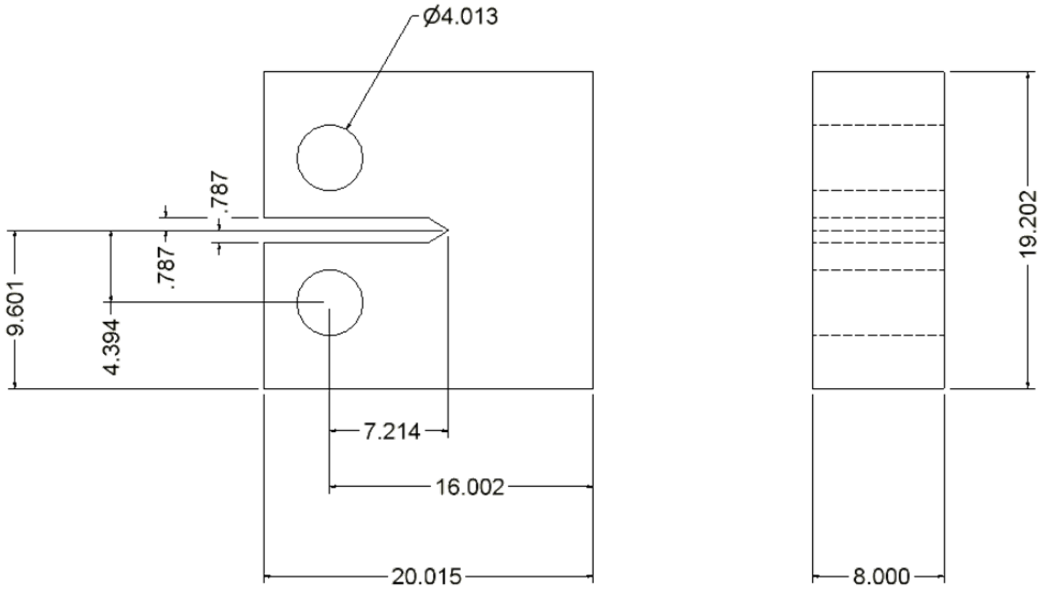


Figure 3.2: Working drawing of the compact tension test specimen prepared at Oak Ridge National Laboratory (ORNL), all dimensions are in mm.

The test with different loading speeds starting from quasi-static up to 1 m/s were per-

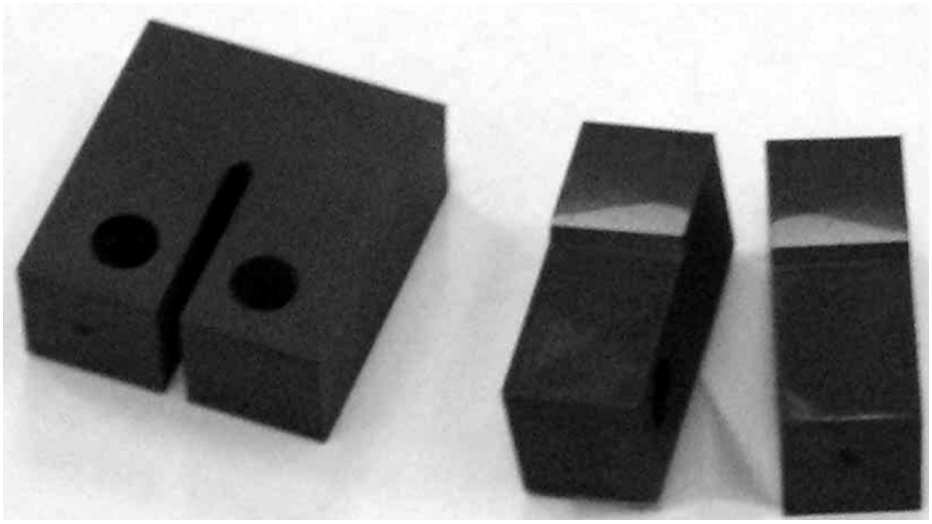

Figure 3.3: Photographs of the compact tension test specimen before and after testing.

formed. The compact tension tests were performed using the quasi-static test standard ASTM-D5045-99. Other researchers were followed in extending this method to higher rates of testing. A servo-hydraulic machine was used for the testing at speeds up to 1 m/s. A 5000 N strain gage-based load cell was used to measure loads. Data were acquired at sampling rates of up to 25,000 per second using a data acquisition card in a computer running custom LabVIEW® codes. Modifications to the load train were made to improve results for the higher rate compact tension tests. In order to minimize the mass of the load train between the specimen and load cell, a short section of threaded rod was used to attach a small aluminum clevis directly to the load cell, which was in turn mounted to the upper, stationary cross head. The lower clevis was attached to a small slack adaptor (also known as a lost motion device) to allow the actuator to get up to the setpoint velocity prior to engaging the specimen. The Mode I stress intensity

factors were determined from the load-displacement plots in accordance with the ASTM standard D50445-99.

The results of the CT are presented in Fig. 3.4. As can be seen from Fig. 3.4, the fracture toughness decreases with increasing test speeds. Based on these results, one can safely assume that the critical strain energy release rate will reduce with an increase in the crack tip opening velocity $\dot{\Delta}$. However, this is contradictory to what has been reported in the literature for rate dependent models cited in section 3.1.

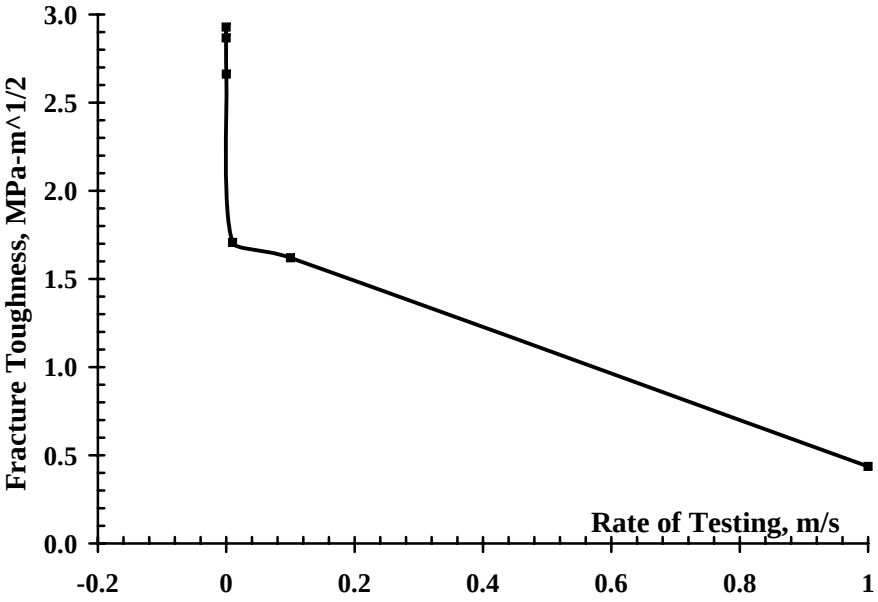


Figure 3.4: Fracture toughness variation obtained using the compact tension test at ORNL.

To develop a rate dependent model, the information that needs to be established is the variation of the critical strain energy release rate $G_{I_c}$ with the rate of opening displacement $\dot{\Delta}$. The CT tests give us the variation of $G_{I_c}$ with respect to the rate of testing. To establish the desired correlation, simulations of the CT were performed in ABAQUS®

at a specified rate of testing and $G_{I_c}$. The complete procedure is explained in detail in the next section. However the tests were carried out at a few discrete cross head speeds. Simulation required intermediate test speed data for more accurate estimate of the rate dependent model. The intermediate data was obtained by fitting a third order polynomial to the CT data plotted on a log-log scale. Figure 3.5 shows the original data and the polynomial fit.

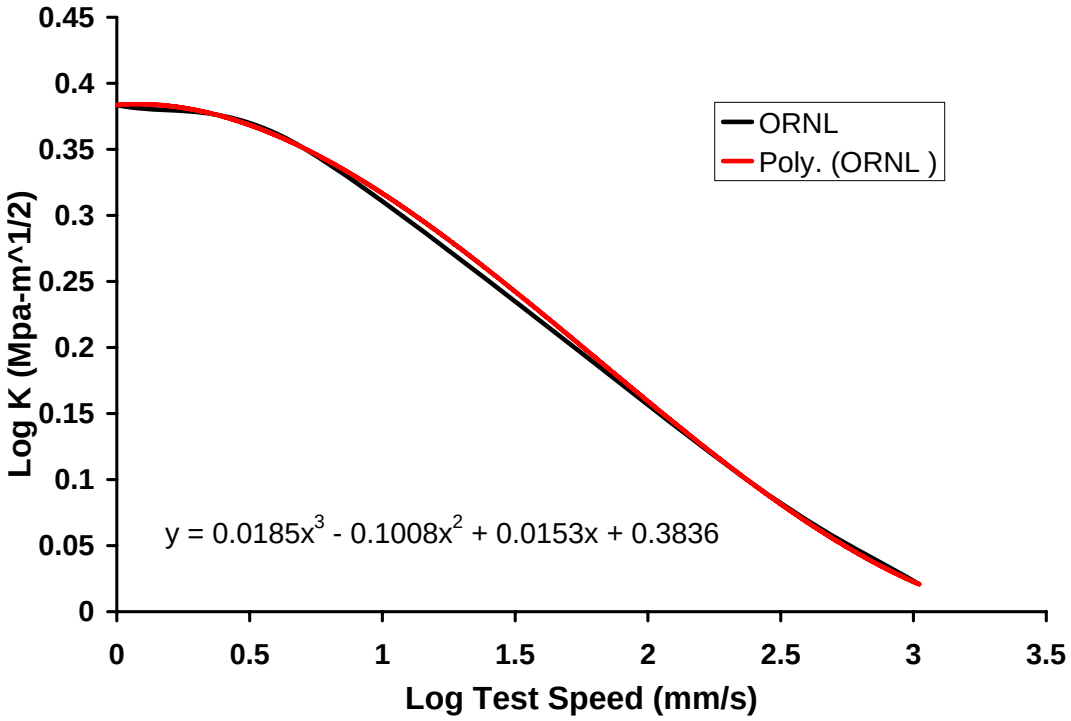


Figure 3.5: Log-Log plot of the fracture toughness $K$ with the test speed, along with the polynomial fit.

## 3.3 Compact Tension Test Simulation in ABAQUS

The rate dependent model has to be established from the compact tension tests, which give a relation between $G_{I_c}$ and the cross head speeds. In a rate independent CZM the tractions are specified as a function of the opening displacement $\Delta$. For the CZM to be rate dependent, the traction not only has to be a function of the opening displacement $\Delta$, but also a function of the rate of opening displacement $\dot{\Delta}$. The simulation of the compact tension test in ABAQUS® will allow us to establish a relation between $G_{I_c}$ and $\dot{\Delta}$. Since the integral of the traction displacement law is the critical strain energy $G_{I_c}$ as given by Eq. 2.2, we need to find the additional relation between traction and rate of opening displacement $\dot{\Delta}$. This section will explain step by step the procedure we have adopted to establish this relationship.

The first part of the procedure as mentioned above is the establishment of a relationship between the critical energy release rate $G_{I_c}$ and the rate of the opening displacement $\dot{\Delta}$. Experimental data from ORNL and the interpolation polynomial fitted to the experimental data give us the variation of $G_{I_c}$ with respect to cross-head speed. This information is sufficient to run a simulation of the compact tension test in ABAQUS® for a set of $G_{I_c}$ and corresponding cross-head speed. During the simulations, the maximum value of $\dot{\Delta}$ can be monitored in all the interface elements. The measurement of $\dot{\Delta}$ is explained in more detail in the following section. So, for each simulation that is done in ABAQUS®, the maximum $\dot{\Delta}$ corresponds to the specified value of the $G_{I_c}$. Simulations for different

set of values for $G_{I_c}$ and cross-head speed will allow us to establish a function between $G_{I_c}$ and $\dot{\Delta}$.

### 3.3.1 Finite Element Model for CT

Finite element simulations of the CT were done in ABAQUS® to measure the maximum $\dot{\Delta}$ in the interface element. The interface elements were placed horizontally along the notch. The size of the interface element was kept to 0.1mm. Fig. 3.6 shows the placement of the interface element in the finite element model of the compact tension test specimen. The elements have zero thickness and have been represented by the symbol $\times$ in the figure. To maintain the length of the interface element to 0.1mm and to have a well-defined mesh, the CT specimen was discretized using ~32,000 triangular elements.

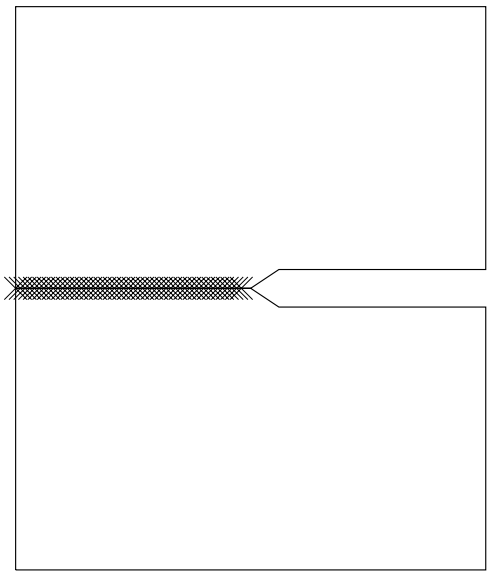

Figure 3.6: Placement of the interface element in the compact tension test in a finite element simulation performed using ABAQUS®.

The rate of the opening displacement, $\dot{\Delta}$, is measured in the interface element in front of the crack tip. As the crack propagates through the interface element, the maximum value of $\dot{\Delta}$ which was attained in the interface element while the crack passed through it is recorded. Consider that, in the undeformed configuration, $\boldsymbol{U}$ be the set of interface elements in front of the notch. As the CT specimen is loaded, $\dot{\Delta}$ reached at each Gauss point in each element of the element set $\boldsymbol{U}$ is measured. $\dot{\Delta}$ is measured at a particular Gauss point till the crack tip passes the Gauss point; in other words, there is no significant traction offered at this Gauss point due to the opening displacement (*i.e.* a traction free surface is established). When the traction offered is lower than $1 \times 10^{-6}$ N, the assumption of traction free surfaces is implemented. The maximum value of $\dot{\Delta}$ measured at a particular Gauss point in the element set $\boldsymbol{U}$ is written. After the simulation is complete, the average of all the maximum $\dot{\Delta}$ values recorded at each Gauss point is taken and this average value of $\dot{\Delta}$ corresponds to the $G_{I_c}$ and cross head speed. Figure 3.7 shows the variation of the maximum $\dot{\Delta}$ recorded as the crack grew in one of the ABAQUS® simulations carried out for a specified $G_{I_c}$ of 0.5 N/mm and a cross head test speed of 0.8m/s. As can be seen from Fig. 3.7, the variation of the data about the mean is within 5%.

The simulations were performed for speeds ranging from nearly 0mm/sec (quasi-static) up to 50 mm/s with an increment of 5 mm/s and then up to 1m/s with an increment of 25 mm/s. A value of $\dot{\Delta}$ was obtained for each of the simulations and a graph of the rate of opening displacement is plotted against the value of the critical energy release rate in

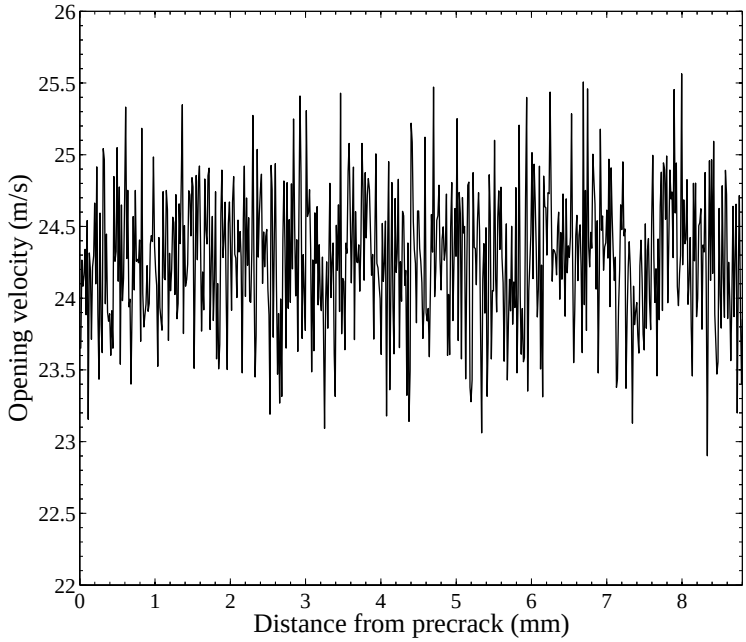


Figure 3.7: Maximum opening velocity measured at Gauss points in the compact tension test simulations.

Fig. 3.8. As predicted, Fig. 3.8 shows that the critical strain energy reduces as the rate of opening displacement increases. The drop is very fast initially and then the value of $G_{I_c}$ tends to stabilize down to the lowest value measured in the experiments.

Having established a discrete set of points for $G_{I_c}$ and $\dot{\Delta}$, a curve can be fit through these points to establish a continuous relation. The graph shown in Fig. 3.8 looks similar to one half of a Sigmoid function. Taking advantage of this fact, a modified Sigmoid function is used to express the fracture toughness as a function of the rate of the opening displacement. Non-dimensional parameters are defined as

$$\bar{\dot{\Delta}} = \left( \frac{\dot{\Delta} - \dot{\Delta}_q}{\dot{\Delta}_q} \right) \tag{3.1}$$

$$\bar{G} = \frac{G_{I_c}}{G_{min}} \tag{3.2}$$

The modified Sigmoid function used to express the relationship between two non-dimensional parameters $\bar{G}$ and $\bar{\dot{\Delta}}$ is shown in Fig. 3.8. One can, after looking at the curve fit, argue that a closer curve fit can be achieved using some other fit to the data, but the goal here is not only to capture the trend of the rate dependent model but also to have a model which can be implemented in a finite element formulation without much difficulty. Effects of this trend on simple fracture specimens is one of the objectives of this study. The equation for the curve fit is

$$\bar{G} = 1 + \frac{A}{\left( B + Exp\left( \xi \left[ \bar{\dot{\Delta}} \dot{\Delta}_q + \dot{\Delta}_q \right] \right) \right) G_{\min}} \tag{3.3}$$

where $A$, $B$, and $\xi$ are constants of curve fitting and they control the shape of the modified Sigmoid function. The numerical values for these are 83, 50, and 0.5, respectively. To keep consistency in the units, we take $\xi$ to have the units of s/mm and $A$ to have the same units as the fracture energy. $G_{min}$ is the minimum value of $G$ obtained from the experimental data. The data from the simulation and the modified Sigmoid function are plotted together in Fig. 3.8.

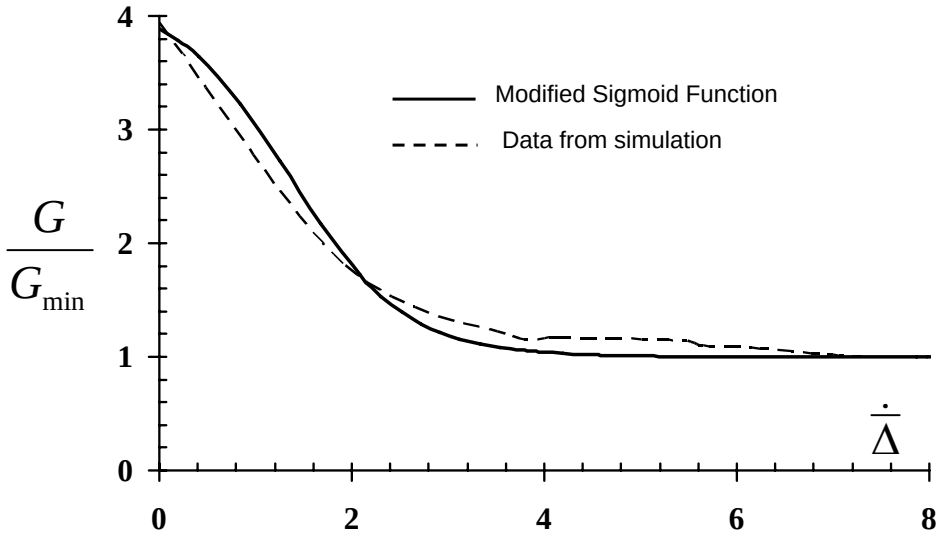


Figure 3.8: Data for $G_{I_c}$ as function of $\dot{\Delta}$ obtained from finite element simulation of a compact tension test and the curve fit.

## 3.4 Formulation of Rate Dependent Models

Until this point the variation of the critical energy release rate with the rate of the opening displacement has been established. However, in the CZM, the critical energy release rate

$G_{I_c}$ needs to be specified and the critical opening displacement $\Delta_c$ is calculated based on this and the maximum strength $T_c$ as given by Eq. 2.2. The value of $\beta$ needs to be specified too. This makes the critical energy release rate a function of two independent variables, $\beta$ and $\Delta_c$, which leads to two possible rate dependent models. The derivation of these two models will be discussed in detail in this section.

### 3.4.1 Rate Dependent Model I ($\Delta_c = F(\dot{\Delta})$)

Of the two independent variables that were discussed in the previous section, here the derivation of the rate dependent model based on the assumption that the brittleness parameter $\beta$ is a constant and the critical strain energy release rate $G_{I_c}$ is now only a function of $\Delta_c$ is given. This is equivalent to saying that the critical opening displacement is a function of the rate of the opening velocity. Since $\Delta_c$ can be expressed explicitly in terms of $G_{I_c}$ and $\beta$, we can explicitly express $\Delta_c$ as a function of $\dot{\Delta}$. Consider the two equations, Eqs. 2.2 and 3.2. Rearranging yields

$$\Delta_c = \frac{G_{min} \; + \; \frac{A}{B \; + \; Exp\left(\xi \; \dot{\Delta}\right)}}{T_c \psi} \tag{3.4}$$

The establishment of this relation allows us to plot the traction as a function of $\Delta$ and $\dot{\Delta}$ provided a value for $\beta$ has been assumed. A surface plot is done for a value of $\beta = 1$ for a better understanding and is shown in Fig. 3.9. Units on the graph have to be noted carefully as they are different for the opening displacement and the rate of opening

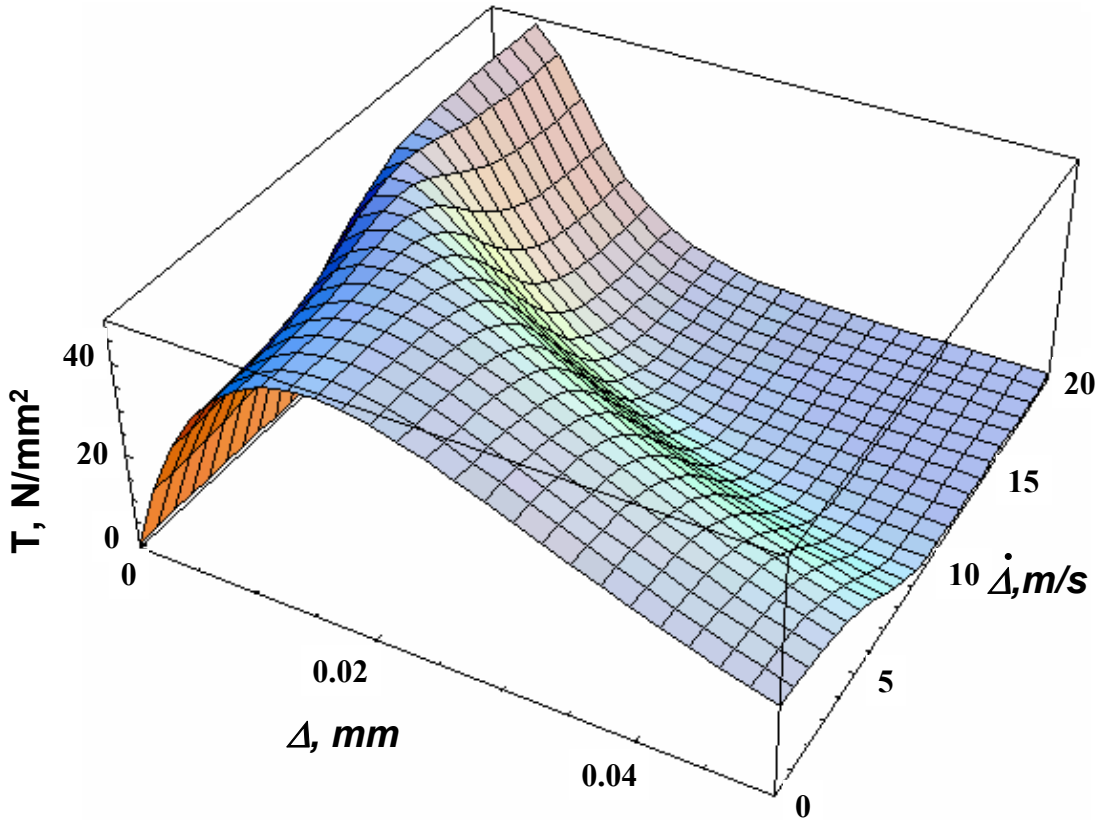


Figure 3.9: Rate dependent model I with $\Delta_c = F(\dot{\Delta})$.

displacement.

### 3.4.2 Rate Dependent Model II ($\beta = F(\dot{\Delta})$)

Since $\beta$ cannot be expressed explicitly in terms of $G_{I_c}$, the values of $\beta$ for different values of the critical energy release rate have to be found numerically. Once again, to obtain the relation between $\beta$ and $G_{I_c}$, a curve fitting was done to this data and the results are shown in Fig. 3.10. It can be seen that at a certain point $\beta$ starts to increase very rapidly as $G_{I_c}$ decreases. The rate dependent CZM law for this case can be understood

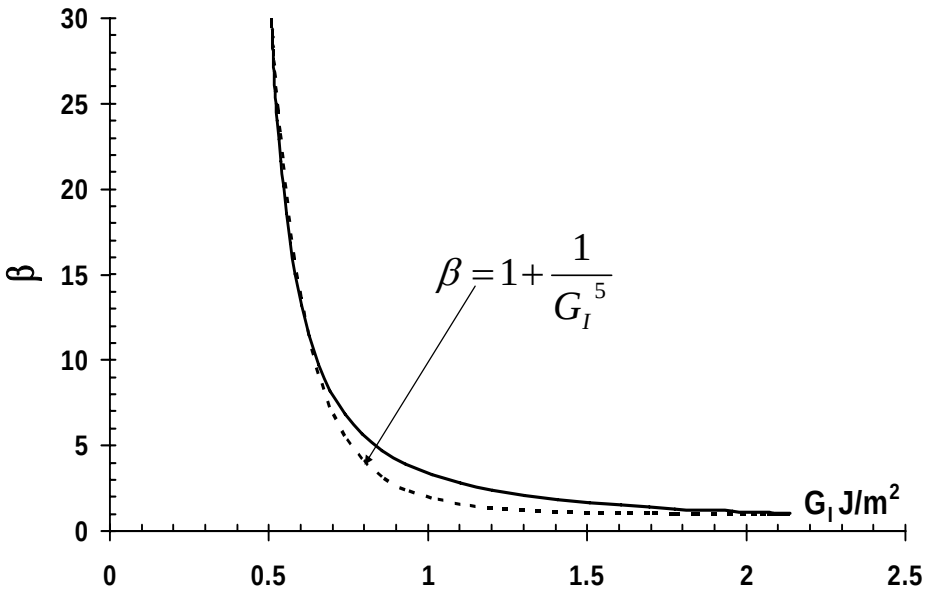


Figure 3.10: $\beta$ as a function of $G_{I_c}$.

more clearly by plotting a 3D graph as was done with the first model. Figure 3.11 shows this plot and, as can be seen, this model has very high gradients as compared to the first model and will be much more expensive to be used to obtain numerical results that have

converged, if at all possible, in an implicit code.

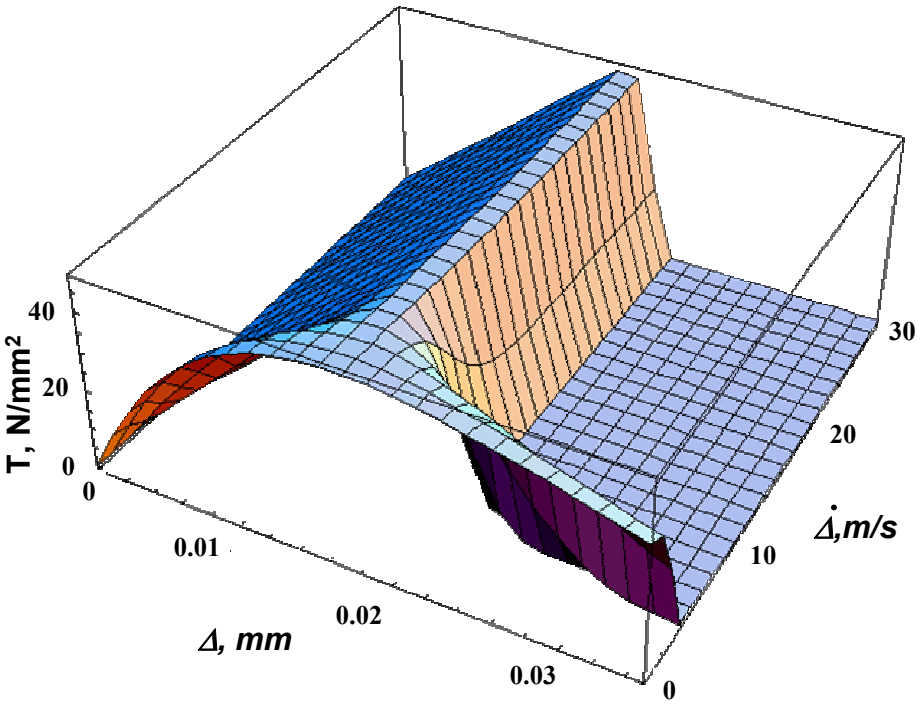


Figure 3.11: Rate Dependent Model II ($\beta = F(\dot{\Delta})$).

To get a further understanding as to how far the value of the brittleness parameter $\beta$ changes, *i.e.*, how brittle the material behaves under high rate of loading, a plot of the CZM law with various values of $\beta$ was generated. The plot is shown in Fig. 3.12. The CZM law with the extreme values of $\beta$ as observed in the rate dependent model **II** are labeled.

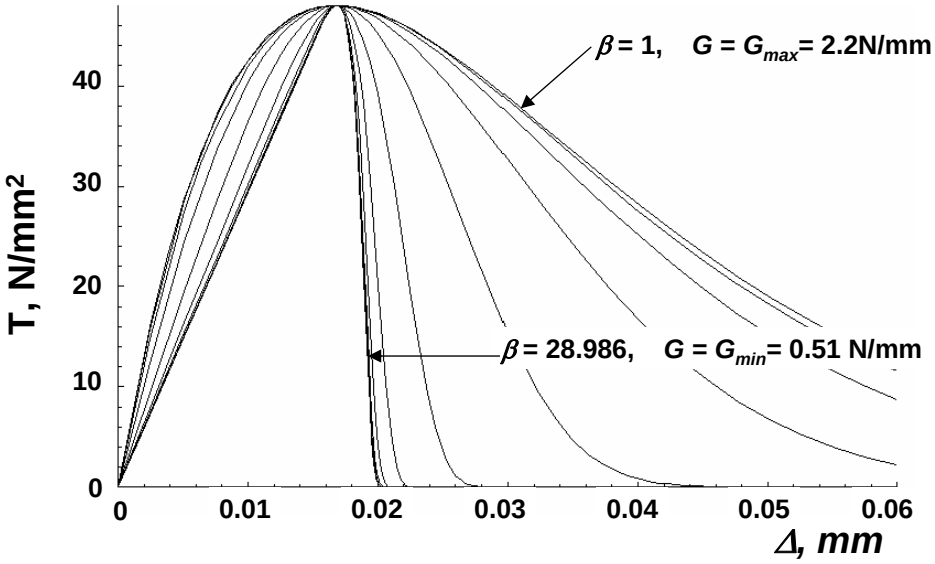


Figure 3.12: Effect on the brittleness parameter in the rate dependent model **II**.

## 3.5 Implementation of Rate Dependent Model I in ABAQUS

The implementation of the rate dependent model is similar to the rate independent model expect for the formulation of the tangent stiffness matrix, which is used to evaluate the stiffness matrix and the internal force vector. For the nonlinear problem formulation, the tangent stiffness matrix can be written in an incremental form as

$$\delta T_i = \frac{\partial T_i}{\partial \Delta_j}\delta\Delta_j + \frac{\partial T_i}{\partial \dot{\Delta}_j}\delta\dot{\Delta}_j = D_{ij}\delta\Delta_j + \dot{D}_{ij}\delta\dot{\Delta}_j \tag{3.5}$$

The tangent stiffness matrix for the rate independent CZM is evaluated by taking the partial derivative of the traction with respect to the opening displacement $\partial T/\partial\Delta = D_{ij}$.

In the case of the rate dependent model, the traction is not only a function of the opening displacement but also the rate of the opening displacement, so the partial derivative of the traction with respect to the rate of opening displacement $\dot{D}_{ij}$ also needs to be evaluated.

Rate Dependent Model I:

For this model proposed here, an analytical form for the partial derivative of traction with respect to the rate of opening displacement is possible. The derivative for the first model is given here:

$$\begin{aligned} \frac{\partial T}{\partial \dot{\Delta}} &= -\left( \frac{A\, T_c\, \xi\, \Delta\, e^{1-\frac{\Delta}{\zeta}-\xi\,\dot{\Delta}}}{\left(B + e^{-\left(\xi\,\dot{\Delta}\right)}\right)^2 \zeta^2} \right) + \frac{A\, T_c\, \xi\, \Delta^2\, e^{1-\frac{\Delta}{\zeta}-\xi\,\dot{\Delta}}}{\left(B + e^{-\left(\xi\,\dot{\Delta}\right)}\right)^2 \zeta^3} \\ \zeta &= \frac{A}{B + e^{-\left(\xi\,\dot{\Delta}\right)}} + G_{min} \end{aligned} \tag{3.6}$$

where $G_{min}$ is the lowest value of the critical strain energy release rate observed in the experiments. This term is added to the partial derivative of the traction with respect to the opening displacement to get the tangent stiffness matrix.

Rate Dependent Model II:

The partial derivative of the traction with respect to the rate of the opening displacement for the second rate dependent model can be derived analytically, but as the equation obtained is too complex, the central difference method was used instead of the analytical

solution. The analytical equation is given here:

$$\begin{aligned}\frac{\partial T}{\partial \dot{\Delta}} &= \frac{1}{\Delta_c}\left[\mathrm{Exp}\left[\frac{1-\Delta/\Delta_c^{\beta}}{\beta}\right]\Delta\, T\left(\frac{-2.5\,A\,\mathrm{Exp}\left[0.5\,\mathrm{V}\right]\left(1-\Delta/\Delta_c^{\beta}\right)}{\left(B+\mathrm{Exp}\left[0.5\,\mathrm{V}\right]\right)G\,\beta^2}\right.\right. \\ &- \left.\left.\frac{2.5A\,\mathrm{Exp}\left[0.5\,\mathrm{V}\right]\Delta/\Delta_c^{\beta}Log\left[\Delta/\Delta_c\right]}{\left(B+\mathrm{Exp}\left[0.5\,\mathrm{V}\right]\right)^2 G\,\beta}\right)\right]\end{aligned} \tag{3.7}$$

$G$ is given by Eq. 3.2 and $\beta$ is defined from the curve fitting shown in Fig. 3.10 as

$$\beta = 1 + \frac{1}{G^5} \tag{3.8}$$

The derivatives are plotted as a function of $\Delta$ and $\dot{\Delta}$ for both rate dependent models for the sake of better understanding.

Both rate dependent models (Section 3.4.1 and 3.4.2) were implemented in ABAQUS® for simulating the DCB test. Rate dependent model **I** converged for the given material properties, however the rate dependent model **II** failed to converge. The time step required for convergence (*i.e.*, for a reasonable residual force vector) was lower than the machine precision. The results for the DCB analyzed using the rate dependent model **I** are presented in the next section.

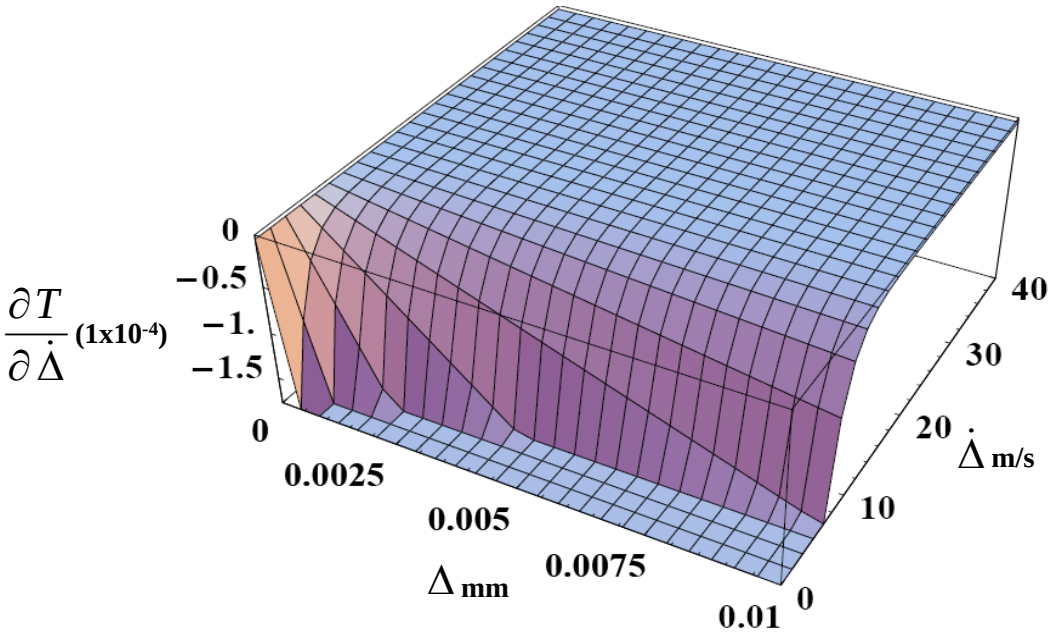


Figure 3.13: Surface plot of the derivative term for rate dependent model **I**.

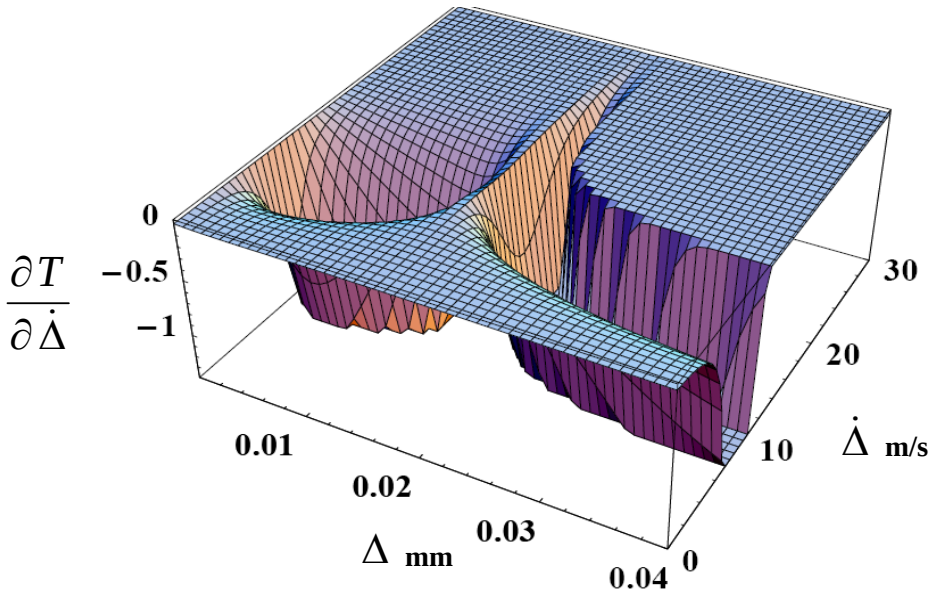


Figure 3.14: Surface plot of the derivative term for rate dependent model **II**.

## 3.6 Results and Discussion

The rate dependent formulation was undertaken with the sole objective of predicting the stick-slip crack growth observed in the quasi-static DCB testing without doing a high fidelity modeling of the adhesive. Let us revisit the problem of the DCB discussed in section 2.5. Again the same properties for the aluminum adherends and the adhesive were used, but instead of modeling the adhesive with ∼80,000 elements, we model the adhesive with just a single layer of interface elements. This reduces the number of elements from ∼80,000 to about 1,000.

Rate dependent model **I** was used to simulate this DCB in ABAQUS®. Reduction in the number of elements didn't reduce the time for the simulation, in fact it almost doubled the time to complete the simulation. The rate dependent model took more iterations to converge for each time step as compared to the rate independent model. The results obtained from this simulation were able to capture the stick-slip crack growth, and the reaction plot along with the one obtained using the high fidelity model discussed in Chapter 2 are shown in Fig. 3.15

Figure 3.15 shows a good agreement between the experimental results and the rate dependent ABAQUS simulations. However, as mentioned before, there was no reduction in the CPU time required to perform the analysis. In fact this time only increased. One marked advantage, however, of using a rate dependent model is that there is no need for creating a highly complex input file. This saves the time required to write FORTRAN

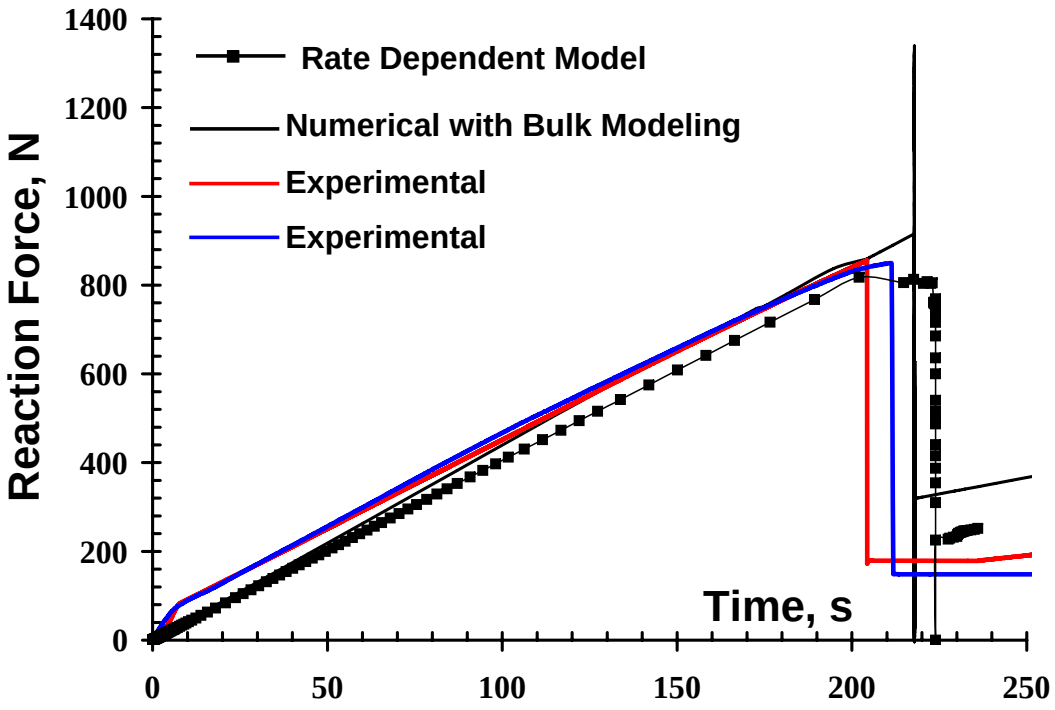


Figure 3.15: Comparison between experimental and numerical results of the tip reaction force for an aluminum DCB.

codes to create the highly refined meshes.

Thus, some of the difficulties associated with the high fidelity modeling mentioned in Section 2.6 have been addressed with the rate dependent model. The difficulty in creating an input file has been handled and also the problem size has been reduced considerably. However, to model the rapid crack growth, the time step required will be extremely small irrespective of the technique used, resulting in large computational times.

# Chapter 4

# Dynamic Fracture Using Explicit Methods

## 4.1 Introduction

Explicit methods have a marked advantage over implicit methods, especially when it comes to analyzing fracture mechanics of structures under dynamic loading. The fact that explicit methods do not require iterations to solve a nonlinear problem also makes the analysis much faster. Time steps in an explicit code are evaluated based on the wave speeds, which in turn depend on the material property and the size of the elements. Quasi-static simulations are therefore not viable using explicit methods. Having established the quasi-static results in an implicit code, the next task is to simulate the same

fracture test specimens discussed in the previous chapters under dynamic loading.

Adhesives have been used to bond joints in automobiles for quite some time now. The automobile industry, for the most part, uses LS-DYNA to simulate the car crash and evaluate the use of composite materials in automobiles. Keeping this in mind, we undertake the task of incorporating the CZM law in LS-DYNA to help facilitate the study of the behavior of bonded joints in a car crash. Unlike ABAQUS, LS-DYNA does not facilitate the user to define elements, so interface elements required to simulate dynamic fracture cannot be incorporated into LS-DYNA directly. The only way to incorporate the CZM law is through a user defined material (UMAT) option, which LS-DYNA allows. The limitations of the software and the process of incorporating the CZM law through the UMAT will be discussed in detail in the subsequent sections. Incorporation of the rate dependent CZM law will be discussed in detail and some dynamic test results will be compared with experimental results in the last section.

## 4.2 User Defined Material (UMAT)

LS-DYNA has the capability that allows the user to define the constitutive relation for a material. A FORTRAN code needs to be written and incorporated with the LS-DYNA to achieve this. The main program of LS-DYNA passes the strain vector at a given point to the subroutine defined by the user and the main program requires the stress vector as an output from the subroutine. This in a gist is the flow of information that takes place

from the main program to the subroutine.

The CZM law incorporated in LS-DYNA through the material definition will be used in conjunction with the standard library elements. Since the standard library elements cannot be specified to have a zero thickness, the thickness of the elements used to model the adhesive is kept equal to the thickness of the adhesive used in the specimen preparation. This acts as the reference thickness, and the opening displacement will be the additional displacement that the element undergoes as the load is applied. For Mode I and Mode II this is shown with a plane strain four-noded element in Fig. 4.1. Adhesive thickness is denoted by '**h**' and the displacements in the deformed configurations, denoted by $\Delta h$ and $\Delta\phi$, are taken to be the opening and sliding displacements, respectively. The thickness of the adhesive will also be taken into account while calculating the shear stress the element undergoes for Mode II and Mode III.

CZM is implemented by having a standard library element with material properties such that it allows the element representing the adhesive to deform only in the three fracture modes. The reference axis can be chosen arbitrarily based on one's preference. For this study the 'Y' direction is taken to be the opening direction. Figure 4.2 shows the three modes of fracture along with a standard brick element. Having established the opening direction for Mode I, the other directions follow from the basics of Linear Elastic Fracture Mechanics (LEFM).

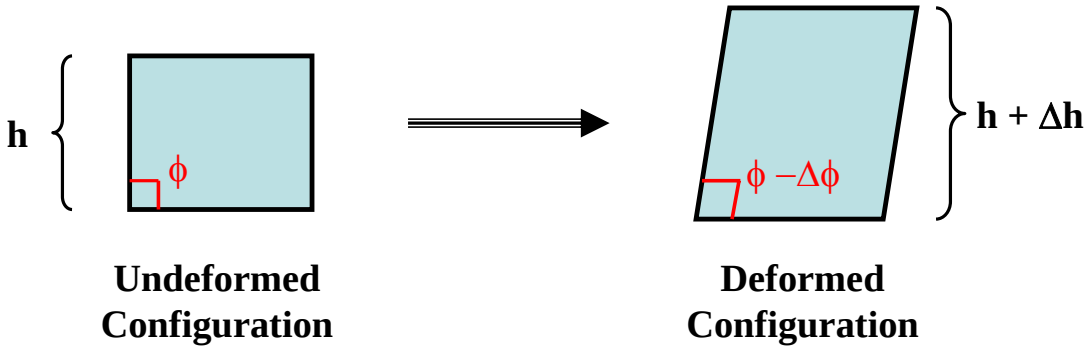


Figure 4.1: Calculation of the opening displacements in a plane strain element.

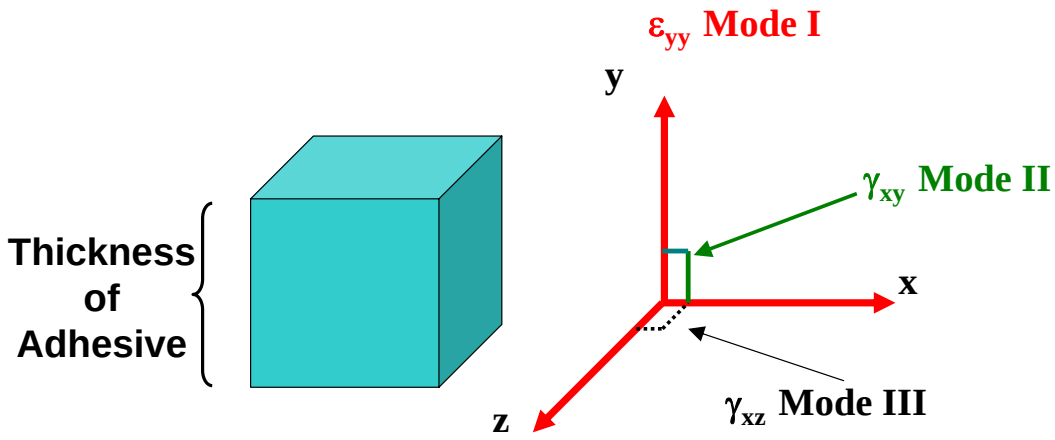


Figure 4.2: Reference orientation for the three fracture modes in a standard brick element.

## 4.3 Formulation

The main program of LS-DYNA requires that the UMAT subroutine evaluates and outputs the stress vector based on the strain vector provided to the UMAT subroutine by the main program. Based on the orientation of the fracture modes shown in Fig. 4.2 and the traction-displacement law, Eq. 2.14, the stress vector can be defined as:

$$\begin{Bmatrix} \sigma_{xx} \\ \sigma_{yy} \\ \sigma_{zz} \\ \tau_{xy} \\ \tau_{yz} \\ \tau_{zx} \end{Bmatrix} = \begin{Bmatrix} 0 \\ T^1_{\max}\left\langle \bar{\Delta}_1 \right\rangle Exp\left(\frac{2-\mu^\beta/\tilde{d}-\tilde{d}}{\beta}\right) - \left\langle \bar{\Delta}_1 \right\rangle Exp\left(\frac{1+\kappa\left|\bar{\Delta}_1\right|^\beta}{\beta}\right) \\ 0 \\ T^2_{\max}\bar{\Delta}_2 Exp\left(\frac{2-\mu^\beta/\tilde{d}-\tilde{d}}{\beta}\right) \\ 0 \\ T^3_{\max}\bar{\Delta}_3 Exp\left(\frac{2-\mu^\beta/\tilde{d}-\tilde{d}}{\beta}\right) \end{Bmatrix} \tag{4.1}$$

The displacements are calculated from the strain vector that comes as information after every time step from the main program. LS-DYNA is programmed based on the updated Lagrangian formulation (Eulerian as per the manual, LS-DYNA (2003)) so the strains at every step are calculated taking the deformed state of the element at the previous time step as the reference state. This has to be taken into account while evaluating the opening displacements in the UMAT subroutine.

Assumptions made in this formulation are that the stresses $\sigma_{xx}, \sigma_{zz}$ and $\tau_{\mathrm{yz}}$, which do not represent any failure mode, are always going to be zero. The strains developed in these

directions will be neglected. The interpenetration in this case will be implemented when the stress $\sigma_{yy}$ becomes compressive, in other words, when the change in the thickness $\Delta h$ becomes negative and the element tries to reduce the originally specified thickness. The same laws for the mixed mode failure criteria as defined in Eq. 2.13 are used in this formulation.

## 4.4 A Beginner's Guide to Writing UMAT in LS-DYNA

The objective of this section is to have a document describing in detail the procedure for writing the User defined Materials subroutines to incorporate in LS-DYNA. Need for this section is justified from the viewpoint that the manuals of LS-DYNA have almost no instructions regarding this. The amount of time and effort put into writing this subroutine and the experience gained could act as guidelines for further ventures. Some of the things outlined here may seem redundant to some readers, but will be useful for anyone who is just starting to use User defined options in LS-DYNA.

The first thing that one needs to do while trying to write the UMAT for LS-DYNA is to obtain a half compiled FORTRAN workspace from LS-DYNA. The standard software distributed by LS-DYNA is not capable of allowing User defined Material subroutines. One has to be careful to have exactly the same compiler as specified by LS-DYNA. Since

Table 4.1: Additional arguements in LS-DYNA.

| Argument | Description |
|---|---|
| i | User specified element number |
| ixs | Node numbers used by the program internally |
| x($\bar{x}$,ix1(nlq)) | A two dimensional array containing the global nodal coordinates |
| ix1(nlq),...,ix8(nlq) | Node numbers specified by user for the nlq$^{th}$ element |

the code which LS-DYNA will be giving is a half compiled code, the code needs exactly the same version of FORTRAN to complete the compilation and create an executable file. This executable file can than be used with the LS-DYNA manager.

Having established the setup which will create the executable file, we now move onto the the details of the subroutine. Primarily, we shall consider the information that is being passed into and out of the subroutine. The subroutine has the following arguments:

**subroutine umat41 (cm,eps,sig,hisv,dt1,capa,etype,time,temp,i,ixs,x,k,j)**

The program gives only part of the argument up till temp. The rest of the arguments are for information regarding the element numbers and the global position of the nodes. The additional information was obtained by going through the main program and mostly by trial and error. The additional arguments that are being used will be listed with the details, whereas the standard arguments can be referred in the LS-DYNA manual. Some arguments are added by using a common card in FORTRAN as follows:

**common/aux33loc/ix1(nlq),ix2(nlq),...,ix8(nlq),mxt(nlq)**

Most of these arguments mentioned in Table 4.1 are needed to evaluate the crack lengths. Since LS-DYNA is based on the updated Lagrangian formulation, one has to be careful while evaluating the strains. For this case, history variables were used to store the dimensions of the element at each time step. At the next time step these stored values were used to evaluate the change in lengths as compared to the original undeformed configuration.

The calculation of crack length was the more complicated part of this implementation, since any information regarding the element or nodes was not being passed to the UMAT subroutine. Once this was established, the crack length was determined on the same criteria as for the interface element, *i.e.*, the tractions should become negligible ($\leqslant 1 \times 10^{-6}$). Since when the element is being loaded the traction could be less than the specified value of $1 \times 10^{-6}$ for a traction free surface, the damage parameter was also noted in the history variable in addition to the tractions. Both the damage and the tractions were monitored before establishing the crack tip.

The tractions in the interface element could be monitored at the Gauss points so the crack lengths could jump from one Gauss point to the next. However, in the material model implementation of the CZM, the opening displacements are monitored at the nodes so the crack length would have to jump at least one element length. A compromise has to be achieved between the accuracy of the crack length and the value of the time increments. A smaller element size will give accurate crack information but will reduce the time step since the time step in LS-DYNA, an explicit code, is determined by the following

equation:

$$\Delta t_e = \frac{L_s}{c} \tag{4.2}$$

where $c$ is the wave speed of the material given by

$$c = \sqrt{\frac{E}{\rho(1-\nu^2)}} \tag{4.3}$$

and $L_s$ is the representative length of the element. For a rectangular element, this length is given by

$$L_s = \frac{A_s}{\max(L_1, L_2, L_3, L_4)} \tag{4.4}$$

For the simulation in these studies, the elements have one dimension equal to the thickness of the adhesive, while the other edges are kept at 0.5mm.

## 4.5 Rate Dependent Model

The rate dependent model **II** discussed in section 3.4.2 is implemented in the UMAT for LS-DYNA®. Since LS-DYNA® is an explicit code, the question of the number of iterations to establish equilibrium at each time step does not arise. So the code which did not converge in an implicit code is being implemented in an explicit code. For the implementation of the rate dependent model, the rate of the opening displacement is needed. The opening displacements are being established from the strain information that is being passed to the subroutine. This information is stored in the history variable

for the last time step and a backward difference is performed to estimate the rate of the opening displacement.

Since the rate dependent model is established for Mode I, only the Mode I opening rate is monitored. The rate dependent model **II** used here assumes that $\Delta_c$ is constant and $\beta$ is being varied to achieve a change in the critical strain energy release rate. The variation of $\beta$ has been shown in Fig. 3.10. Having established the CZM law along with the rate dependent model in LS-DYNA® through a user defined material model (UMAT), the next step is to validate the implementation with available experimental results.

## 4.6 Mode I Results

To validate the CZM implemented in an explicit code through a material model, we take the results of an aluminum DCB under a falling wedge test. The test was conducted at the ESM department at Virginia Tech under the guidance of Dr. David Dillard. The specimen along with the bearings and the drop tower setup are shown in Fig. 4.3. The test is set up in such a manner that the falling wedge does not come in contact with the beams at all. The wedge falls on the two sets of bearings that are protruding from the edges of the beams. The details of the drop tower and the test procedure are well documented by Simón (2004).

Under dynamic testing conditions, it is difficult to measure the reaction forces, since they are very oscillatory ( Blackman *et al.* (1995)). The other information that can be

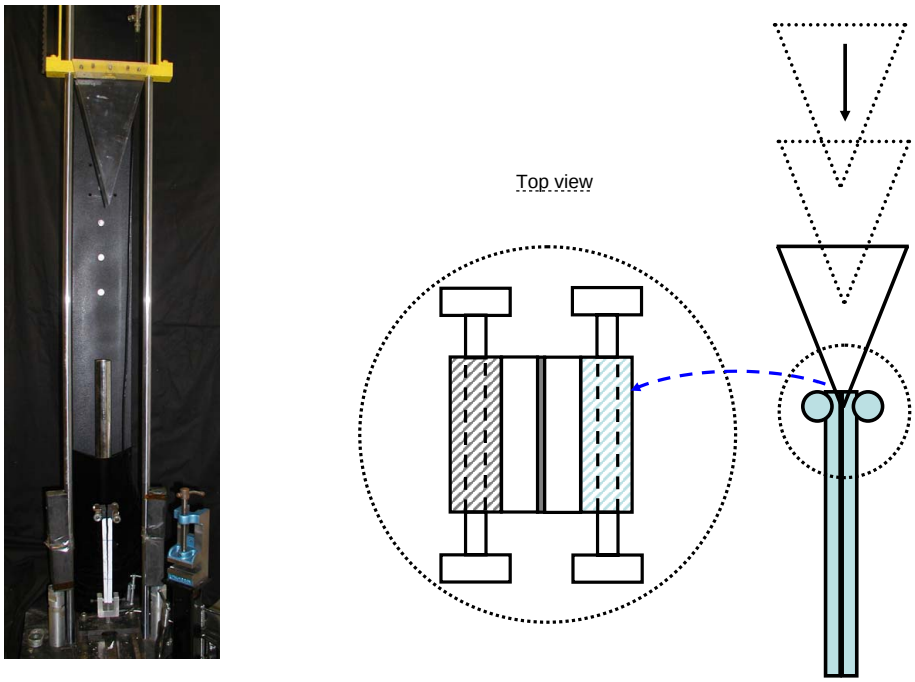


Figure 4.3: DCB dynamic testing using a drop tower in Adhesion Science Laboratory, ESM.

extracted from the experimental data is the crack length as a function of time. This is the information that is being collected from the drop tower experiment and compared to the crack length obtained numerically. The crack length information from the drop tower test is difficult to measure with the naked eye, so a high-speed camera is used to record the complete experiment. Tip displacements can be found from the images based on the pixel resolution used. Crack lengths are found by solving the third-order beam theory equations for the known tip displacements. The crack lengths are determined in a MATHEMATICA® code by using the built-in root finding algorithms.

### 4.6.1 Aluminum DCB

The specimens tested under quasi-static conditions are used here in the drop tower test to study the characteristics of the adhesive under dynamic loading. End blocks with the bearings were fixed to the DCB specimens and were cracked to about 55mm. The material properties for the aluminum are given in Table 4.2.

Table 4.2: Mechanical properties for aluminum for dynamic testing.

| $E_{11}$ | $\nu$ | $\rho$ |
|---|---|---|
| 69 GPa | 0.3 | 2700 $kg/m^3$ |

The adhesive properties used in this simulation are the same as the ones used for the quasi-static testing and are given in Table 4.3. An opening velocity of 2.2 m/s was

Table 4.3: Material properties for the SIA adhesive as defined in the UMAT.

| $T_1^c = T_c^2$ | $G_{I_c}$ | $\beta$ | $K_a$ | $\rho$ |
|---|---|---|---|---|
| 40 MPa | 2.2 N/mm | 2 | $10^6$N/mm$^3$ | 1000 $kg/m^3$ |

induced at the tips of the beams due to the falling wedge. The calculations for these were made based on the angle of the wedge, the falling mass on top of the drop tower. The main assumption here is that the wedge is in constant contact with the bearings. Details of these calculations can be found in Josh Simón's Thesis ( Simón (2004)).

A two-dimensional plane strain model was used for numerical analysis of the aluminum DCB. The adhesive was modeled with plane strain elements too, but the material was user defined. Single elements through the thickness were used to model the adhesive, with the height of the element being kept equal to the thickness of the adhesive. The length of the element was kept as 0.5mm. The geometry of the specimen was the same as that mentioned in Section 2.3.

Figure 4.4 shows the comparison of the crack lengths for two experiments and a numerical simulation. The simulation was run using a rate independent CZM law. The graph shows that the crack lengths predicted from the numerical analysis have a good agreement with the experimental results. On careful observation it might be noticed that at some place the crack length deduced from the experiments starts to reduce marginally with increasing time. This is physically not possible since the material once cracked cannot heal again. The error is induced from the numerical root finding of the third-order beam theory equation used to get the crack length from the captured digital image.

### 4.6.2 Composite DCB

Having established the CZM law for the adhesive through the UMAT option in LS-DYNA, we proceed to analyze joints with composite materials. The additional failure modes for composite materials are the failure of the composite material and the delamination between the plies. The failure of the composite material is considered in this simulation

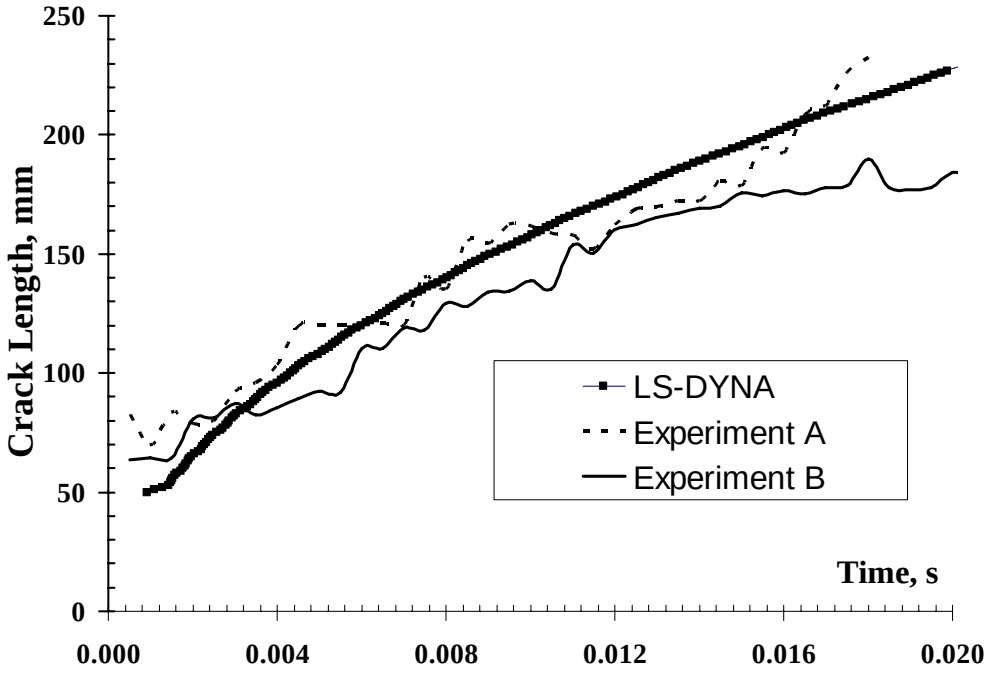


Figure 4.4: Crack length comparison for aluminum DCB in a drop tower test.

but the delamination between the plies is ignored. For the degradation of the composite material, the Tsai and Wu model ( Tsai and Wu (1971)), which takes into account the fiber failure as well as the matrix failure, is considered. The material model for the degradation of the composite material is already incorporated in LS-DYNA through the library Material type 55 (*MAT_054-55).

The geometry of the composite DCB specimen is the same as that of the aluminum DCB except that the thickness of the adherend is 2.34mm. Here the composite material is a woven composite made up of an 11 ply symmetric lay up. The material properties for the 11 ply composite material is given in Table 4.4. The same setup for the drop tower was used as for the aluminum DCB. However, when the digital images were processed

Table 4.4: Material properties for composite adherends (11-ply symmetric).

| $E_{11}$ | $E_{22} = E_{33}$ | $\nu_{21} = \nu_{31}$ | $\nu_{32}$ | $G_{12}$ | $G_{13} = G_{23}$ |
|---|---|---|---|---|---|
| 45 GPa | 40 GPa | 0.24 | 0.34 | 18 GPa | 14 GPa |

to deduce the crack information, the trend shown by the crack growth in the composite DCB was altogether different from the crack growth pattern in the aluminum DCB. The crack growth information is shown in Fig. 4.5.

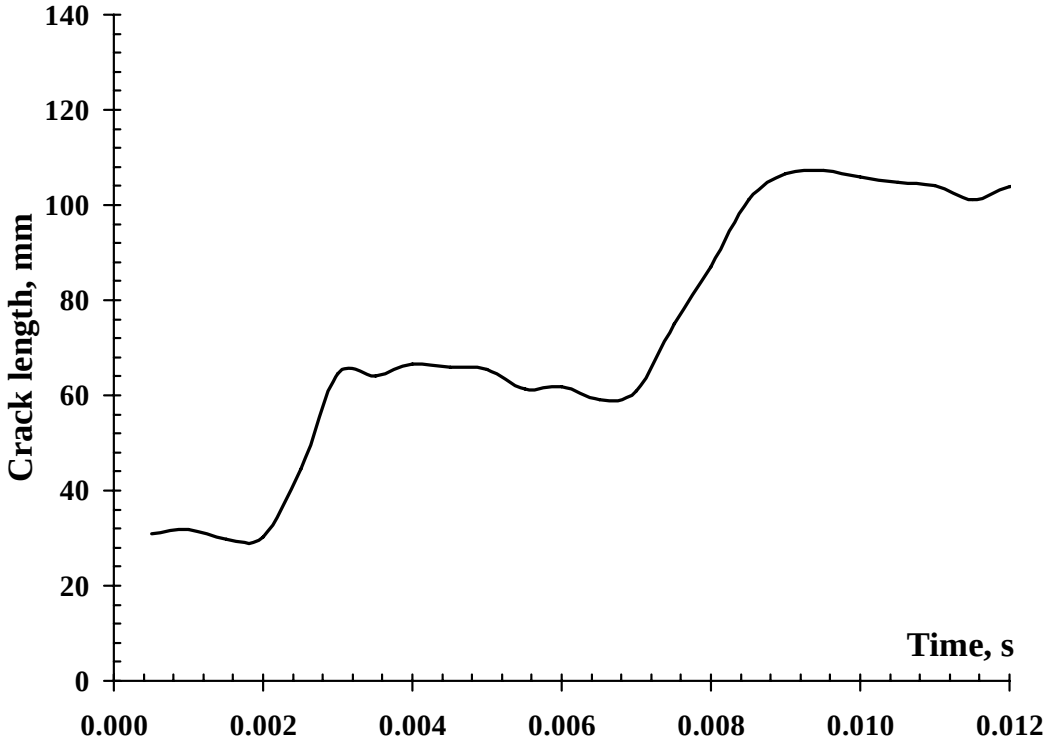


Figure 4.5: Crack length for a composite DCB test in the drop tower.

As can be seen from Fig. 4.5, the crack growth exhibits some kind of stick-slip behavior. The flat plateau observed in the graph indicates that for a certain period of time the crack is arrested. Also, the reduction in crack growth observed once again contributes to

the numerical error in obtaining the crack lengths from the digital images.

The LS-DYNA® simulations were carried out a little differently as compared to the aluminum DCB. Plane strain elements can not be used to model composite beams, so shell elements were used to model the composite beams and the adhesive was modeled using 3D brick elements. Figure 4.6 shows snapshots at different times during the simulation of the numerical model. The crack was measured at the center of the width of the composite DCB. A crack growth pattern similar to the one for the aluminum DCB was obtained. When the rate dependent effects were considered, it exhibited some type of stick-slip behavior but nothing as significant as what was observed in the experiments (Fig. 4.5).

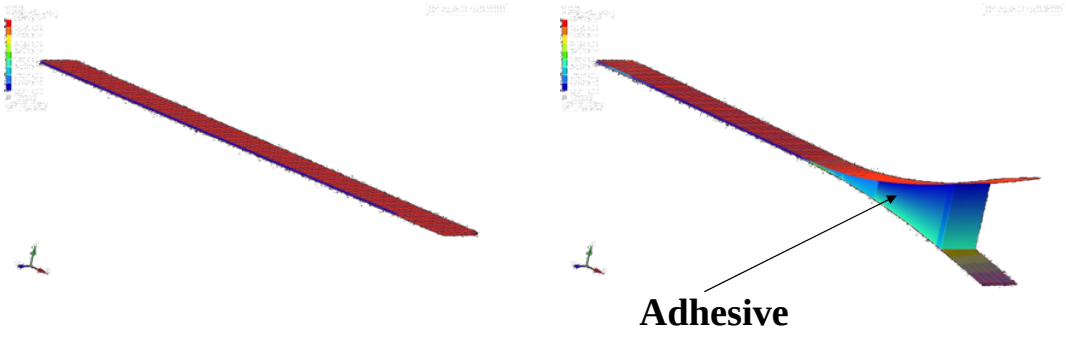


Figure 4.6: Snapshots of the composite DCB simulation a) t = 0s b) t = 0.01s.

This stick-slip behavior led us to look closely at each of our assumptions that were made at every step in the experiments, as well as the numerical analysis. One of the major assumptions made in the drop tower experiment is that the wedge stayed in continuous contact with the bearing, and the velocity imparted to the bearings by the falling wedge was constant in time. To verify this assumption, the tip displacements of the adherends

were plotted with respect to time from the digital images that were taken of the specimen at 2,000 frames/sec. The tip displacement is shown in Fig. 4.7. As can be seen in Fig. 4.7, the tip displacement does not vary linearly with time, indicating that the velocity is not constant. However, one can argue, looking at the graph in Fig. 4.7, that it is almost linear. A linear regression fit was done to check this. The fit along with the original curve is shown in Fig. 4.8.

The parameter, $R^2$, which is known as the measure of the goodness-of-the-fit, is very close to unity (the exact fit). However, the good fit does not necessarily imply that the assumptions made, keeping in mind the physics of the problem, are indeed valid. If the wedge loses contact with the bearing for very small period of times, the effect may not be noticed in the tip displacement since it may be too fast for the camera to capture, but it could change the way the crack grows.

To be certain about the effects of this non-linear displacement profile exhibited by the arms of the composite adherends, a simulation in LS-DYNA® was done where instead of prescribing a constant velocity at the tips of the adherends, the displacement profile measured from the camera was prescribed as the boundary condition. Surprisingly the crack growth pattern that this simulation gave us was different from the one obtained using the constant velocity assumption. This numerical simulation exhibited the stick-slip behavior as was observed in the experiments. This is a very important observation, as almost every study in the literature, to the best of our knowledge, that has used the drop tower has assumed that the velocity imparted by the falling wedge to the bearing

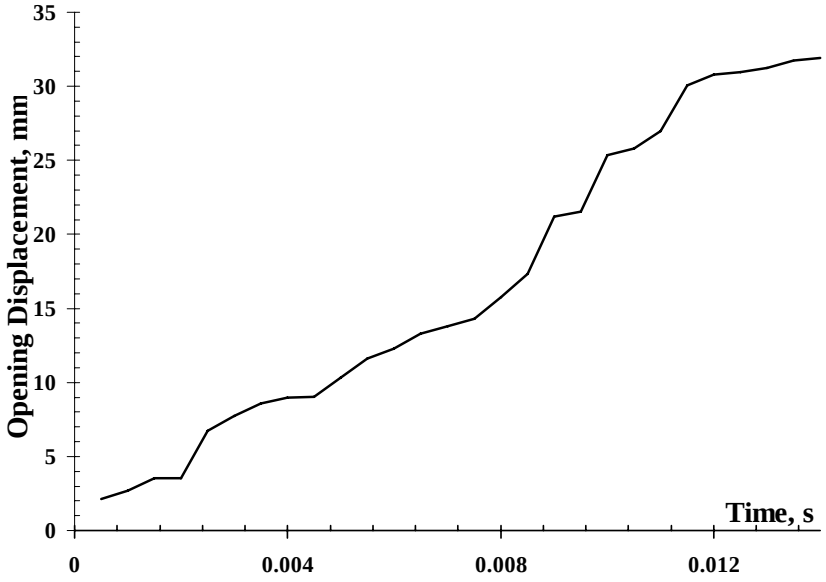


Figure 4.7: Tip displacement observed from test.

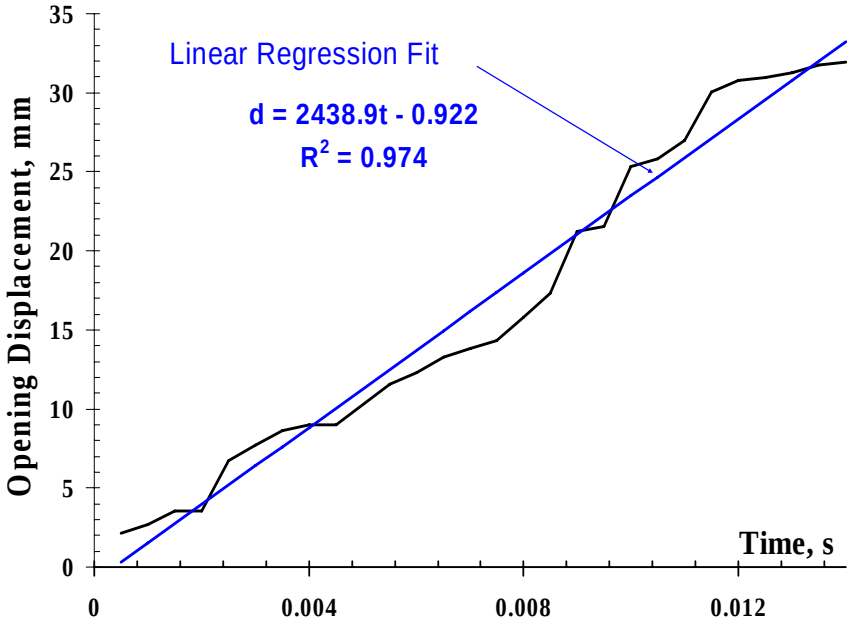


Figure 4.8: Tip displacement observed from test and a linear regression fit.

is constant. Here it has been proven that for the smallest period of time when the bearing loses contact with the wedge, the crack growth pattern will change. There is the possibility that this will also depend somewhat on the compliance of the adherends. If the adherends are too compliant, *i.e.*, they are too thin, there is a high possibility that the bearings might lose contact with the wedge. A study of a composite DCB with thicker adherends was planned to draw a more concrete conclusion. Unfortunately this was the time when the high speed digital camera in the ESM department broke down.

The crack growth pattern obtained from the simulation by prescribing the displacement observed in the experiments at the tips is shown in Fig. 4.9. One can observe that

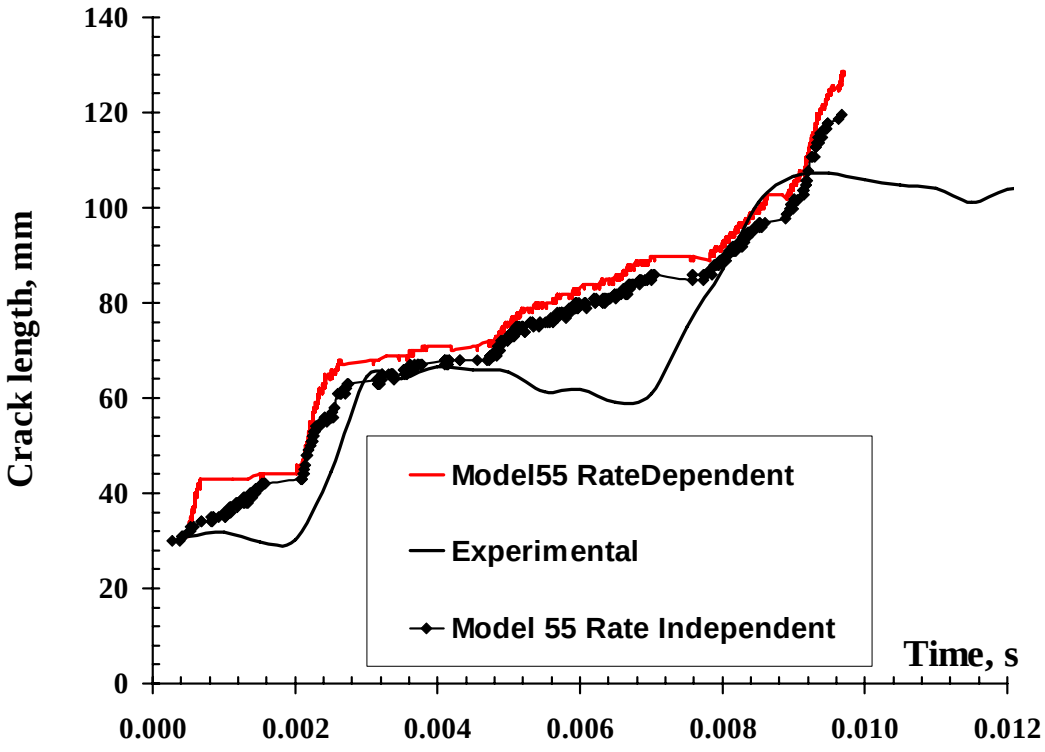


Figure 4.9: Crack length comparison for composite DCB.

the rate dependent model introduces some amount of stick-slip, especially initially, but the predominant effect is due to the application of the experimentally measured tip displacement profile.

## 4.7 Mode II Simulations

Joints in structures often fail in mixed mode conditions rather than in any single predominant mode. To predict the failure of practical joints, it is necessary to investigate the other modes of failure as well. Having established Mode I under quasi-static and dynamic conditions, we proceed to investigate the Mode II characteristics of the SIA adhesive under dynamic conditions. The configuration chosen for Mode II testing is the End Loaded Split (ELS) and a schematic is shown in Fig. 4.10

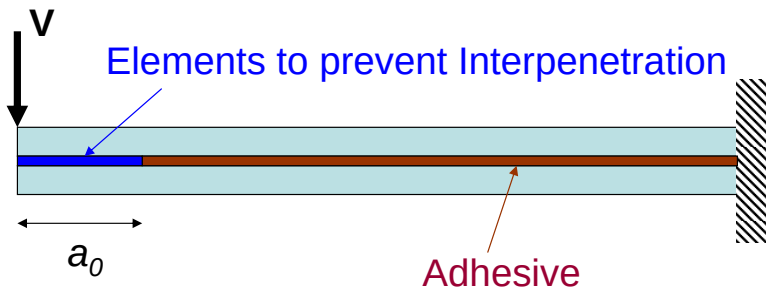


Figure 4.10: The ELS configuration for Mode II testing.

The configuration shows that only one adherend tip is being imparted a certain velocity. This will cause the adherends in the precracked zone to come in contact with each other. So in the finite element simulations the precrack was modeled with special con-

tact elements, which provided a high resistive stiffness to interpenetration, but offered no resistance to the crack growth. The ELS was tested in the drop tower. Instead of the falling wedge, a tip was attached and the beam was mounted parallel to the ground as shown in Fig. 4.11. The drop velocity of the tip was calculated to be 2m/s. An alu-

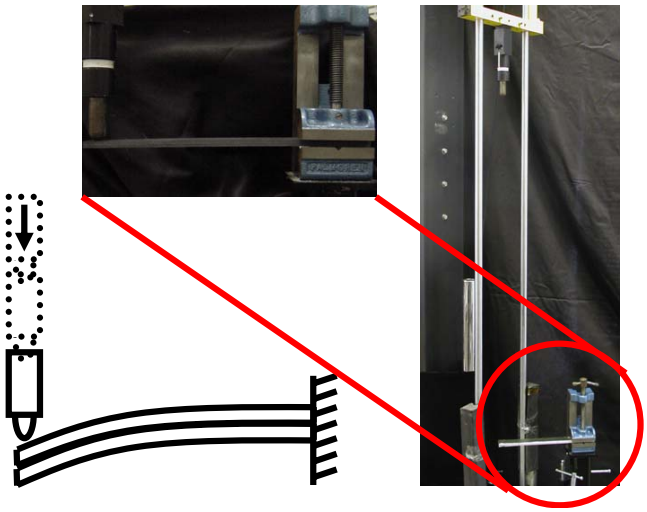

Figure 4.11: ELS specimen in a drop tower.

minum ELS specimen was prepared in a manner similar to that of the DCB. A pre-crack of 55 mm was kept for the ELS specimen. The critical strain energy release rate was the only information that could be extracted from the experiment. A value of 4 N/mm was deduced from the drop tower data following the procedure given by Blackman *et al.* (1996). All that could be noted from the experimental video was that the crack was growing extremely fast. This can be seen in a series of snapshots shown in Fig. 4.12. The crack growth can be observed from these images based on the fact that at the crack tip, the slope of the specimen will change. As the crack tip grows through the specimen, the

location of this discontinuity will also change.

The ELS was simulated in LS-DYNA with the same geometry and mesh size as for the aluminum DCB. Only the elements used to avoid interpenetration were added. The loading conditions were changed as per the schematic shown in Fig. 4.10. Since the crack length information was not available from the experiments, a quantitative comparison is not possible. However, a qualitative comparison for the crack growth will be done using the images from the numerical simulation.

Snapshots of the numerical simulation similar to the experimental simulation shown in Fig. 4.12 are shown here for a qualitative comparison in Fig. 4.13. Looking at the images shown in Figs. 4.12 and 4.13, it can be said that the crack growth is similar in both the sets of images. To get an idea of how fast the crack grew, the crack information obtained from the numerical simulation is plotted as a function of time. Figure 4.14 shows the plot of crack length as a function of time and, as can be seen, the crack length increases almost instantaneously. For clarity, regarding the CZM model used, we reiterate that the rate dependent model was developed for Mode I only, so the ELS simulation is done using a rate independent CZM.

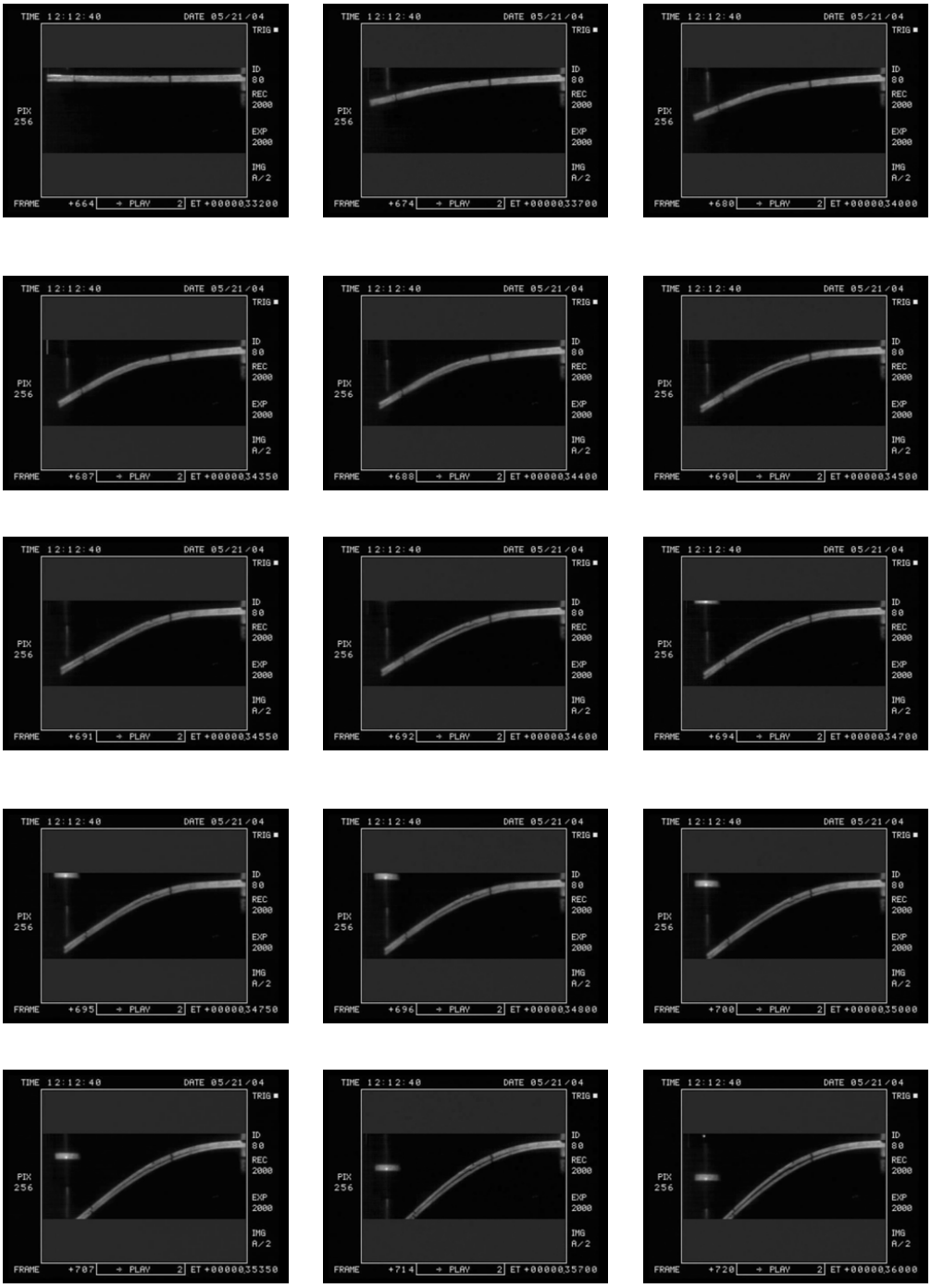


Figure 4.12: Snapshots of the ELS in a drop tower.

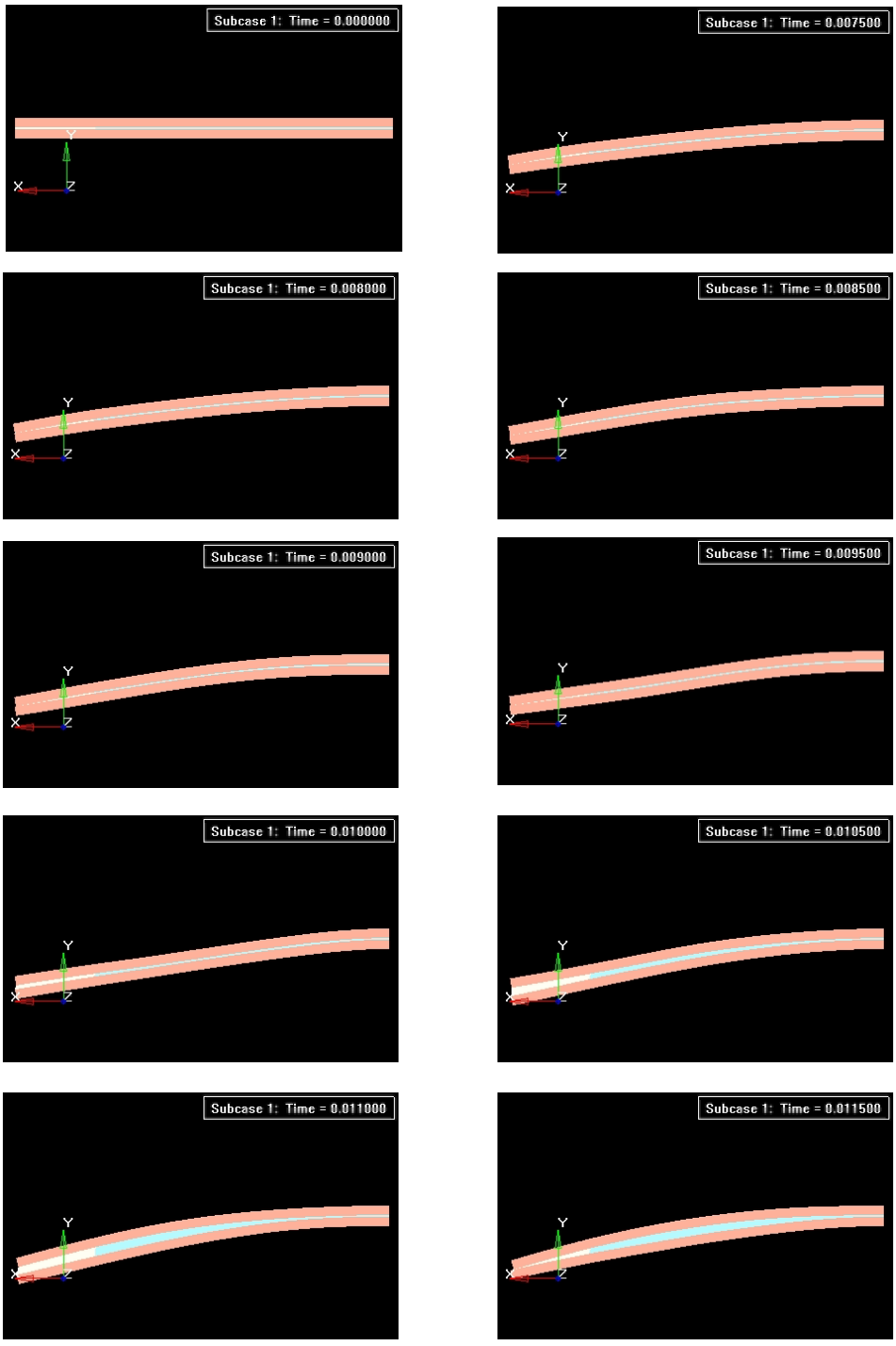


Figure 4.13: Snapshots of the ELS simulation in LS-DYNA.

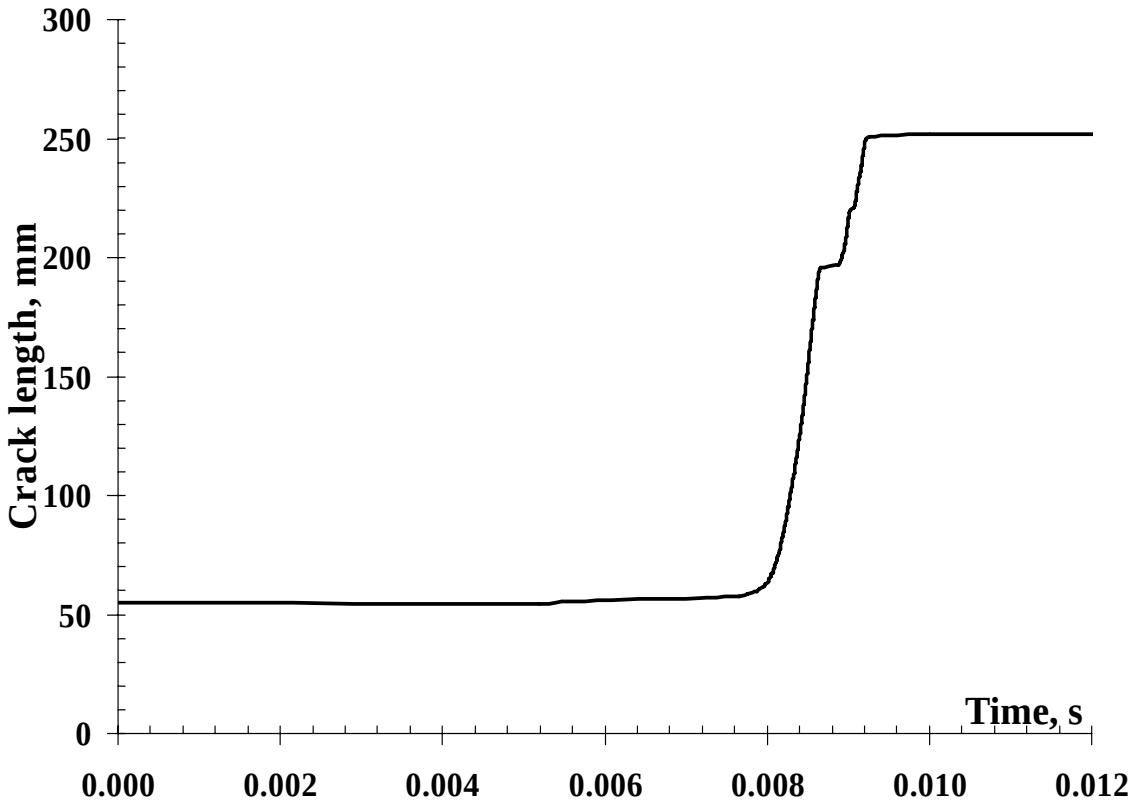


Figure 4.14: Crack growth history from the ELS simulation using LS-DYNA and a rate independent CZM law.

# Chapter 5

# Modeling of an Unbonded/Bonded Square Composite Tube

## 5.1 Introduction

Collapsible impact energy absorbers made of fibre reinforced composite materials are structural elements used in a broad range of automotive and aerospace applications, since they provide significant functional and economic benefits such as enhanced strength and durability, weight reduction and lower fuel consumption. Moreover, they have been found to ensure enhanced levels of structural vehicle crashworthiness, being capable of collapsing progressively in a controlled manner that ensures high crash energy absorption in the event of a sudden collision. In contrast to the response of metals and polymers,

progressive crushing of composite collapsible energy absorbers is dominated by extensive micro-fractures instead of plastic deformation. Among the various types of composite structures and materials that have been tried by researchers worldwide aiming to achieve an improved level of crashworthiness, fibre reinforced plastics (FRP) have proven to be exceptionally efficient crash energy absorbing components featured by excellent stiffness to weight ratios.

The most widely used method of design of composite collapsible energy absorbers is by experimental testing in order to quantify mechanical properties and behavior of structures, since the complex failure mechanisms that characterize the overall crushing response of composite structures, such as transverse shear, inter- and intra-laminar cracking, laminate splaying, or local wall buckling, are difficult to predict by analytical methods. However, the high cost of experimental work makes the design by means of numerical methods, especially finite element simulations, very attractive, even though this requires fine-tuning of the analytical models and approximate constitutive laws in order to satisfactorily predict the complex behavior of the composite materials and the propagation of structural failure.

There has been a considerable amount of research on circular tubes of isotropic material (namely aluminum) and composite materials. Based on the axisymmetric mode of deformation, analytical solutions have also been proposed. An extensive study along with some numerical and experimental results have been complied by Al Galib and Limam (2004) for circular aluminum tubes under static and dynamic axial crushing. The circular

aluminum tubes will be considered in this study for the purpose of verification. One of the tubes tested in the paper cited above will be simulated in LS-DYNA and the failure modes and the reaction forces will be compared.

## 5.2 Square Tubes

Recently square tubes made up of composite material have received more attention in the automotive industry. Square tubes have more complex failure modes as compared to circular tubes, and the failure of the composite material adds to the complexity of the analysis. Failure of the square tubes can be classified as given by Mamalis *et al.* (2005) into three basic failure modes:

1. Mode I: Progressive end-crushing collapse
2. Mode II: Local tube wall buckling collapse
3. Mode III: Mid-length collapse

Experimental images of the three failure modes shown by Mamalis *et al.* (2005) are reproduced in Fig. 5.1. The research done by Mamalis *et al.* (2005) shows that LS-DYNA is able to capture the three modes of failure for square tubes made up of carbon fibre reinforced plastics (CFRP). LS-DYNA predicted the main crushing characteristic *i.e.*, the peak compressive load and the absorbed crash energy, very well for all the failure

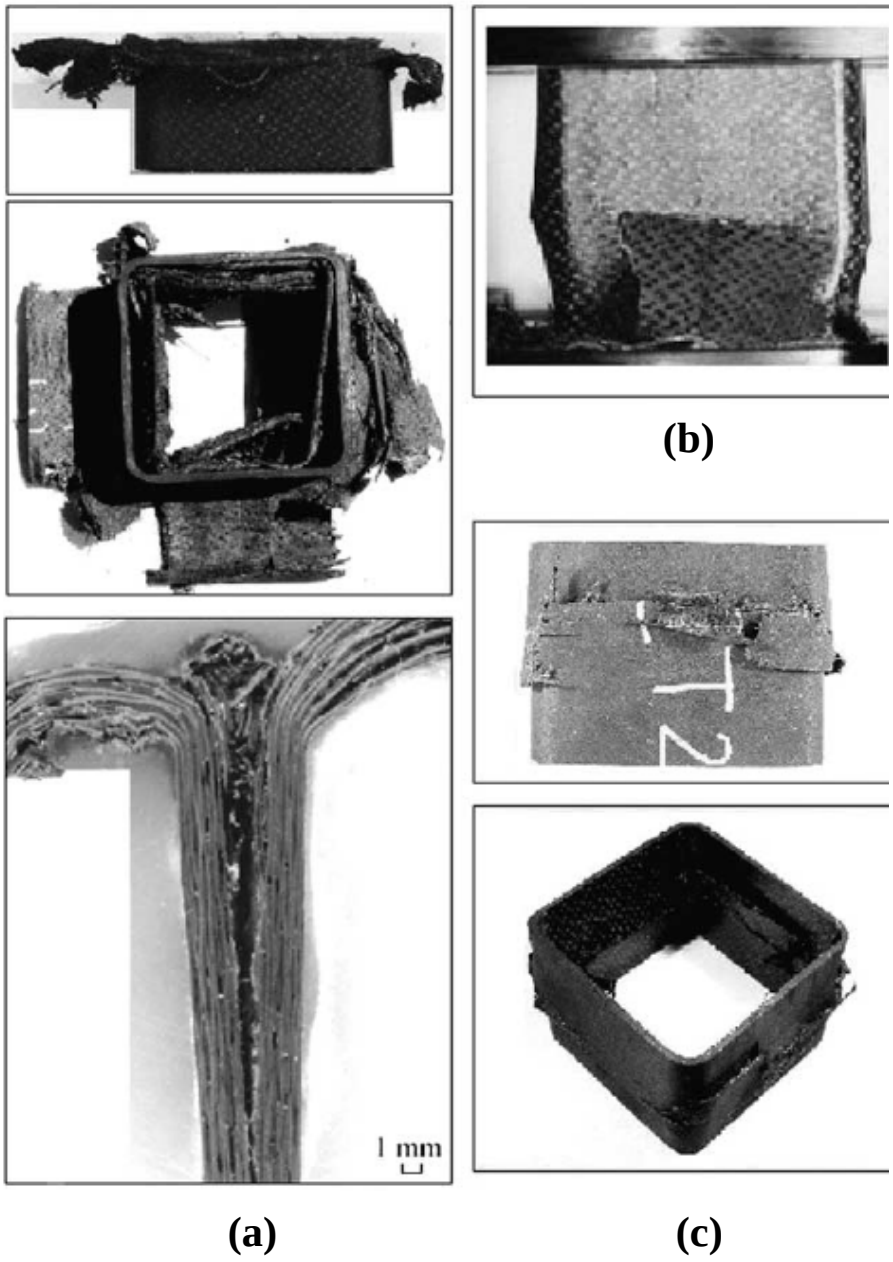


Figure 5.1: Deformed specimens corresponding to collapse Modes I-III: (a) Mode I; (b) Mode II; (c) Mode III.

modes. Also, another important observation of this study was that the tubes failed only in Mode I under static loading.

The experiments carried out by ORNL on the square composite tubes considered in this study showed that the tubes failed by progressive end-crushing under dynamic loading conditions, which is contrary to what is reported by Mamalis *et al.* (2005), Hull (1991) and Farley and Jones (1992). However, the failure was not a pure Mode I failure as shown in Fig. 5.1. The main difference was that under the progressive end-crushing observed in the experiments at ORNL, the material at the progressive end shattered and was broken in small pieces as opposed to flaps being formed as shown in Fig. 5.1. The deformed specimen of the tube considered in this study is shown in Fig. 5.2. Most of the simulations in the study by Mamalis *et al.* (2005) were carried out under a quasi-static loading and only the failure under Mode III was studied under the dynamic loading. Even though this is not the mode in which the tubes in this study failed, we shall be comparing our LS-DYNA simulations to the ones given by Mamalis *et al.* (2005) to achieve a certain confidence in our implementation skills in LS-DYNA.

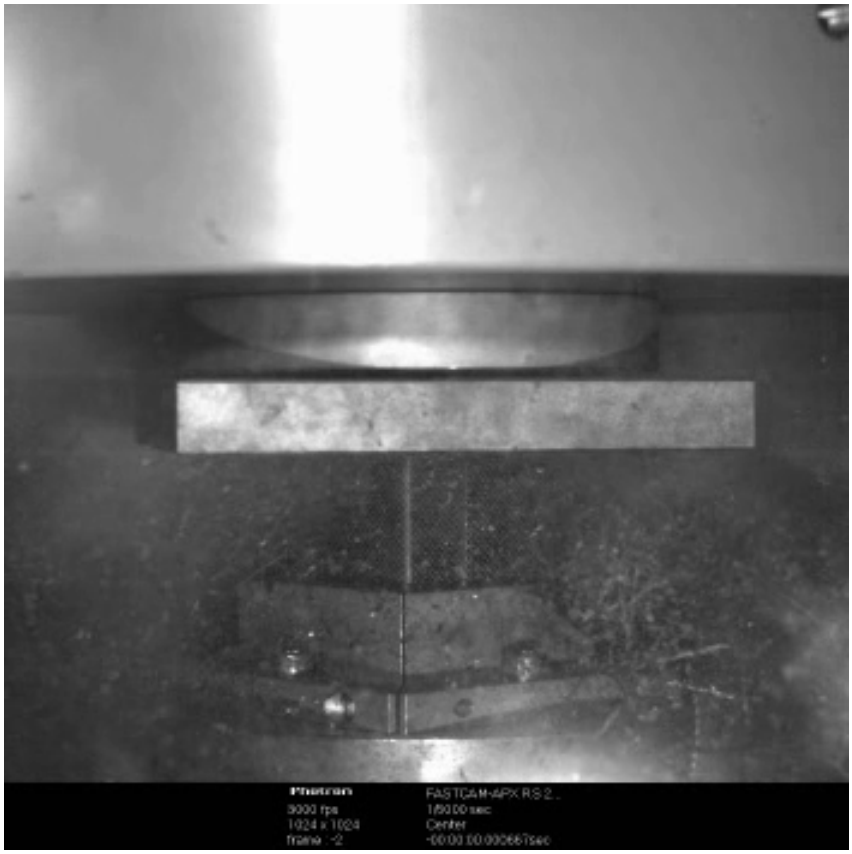


Figure 5.2: Deformed specimen of tube tested at ORNL.

## 5.3 LS-DYNA Modeling

### 5.3.1 Circular Tubes

As a first step in the learning process for studying tubes subjected to dynamic axial compression, circular tubes made out of aluminum studied by Al Galib and Limam (2004) were simulated in LS-DYNA®. Experimental results were used to compare the accuracy of the finite element simulations carried out in ABAQUS® by this group. One important conclusion of this study was that the thickness of the plate used to crush the tubes could highly influence the deformation mode and the peak load. Since circular tubes are not the main focus of this study, a brief description and a summary of the results will be provided in this section and the reader is referred to the work of Al Galib and Limam (2004) for more details regarding the experimental setup and other important conclusions pertaining to the circular tubes.

For verification purposes, a circular tube simulation was carried out for a tube with the geometry shown in Fig. 5.3. The specific test was conducted at a crushing velocity of 8.97 m/s. Since the reaction forces obtained were very oscillatory, we compare the first peak load and the visible deformation patterns obtained from the experiments and the simulations conducted in LS-DYNA.

Since the elastic material option in LS-DYNA was used, there isn't much to discuss about the material properties, however, the control surfaces needed to be defined for this

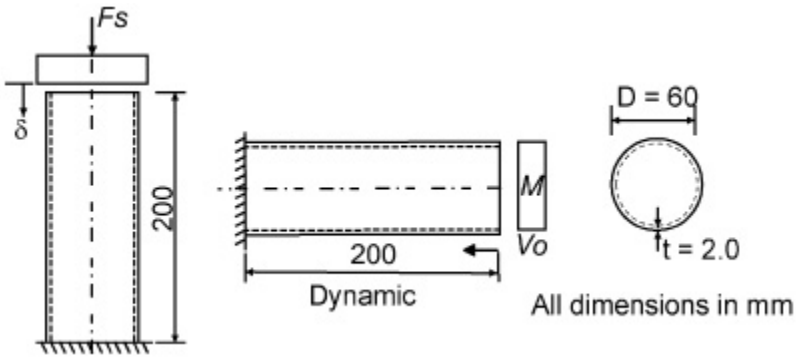


Figure 5.3: Geometry of the circular tube.

simulation are discussed here. There are two control surfaces that need to be defined for such a simulation, they are:

1. The control between the crushing plate and the tube: the elements on the plate are defined as the master and the nodes on the tube are defined as the slave.

2. A control surface for the surface of the tube also needs to be defined to prevent interpenetration when the tube starts to form lobes, *i.e.*, folds onto itself.

A convergence study on the element size was carried out and finally the tube was modeled with 60 elements circumferentially and 100 elements along the length. Also, for initiation, the crushing end of the tube is cut at an angle to the horizontal and the edges are champered as shown in the exaggerated view in Fig. 5.4. The paper did not explicitly specify the initiation criteria used, but did mention that there was an initiation mechanism provided. For our simulations, $\delta H$ was taken as 2% of the total length of the tube. The amount was taken as 2% after discussions with Dr. Mike Starbuck from ORNL

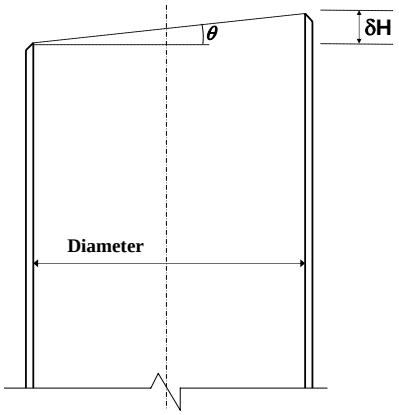


Figure 5.4: Initial champering for the circular tube at the crushing end.

who has considerable experience in energy absorption of circular tubes. Table 5.1 shows the peak load results obtained from our simulation and the experimental and numerical results given by Al Galib and Limam (2004). The results show very good agreement

Table 5.1: Comparison of peak loads and energy for dynamic tube crush of aluminum circular tubes.

| | LS-DYNA | Experimental | Numerical (ABAQUS) |
|---|---|---|---|
| Peak Loads (KN) | 118.5 | 120 | 120 |
| Energy Absorbed (J) | 3686.91 | — | 3702 |

in the peak loads and energy absorption. Deformation modes from the two numerical simulations in LS-DYNA and ABAQUS are shown in Fig. 5.5.

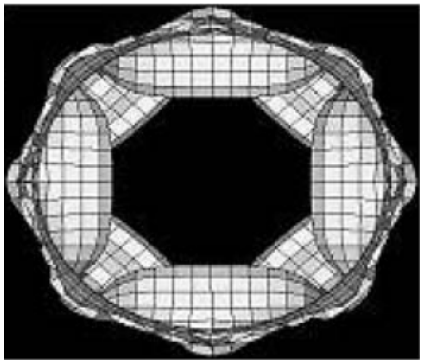

**ABAQUS simulation Galib (2004)**

**LS-DYNA simulation**

Figure 5.5: Deformation mode of the circular tube from two numerical simulations.

### 5.3.2 Square Composite Tubes

The focus in this section is on the study of square composite tubes: prediction of peak loads and the correct failure modes. Before comparing our numerical simulations to the experimental data obtained from ORNL for the tubes that are under consideration in this study, numerical simulations were carried out for experimental data available in literature. The experimental data set that has been chosen for our numerical simulation is taken from a recent paper by Mamalis *et al.* (2005). One of the primary reasons for taking these results for comparison is that the cross-section of the square tubes used in the study by Mamalis *et al.* (2005) is exactly the same as for the tubes in our study. The geometry of the cross-section is shown in Fig. 5.6. The dynamic tests were performed on an 80 Kg drop-weight test machine at an impact speed of 5.4 m/s, corresponding to a drop height of 1.5 m and average compressive strain rate approximately equal to 20 $s^{-1}$. Geometric data for the tube is shown in Table 5.2. The basic material properties

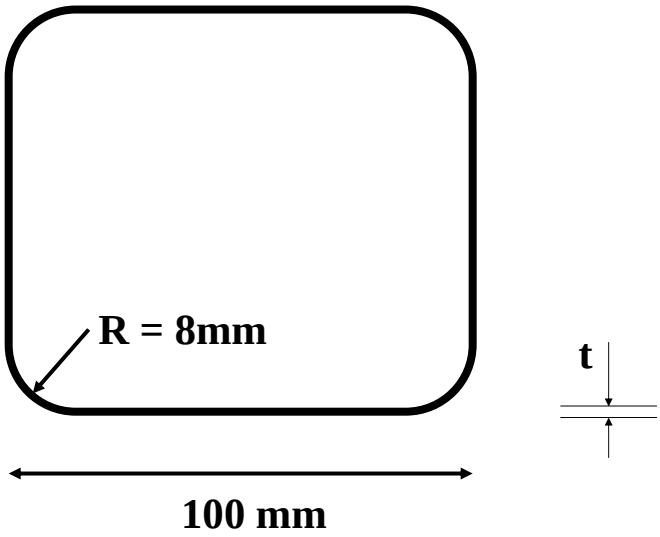


Figure 5.6: Cross section of the composite square tubes.

Table 5.2: Geometric and material data for the square tubes.

| Number of Plies | Length $L$ (mm) | Thickness $t$ (mm) |
|---|---|---|
| 18 | 50.4 | 4.33 |

for the composite material, made up of $[\pm 0]_{18}$, along with the relative symbols used in LS-DYNA are given in Table 5.3.

For these experiments carried out by Mamalis *et al.* (2005), the authors have not used any form of trigger mechanisms such as bevelling or tulip shaping of the tube ends. The material modeling of the tube was done using the in built material model in LS-DYNA, namely the

Material model 55 "mat_enhanced_composite_damage"

Table 5.3: Geometric and material data for the square tubes.

| Material Property | Symbol | Value |
|---|---|---|
| Density | $\rho$ | 1549 kg/m$^3$ |
| Elastic modulus in longitudinal direction (a) | $E_a$ | 19,900 MPa |
| Elastic modulus in transverse direction (b) | $E_b$ | 20,020 MPa |
| Shear modulus | $G_{ab}$ | 3700 MPa |
| Possion ratio between (a) and (b) directions | $\nu_{ab}$ | 0.048 |
| Possion ratio between (b) and (a) directions | $\nu_{ba}$ | 0.042 |

A brief description of the material model is given here, and detailed in the LS-DYNA3D User's and Theory Manual. Material model 55 is a model built on a set of stress-based failure criteria for the failure of the fibre and matrix under tensile, compressive, and/or shear loading. The basis of this model is the modification made by Matzenmiller to the well known Chang and Chang composite damage model (Chang and Chang (1987)). More specifically, failure of a ply subject to tensile fibre loading is assumed whenever the following condition is true:

$$\left(\frac{\sigma_{aa}}{X_t}\right) + \beta\left(\frac{\tau_{ab}}{S}\right) \geqslant 1 \tag{5.1}$$

$\beta$ is a weight factor for the ratio of the shear stress, $\tau_{ab}$, to shear strength, S, taking values in the range between 0.0 and 1.0. For $\beta = 1.0$ this condition is identical to the Hashin failure criterion for fibre tensile loading, while for the $\beta = 0.0$ condition, Eq. 5.1 corresponds to the maximum stress failure criterion which is found to compare better

to experimental results. When failure occurs, the material constants $E_a$, $E_b$, $G_{ab}$, $\nu_{ba}$, and $\nu_{ab}$ are set to zero in the corresponding layer of the composite shell element. In the case of the compressive fibre mode, failure in a ply is assumed whenever the compressive stress $\sigma_{aa}$ reaches or exceeds the compressive strength, $X_c$:

$$\left(\frac{\sigma_{aa}}{X_c}\right)^2 \geqslant 1 \tag{5.2}$$

Similar to the previous case, when failure occurs, material constants $E_a$, $G_{ab}$, and $\nu_{ba}$ are set to zero in the corresponding layer of the composite shell. Finally, regarding the matrix failure, the Tsai and Wu failure criterion ( Tsai and Wu (1971)) is adopted for both tensile and compressive matrix modes, *i.e.*, failure is assumed in a ply whenever

$$\frac{\sigma_{\mathrm{bb}}^2}{\mathrm{Y_c}Y_t} + \left(\frac{\tau_{ab}}{S}\right)^2 + \frac{(Y_c - Y_t)\,\sigma_{bb}}{\mathrm{Y_c}Y_t} \geqslant 1 \tag{5.3}$$

As before, constants $E_b$, $G_{ab}$, $\nu_{ba}$, and $\nu_{ab}$ are set to zero in the ply of the laminate where matrix failure occurred. In the above failure conditions, subscripts **a** and **b** denote the two principal material directions of a ply (*i.e.*, longitudinal and transverse directions, respectively) in the plane of the shell element with respect to the fibre orientation, while subscripts **t** and **c** denote tension and compression, respectively. **X** and **Y** are the strength values in directions **a** and **b**, respectively, while **S** represents the shear strength in the **ab** plane.

A point of particular importance related to material model 55 is the non-linear stress-

strain relationship adopted for the shear behaviour of the modelled composite materials. This consideration, which is also used in the case of other composite material models in LS-DYNA such as 22 and 54, uses the following cubic relation:

$$2\epsilon_{ab} = \frac{\tau_{ab}}{G_{ab}} + \alpha \cdot \tau_{ab}^3 \tag{5.4}$$

Obviously this non-linear relation between the shear stress and the shear strain influences the second term of the quadratic matrix failure criterion (Eq. 5.3) and also the second term of the tensile fibre mode failure criterion (Eq. 5.1) in the case in which the weight factor ($\beta$) is not zero. The non-linear shear stress parameter ($\alpha$) is estimated by the shear strength and response of the composite material.

Failure of a composite layer in a shell element can occur in any of the following four ways:

1. If the Chang-Chang failure criterion Eq. 5.1 is satisfied in the tensile fibre mode, provided that the DFAILT (maximum strain for fibre tension) material parameter is set to zero.

2. If the tensile fibre strain exceeds a prescribed maximum value (DFAILT) or if the maximum strain for fibre compression becomes less than a certain limit value (DFAILC).

3. If the maximum effective strain exceeds a prescribed value (EFS).

4. When the failure criteria that were previously described are satisfied provided that

the time-step failure parameter (TFAIL) is greater than zero.

When all composite layers of a shell element have failed, LS-DYNA eliminates that element, thus limiting the element deformation and enabling a reproduction of the brittle behavior of the composite material. In fact, the value of the time-step failure parameter TFAIL determines, to a significant degree, whether the overall crushing response of the compressed composite tube will be brittle or ductile. Smaller values of TFAIL result in a ductile behavior of the composite material similar to the response of metals or polymers, while values above 0.8 gives a brittle compressive response. The value of 0.8 represents the quotient of the actual time step and the original time step for any element. Elements sharing nodes with a deleted shell element become crash front elements, *i.e.*, elements with a reduced strength level (evaluated based on the softening factor SOFT in the material card) at which failure is more probable. The zone with reduced strength level acts as a trigger mechanism for further failure spreading, fracture propagation, and crushing of the undamaged material. This partial strength deterioration mechanism, - which is in accordance with the experimental observations, is a feature of LS-DYNA material model 55 applied by activating the crash front algorithm when TFAIL is given a positive value.

Table 5.4 compares the results from *our* simulations in LS-DYNA® to the numerical and experimental results given by Mamalis *et al.* (2005). The results obtained from our simulations are the same as given by the authors. This is expected since both the simulations used the same software and the same material models.

Table 5.4: Comparison of peak loads and energy for dynamic tube crush of square composite tubes.

| | LS-DYNA This Study | Experimental Mamalis et al. (2005) | LS-DYNA Mamalis et al. (2005) |
|---|---|---|---|
| Peak Loads (kN) | 433.26 | 426 | 433 |
| Energy Absorbed (J) | 988.67 | 1024 | 988 |

## 5.4 Unbonded Composite Square Tubes Tested at ORNL

The verification of the circular aluminum tube and the square composite tube allows us to proceed confidently to simulate the square composite tube crush being done at ORNL for this study. Experimental observation of these tubes showed that the failure mode was somewhat similar to Mode I failure at the progressive crushing end. The composite material was so brittle that on impact it shattered into small pieces and at the end of the experiment only the unimpacted tube remained. Figure 5.7 shows the various stages of the tube being crushed in the test machine at ORNL. The test machine at ORNL is a custom-built machine designed by ORNL to apply a constant velocity throughout the test. A control system has been incorporated in the machine under a feedback control system. The pneumatic pump is controlled by the feedback system. TMAC (Testing Machine for Automotive Crashworthiness) is the name given to this machine and it is a

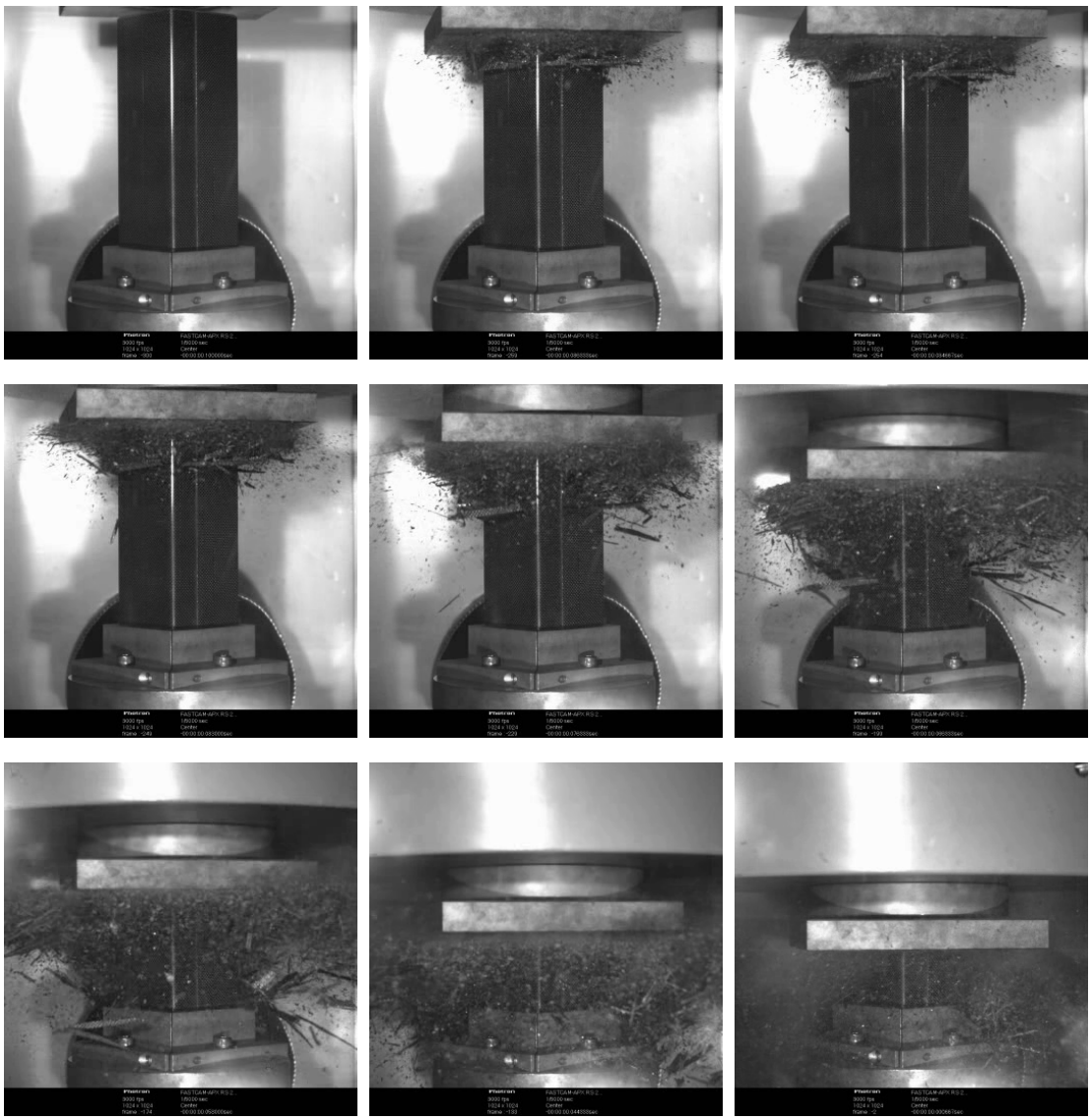

Figure 5.7: Snapshots of the square composite tube under dynamic load.

very large machine, about 6m in height. To avoid the shattered pieces of the composite tubes from flying all over the place, the tube is enclosed in a hardened transparent plastic casing. A vacuum cleaner is used to suck the shattered particles and to provide a clearer image.

As can be seen from Fig. 5.7, the failure of this square composite tube is significantly different in some aspects from the Mode I failure reported in the literature. The main difference is that the Mode I failure reported in the literature was seen only under quasi-static simulations, whereas the experiments done at ORNL exhibit the complete fragmentation of the tube under dynamic loading. To model the composite material shattering into pieces, the TFAIL option in LS-DYNA was adjusted until the desired failure pattern was achieved. The cross-section of the square tube is the same as shown in Fig. 5.6 and the length of the tube is 356 mm (14 inches). The material properties for the composite 11 ply symmetric ($0^0/45^0$) woven composite are given in Table 5.5. Simulation was carried out with a TFAIL value of 0.95. LS-DYNA® calculates this quotient for every element and deletes the element when the quotient reaches a value lower than the specified value of 0.95. As mentioned earlier for the square tubes, brittle behavior is seen for a value of TFAIL values greater than 0.8 A value equal to or greater than 0.95 makes the material very brittle and complete fragmentation of the material can be achieved.

Figure 5.8 shows the shattering of the square composite tube as simulated in LS-DYNA. Also, the figure shows the pieces of composite material flying away from the tube. Calculations for the elements flying away as rigid bodies are suppressed by LS-DYNA after

Table 5.5: Material data for the square woven composite tubes.

| Material Property | Symbol | Value |
|---|---|---|
| Density | $\rho$ | 1500 $Kg/m^3$ |
| Elastic modulus in longitudinal direction (a) | $E_a$ | 45,000 MPa |
| Elastic modulus in transverse direction (b) | $E_b$ | 40,000 MPa |
| Shear modulus | $G_{ab}$ | 1800 MPa |
| Shear modulus | $G_{bc}$ | 1400 MPa |
| Poisson ratio between (a) and (b) directions | $\nu_{ab}$ | 0.24 |
| Poisson ratio between (b) and (a) directions | $\nu_{ba}$ | 0.34 |

a few time steps to reduce the computations.

Comparing the images from the experiment and the numerical simulations, one can state with a fair level of confidence that the failure pattern, at least qualitatively, is being well captured by the numerical simulation. Based on the strain value used for calculating TFAIL, different failure modes can be achieved. Once the failure pattern has been compared, the next task is to compare the peak loads and the load history. The unbonded tube was tested at ORNL at an impact velocity of about 4 m/s. Figure 5.9 compares the reaction force from the experimental and numerical simulations. The peak loads for each of the time histories are given in parentheses in the legend. Spikes in the force history obtained from the numerical simulation correspond to the deletion of the elements and re-establishment of the crash front.

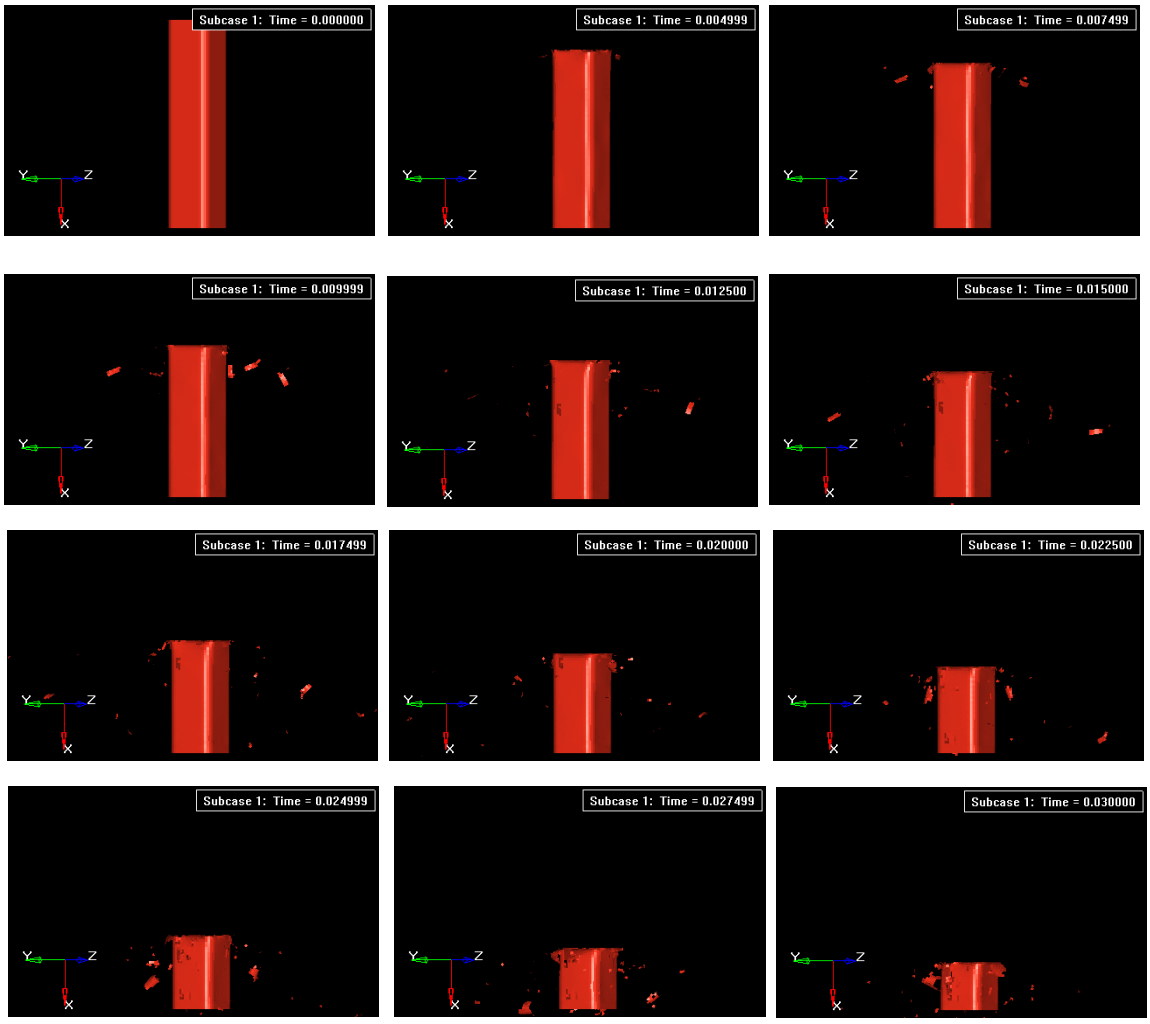


Figure 5.8: Snapshots of the square composite tube under dynamic load in LS-DYNA.

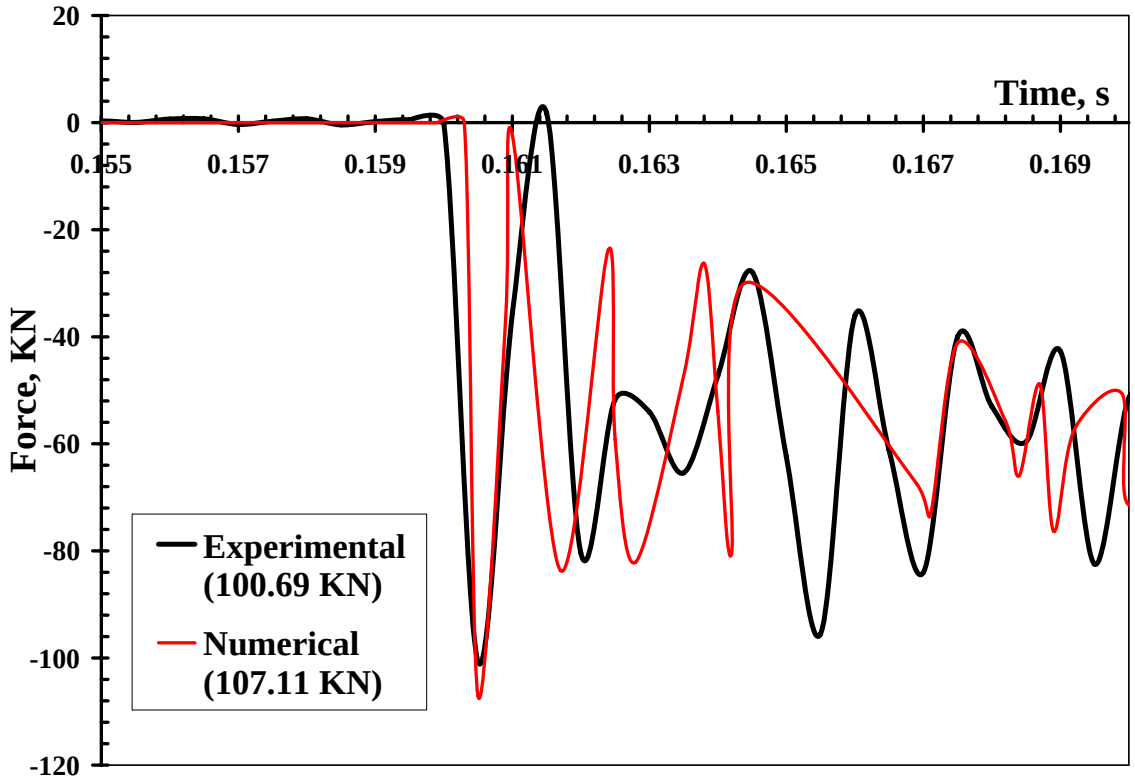


Figure 5.9: Comparison of force histories for the unbonded tube under an impact velocity of 4 m/s.

Comparison of the two load histories shows that the LS-DYNA simulation is not only capable of capturing the right failure mode, but also predicts the peak load reasonably well.

## 5.5 Bonded Composite Square Tubes Tested at ORNL

One of the goals of this study was the crash analysis of the bonded composite square tubes. The bonded tubes were made up by joining two C section with chamfered ends. Basically this would keep the cross-section of the bonded tube the same as for the unbonded tube square tube. Figure 5.10 shows a schematic representation of the cross-section of the bonded tube. The two ends of the C section are filed to reduce the plies and then the adhesive is applied. However, for the case of the finite element modeling, the joint was assumed to be an overlap, with the size of the overlap being 5mm. The overall length of the side was kept as 100 mm. The geometry is shown in Fig. 5.11. The experimental results for the bonded tube were very similar to those for the unbonded tube. In fact, the peak loads and the energy for the bonded tube were the same as for the unbonded tube. This leads to the conclusion that the failure of the bonded tube was dominated by the composite failure and not by the failure of the adhesive bond. This is very unusual, given that the adhesive bond is usually assumed to be the weakest part of any structure and is expected to be the primary reason for failure.

The numerical simulation for the bonded tube was carried out using the same material

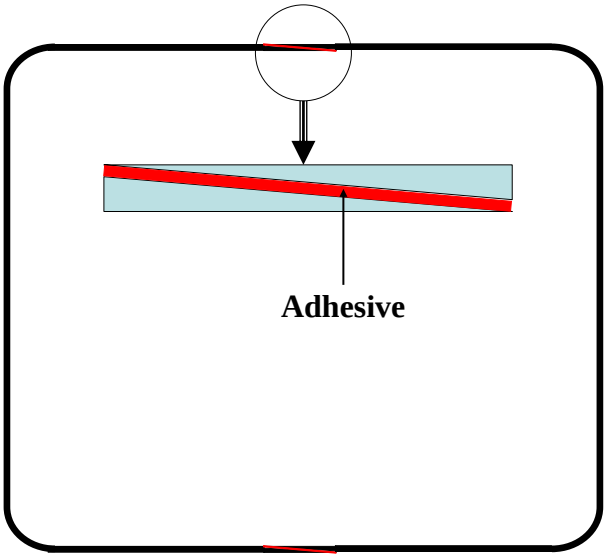


Figure 5.10: Schematic diagram of the bonded square composite tube.

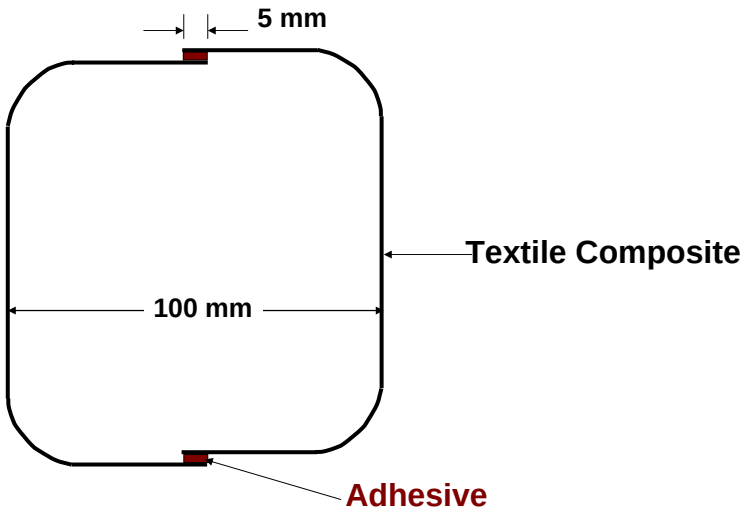


Figure 5.11: Approximated overlap joint for numerical analysis in a bonded tube.

properties for the composite and the rigid wall. Additionally, the adhesive bond was modeled using the 3D solid eight-noded library elements. The material model for this solid element was defined using the user defined option, based on the cohesive traction-displacement relations, as per the details given in Chapter 4. The properties used for the adhesive joint are listed in Table 5.6, and the main assumption here is that the properties in Mode III are taken to be the same as in Mode II due to lack of experimental data for Mode III. Another major difference in this numerical simulation is the number of contact surfaces. Four different kinds of contact surfaces were defined in the case of the bonded tube, whereas only two were needed for the unbonded tube. In addition to the contact algorithm between the rigid wall and the tube, contact algorithms for each part of the C sections were defined, and lastly a contact algorithm between the two C sections was defined.

Since the failure pattern of the bonded and the unbonded tube is hardly differentiable in the images from the numerical analysis, these images are not shown here for the sake of brevity. However, what will be compared are the peak reaction forces.

Table 5.6: Material properties for the SIA adhesive as defined in the UMAT.

| $T_1^c$ | $T_c^2 = T_c^3$ | $G_{I_c}$ | $G_{II_c} = G_{III_c}$ | $\beta$ | $K_a$ | $\rho$ |
|---|---|---|---|---|---|---|
| 40 MPa | 40 MPa | 2.2 N/mm | 4 N/mm | 1 | $10^6$N/mm$^3$ | 1000 $kg/m^3$ |

Table 5.7 shows the peaks loads from the experiments and the numerical analysis. One

can note that for all practical purposes, the peak load reported from experiments for the bonded and the unbonded tubes are the same. Comparing the results from the simulation of these tubes, one can observe that there is a about a 4% reduction in the peak loads for the bonded tube. This difference can be attributed to the approximation of the joint geometry that was done in the numerical simulation. The force time history for the bonded tube is shown in Fig. 5.12

Table 5.7: Peak loads for the bonded and unbonded square composite tubes.

| Experimental | | Numerical | |
|---|---|---|---|
| Unbonded | Bonded | Unbonded | Bonded |
| 100.69 KN | 100.37 KN | 107.11 KN | 102.67 KN |

The crashworthiness of tubes made up of different cross sections and different materials has been studied here. Numerical simulations for all the cases simulated in LS-DYNA predicted not only the correct failure mode, but also predicted the peak loads quite accurately. For the square composite tube tested at ORNL, the failure mode was unique and something that has not been observed in the literature. The element deletion option (TFAIL) in LS-DYNA allowed us to simulate this unique failure mode very accurately. The presence of the adhesive bond did not change the failure mode of the tube. The general assumption that the bond is the primary reason for failure is not valid here.

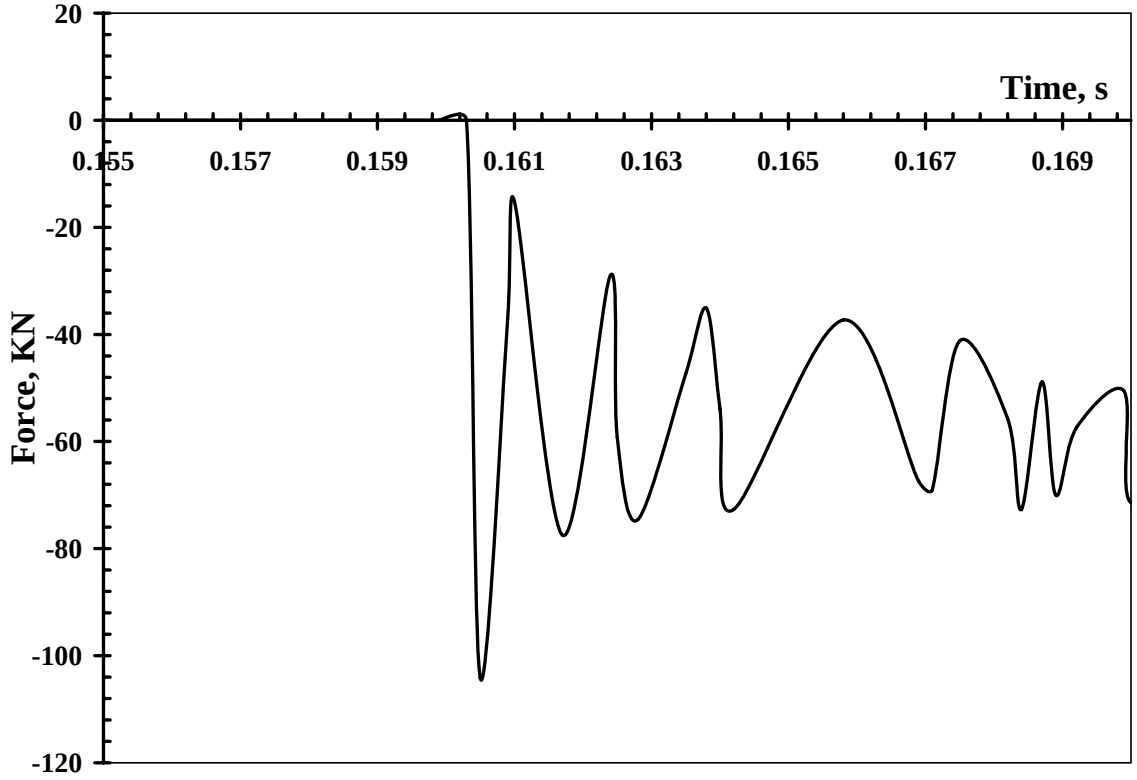


Figure 5.12: Force history for the bonded tube under an impact velocity of 4 m/s.

# Chapter 6

# Fracture Analysis Using Extended Finite Element (X-FEM)

## 6.1 Introduction

The numerical problems associated with the crack being mesh biased and convergence of the cohesive zone model implemented through the interface elements have been well documented by de Borst (2003). Although the method has proven effective in solving many problems which only a decade ago would have been considered extremely difficult if not impossible, the tedious task of placing the interface elements, which have zero thickness, makes the technique problematic for complex practical structures. One of the other things that has troubled researchers using this technique has been that the crack

path is always pre-defined in some sense. Even if the medium through which the crack is propagating is modeled with a high number of bulk and interface elements, the crack tip has limited options in terms of the direction of propagation. This makes the complete method very mesh dependent and convergence is theoretically non-existent.

A significant improvement in the field of fracture mechanics was realized with the development of a partition-of-unity based enrichment method for discontinuous fields ( Moës *et al.* (1999)). In the Extended Finite Element Method (X-FEM), special functions are added to the finite element approximation using the framework of partition-of-unity ( Moës *et al.* (1999), Durate and Oden (1996)). For crack modeling, a discontinuous function (Heaviside step function) along with linear elastic fracture mechanics equations are used to account for cracks. This enables the domain to be modeled by finite elements without explicitly meshing the crack surfaces. The location of the crack discontinuity can be arbitrary with respect to the underlying finite element mesh, and quasi-static or dynamic crack propagation simulations can be performed without the need to re-mesh as the crack advances. A particularly appealing feature is that the finite element framework and its properties are retained, and a single-field variational principle is used to obtain the discrete equations. The technique provides an accurate and robust numerical method to model strong (displacement) discontinuities, as well as weak (strain) discontinuities.

Here the derivation of the X-FEM and the implementation through a 2D plane strain finite element program will be described in detail. Part of the finite element program is written in FORTRAN and part of it is written in MATLAB. The matrices forming the

system of equations are generated in FORTRAN and the solution of these equations is done in MATLAB. MATLAB is called intrinsically from FORTRAN and the matrices are passed over to MATLAB, and after solving these equations MATLAB returns the results to the FORTRAN code where they are processed further. Advantage was taken of the fact that the FORTRAN compiler used here is COMPAQ VISUAL FORTRAN 6.6, by plotting the crack path using the graphics options in FORTRAN after every few pre-selected steps. The crack path is plotted on an initial undeformed configuration.

The formulation developed here is based on the partition-of-unity ( Melenk and Babuska (1996)). Discontinuous shape functions are used, with the magnitude of the displacement jump represented by adding extra nodal degrees-of-freedom (enhanced degrees-of-freedom) at existing nodes. Here, there are no restrictions on the allowable element types and displacement jumps are continuous across element boundaries. The displacement jump is added by extending the basis of the underlying finite element interpolation. Functions with displacement jumps are added selectively to the support of individual nodes to model a propagating discontinuity. This method has been used within the element-free Galerkin method ( Fleming *et al.* (1997)) and with finite elements ( Wells and Sluys (2001a), Moës *et al.* (1999)) to simulate cracks in elastic solids under quasi-static loading conditions.

## 6.2 Formulation

The computational modeling of propagating discontinuities has long been restricted by the computational tools available. Discontinuities have been limited to inter-element boundaries (interface elements) or the finite element mesh must be changed adaptively to capture a propagating discontinuity. Here a problem is formulated for modeling propagating cohesive cracks that cut through the elements.

To incorporate displacement jumps in a finite element interpolation, it is necessary to examine the kinematic properties of a solid in the presence of a displacement discontinuity. Consider the body $\Omega(\Omega = \Omega^+ \cup \Omega^-)$ shown in Fig. 6.1. The displacement field $\mathbf{u}$

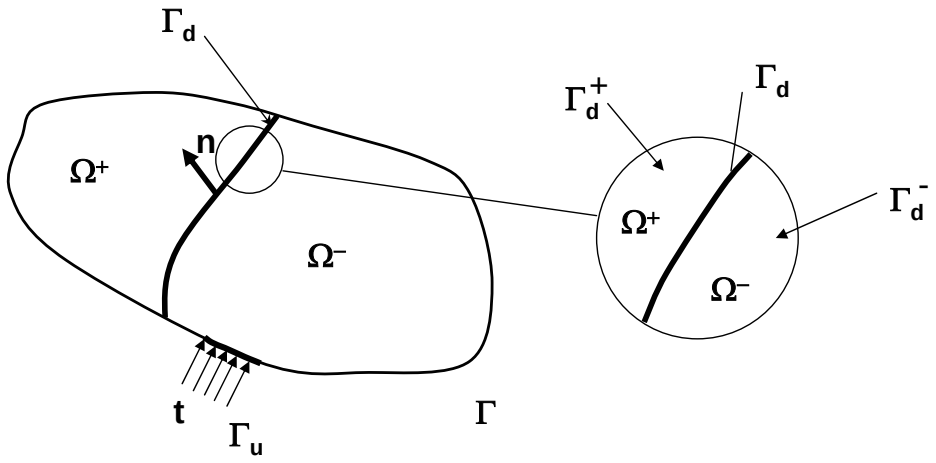


Figure 6.1: Body $\Omega$ crossed by a discontinuity $\Gamma_d$.

can be decomposed into two parts a continuous and a discontinuous part:

$$\mathbf{u}(\mathbf{x}, t) = \hat{\mathbf{u}}(\mathbf{x}, t) + \mathscr{H}_{\Gamma_d}[\![\mathbf{u}(\mathbf{x}, t)]\!] \tag{6.1}$$

where $\hat{\mathbf{u}}$ and $[\![\mathbf{u}]\!]$ are continuous functions on $\Omega$, and $\mathscr{H}_{\Gamma_d}$ is the Heaviside function centered on the discontinuity $\Gamma_d$ ($\mathscr{H}_{\Gamma_d} = 1$ if $\mathbf{x} \in \Omega^+$, $\mathscr{H}_{\Gamma_d} = 0$ if $\mathbf{x} \in \Omega^-$). The components of the displacement jump at the discontinuity are given by $[\![\mathbf{u}]\!]_{\mathbf{x}\in\Gamma_d}$.

It is possible to find the strain field for a body crossed by a discontinuity by taking the gradient of Eq. 6.1:

$$\begin{aligned} \varepsilon &= \nabla^s \hat{\mathbf{u}} + \mathscr{H}_{\Gamma_d} \left(\nabla^s [\![\mathbf{u}]\!]\right) + \left(\nabla \mathscr{H}_{\Gamma_d} \otimes [\![\mathbf{u}]\!]\right)^s \\ &= \underbrace{\nabla^s \hat{\mathbf{u}} + \mathscr{H}_{\Gamma_d} \left(\nabla^s [\![\mathbf{u}]\!]\right)}_{\text{bonded}} + \underbrace{\delta_{\Gamma_d} \left([\![\mathbf{u}]\!] \otimes \mathbf{n}\right)^s}_{\text{unbonded}} \end{aligned} \tag{6.2}$$

where $\delta_{\Gamma_d}$ is the Dirac-delta distribution centered on the discontinuity and $\mathbf{n}$ is the unit normal vector to the discontinuity (pointing towards $\Omega^+$). All strains are assumed to be infinitisimal, so $(.)^s$ indicates the symmetric part only. Due to the jump in the displacement field, Dirac's delta distributions arise in the strain field. Since the Dirac's delta distribution is unbonded, it is physically meaningless, although as is later seen, it is useful for inserting the strain field into the virtual work equation and performing the required integrals using the sifting property of this distribution.

### 6.2.1 Shape functions based on the partitions of unity

A collection of functions $\varphi_i(x)$, each belonging to a node, defined over a body $\Omega$ ($x \in \Omega$) form a partition of unity if

$$\sum_{i=1}^{n} \varphi_i(\mathbf{x}) = 1 \tag{6.3}$$

where $n$ is the number of nodal points. It has been shown by Durate and Oden (1996) that a field can be interpolated in terms of discrete nodal values using partitions of unity. Using the functions $\varphi_i$, an interpolation of $u$ over a body can be formed by

$$u(\mathbf{x}) = \sum_{i=1}^{n} \varphi_i^k(\mathbf{x}) \left( a_i + \sum_{j=1}^{m} b_{ij} \gamma_j(\mathbf{x}) \right) \tag{6.4}$$

where $\varphi_i^k$ are partition of unity functions of order $k$ (if the partition of unity functions are polynomials, $k$ refers to the polynomial order), $a_i$ are 'regular' nodal degrees-of-freedom, $b_{ij}$ are 'enhanced' nodal degrees-of-freedom and $\gamma_j$ is an 'enhanced' basis with $m$ terms. To avoid linear dependency, the order of any polynomial terms in the enhanced basis must be greater than $k$.

It is Eq. 6.4 that provides a link between meshless methods and the finite element method. The differences between the two methods lies in the choice of the function $\varphi(\mathbf{x})$. The element-free Galerkin Method ( Belytschko *et al.* (1994)) uses a weighted moving least-squares function of order $k$ having, in general, an empty (zero) enhanced basis as the partition of unity. More generally, *hp* clouds ( Durate and Oden (1996)) use a weighted

moving least-squares function of order $k$ (which can be of order zero) with a non-empty enhanced basis. Importantly, finite element shape functions are also partitions of unity, since

$$\sum_{i=1}^{n} N_i(\mathbf{x}) = 1 \tag{6.5}$$

where $N_i$ are finite element shape functions. The difference between the classical finite element method and the meshless methods lies solely in the choice of the partition of unity functions. In the conventional form of the finite element method, the order of the partition of unity function is the polynomial order of the shape function and the enhanced basis is empty. There is however no reason why the enhanced basis cannot be used with finite elements. In the finite element notation, the interpolation of the displacement field, using the partition of unity property, can be written as

$$u(x) = \underbrace{\mathbf{N(x)}\,\mathbf{a}}_{\text{standard}} + \underbrace{\mathbf{N(x)}\,(\mathbf{N}_\gamma\mathbf{(x)b})}_{\text{enhanced}} \tag{6.6}$$

where $\mathbf{N}$ is a matrix containing the usual (polynomial) shape functions of polynomial order $k$, $\mathbf{a}$ contains the regular nodal degrees of freedom, $\mathbf{N}_\gamma$ is a matrix containing the enhanced basis terms, and $\mathbf{b}$ contains the enhanced nodal degrees of freedom. The number of enhanced degrees-of-freedom per node is equal to the number of terms in the enhanced basis multiplied by the spatial dimensions. The vector form of the strain field

in terms of nodal displacements can be written as

$$\varepsilon = \nabla^s \mathrm{u} = \mathbf{B}\,\mathbf{a} + \mathbf{B}_\gamma \mathbf{b} \tag{6.7}$$

where $\mathbf{B} = \mathbf{L}\mathbf{N}$ and $\mathbf{B}_\gamma = \mathbf{L}\ (\mathbf{N}\ \mathbf{N}_\gamma)$. The matrix $\mathbf{L}$ contains the differential operators. The critical feature of the interpolation in Eq. 6.6 is that the interpolation is constructed on a per-node basis. It is possible to enhance individual nodes to improve a solution without modifying the original element mesh.

### 6.2.2 Discontinuities in the enhanced basis

Discontinuities can be added to the displacement field with the help of some discontinuous functions to the enhanced basis. Consider Eq. 6.6, the matrix $\mathbf{N}$ together with the regular degrees-of-freedom $\mathbf{a}$ can be considered to represent the continuous part $\hat{\mathbf{u}}$ of the domain $\Omega$ and the term $\mathbf{N}\mathbf{N}_\gamma$ with the enhanced degrees of freedom $\mathbf{b}$ representing the discontinuous part $\mathscr{H}_{\Gamma_d}[\![\mathbf{u}]\!]$ given in Eq. 6.1. The term representing the discontinuous part consists of a continuous function $[\![u]\!]$ interpolated by $\mathbf{N}$ and the Heaviside function $\mathscr{H}_{\Gamma_d}$ which is contained within $\mathbf{N}_\gamma$. Inserting the Heaviside function for the discontinuous part in Eq. 6.6, the displacement field can be written as

$$u(x) = \underbrace{\mathbf{N}(\mathbf{x})\mathbf{a}}_{\hat{\mathbf{u}}} + \mathscr{H}_{\Gamma_d} \underbrace{\mathbf{N}(\mathbf{x})\mathbf{b}}_{[\![\mathbf{u}]\!]} \tag{6.8}$$

The strain field in elements with active enhanced degrees-of-freedom can be expressed as

$$\varepsilon = \mathbf{Ba} + \mathscr{H}_{\Gamma_d}\mathbf{Bb} + (\delta_{\Gamma_d}\mathbf{n})\,\mathbf{Nb} \tag{6.9}$$

In other words, the regular degrees-of-freedom $\mathbf{a}$ represent the continuum part, while the enhanced degrees of freedom $\mathbf{b}$ represent the displacement jump across the displacement discontinuity. Introducing the Heaviside function, $\mathscr{H}$, to the enhanced basis for the finite element results in a displacement jump along a discontinuity of the same order as the interpolating polynomial shape functions.

### 6.2.3 Variational Formulation

The weak form of the equation of motion without the body forces is written as

$$\int_\Omega \boldsymbol{\nabla}^s\boldsymbol{\eta} : \boldsymbol{\sigma}\,\mathrm{d}\Omega + \int_\Omega \boldsymbol{\eta}\cdot\rho\ddot{\mathbf{u}}\,\mathrm{d}\Omega = \int_{\Gamma_u}\boldsymbol{\eta}\cdot\bar{\mathbf{t}}\,\mathrm{d}\Gamma \tag{6.10}$$

where $\boldsymbol{\eta}$ are admissible displacement variations, $\boldsymbol{\sigma}$ is the stress field, $\bar{\mathbf{t}}$ are external traction forces applied on the boundary $\Gamma_u$, and $\rho$ is the density. Following the Galerkin formulation (*i.e.*, space of admissible displacement variations the same as actual displacements), variations of displacements from Eq. 6.1 are decomposed as

$$\boldsymbol{\eta} = \hat{\boldsymbol{\eta}} + \mathscr{H}_{\Gamma_d}[\![\boldsymbol{\eta}]\!] \tag{6.11}$$

Inserting Eq. 6.11 and the kinematic equation (6.1) into the weak equation of motion (6.10) gives

$$\int_\Omega \boldsymbol{\nabla}^s \left(\hat{\boldsymbol{\eta}} + \mathscr{H}_{\Gamma_d}[\![\boldsymbol{\eta}]\!]\right) : \boldsymbol{\sigma}\, \mathrm{d}\Omega + \int_\Omega \left(\hat{\boldsymbol{\eta}} + \mathscr{H}_{\Gamma_d}[\![\boldsymbol{\eta}]\!]\right) \cdot \rho \left(\ddot{\hat{\mathbf{u}}} + \mathscr{H}_{\Gamma_d}[\![\ddot{\hat{\mathbf{u}}}]\!]\right) \mathrm{d}\Omega = \int_{\Gamma_u} \left(\hat{\boldsymbol{\eta}} + \mathscr{H}_{\Gamma_d}[\![\boldsymbol{\eta}]\!]\right) \cdot \bar{\mathbf{t}}\, \mathrm{d}\Gamma \tag{6.12}$$

Since Eq. 6.10 holds for any admissible variation in $\boldsymbol{\eta}$, it implies that Eq. 6.12 must hold for any admissible variations $\hat{\boldsymbol{\eta}}$ and $[\![\boldsymbol{\eta}]\!]$. Taking the gradient of the variations of displacements, Eq. 6.12 can be expressed as

$$\begin{aligned}
&\int_\Omega \boldsymbol{\nabla}^s \hat{\boldsymbol{\eta}} : \boldsymbol{\sigma}\, \mathrm{d}\Omega + \int_\Omega \mathscr{H}_{\Gamma_d} \left(\boldsymbol{\nabla}^s [\![\boldsymbol{\eta}]\!]\right) : \boldsymbol{\sigma}\, \mathrm{d}\Omega + \int_\Omega \delta_{\Gamma_d} \left([\![\boldsymbol{\eta}]\!] \otimes \mathbf{n}\right)^s : \boldsymbol{\sigma}\, \mathrm{d}\Omega + \int_\Omega \hat{\boldsymbol{\eta}} \cdot \rho \ddot{\hat{\mathbf{u}}}\, \mathrm{d}\Omega + \\
&\quad + \int_\Omega \mathscr{H}_{\Gamma_d} \hat{\boldsymbol{\eta}} \cdot \rho [\![\ddot{\mathbf{u}}]\!]\ \mathrm{d}\Omega + \int_\Omega \mathscr{H}_{\Gamma_d} [\![\boldsymbol{\eta}]\!] \cdot \rho \ddot{\hat{\mathbf{u}}}\, \mathrm{d}\Omega + \int_\Omega \mathscr{H}_{\Gamma_d} [\![\boldsymbol{\eta}]\!] \cdot \rho [\![\ddot{\mathbf{u}}]\!]\, \mathrm{d}\Omega \\
&\quad = \int_{\Gamma_u} \left(\hat{\boldsymbol{\eta}} + \mathscr{H}_{\Gamma_d}[\![\boldsymbol{\eta}]\!]\right) \cdot \bar{\mathbf{t}}\, \mathrm{d}\Gamma
\end{aligned} \tag{6.13}$$

Following integral properties for Dirac's delta and Heaviside functions, the integral whose integrand contains the Dirac's delta can be changed from a volume integral to a surface integral, since the Dirac's delta is centered on the displacement discontinuity, to eliminate the Dirac's delta term, and the Heaviside function is eliminated by changing the integration domain of integrals whose integrand contains the Heaviside function from $\Omega$

to $\Omega^+$:

$$\int_\Omega \boldsymbol{\nabla}^s\hat{\boldsymbol{\eta}} : \boldsymbol{\sigma}\,\mathrm{d}\Omega + \int_{\Omega^+} (\boldsymbol{\nabla}^s[\![\boldsymbol{\eta}]\!]) : \boldsymbol{\sigma}\,\mathrm{d}\Omega + \int_{\Gamma_d} [\![\boldsymbol{\eta}]\!]_{\Gamma_d} \cdot \bar{\mathbf{t}}\,\mathrm{d}\Gamma + \int_\Omega \hat{\boldsymbol{\eta}} \cdot \rho\ddot{\hat{\mathbf{u}}}\,\mathrm{d}\Omega + \\ + \int_{\Omega^+} \hat{\boldsymbol{\eta}} \cdot \rho[\![\ddot{\mathbf{u}}]\!]\ \mathrm{d}\Omega + \int_{\Omega^+} [\![\boldsymbol{\eta}]\!] \cdot \rho\ddot{\hat{\mathbf{u}}}\,\mathrm{d}\Omega + \int_{\Omega^+} [\![\boldsymbol{\eta}]\!] \cdot \rho[\![\ddot{\mathbf{u}}]\!]\,\mathrm{d}\Omega \\ = \int_{\Gamma_u} (\hat{\boldsymbol{\eta}} + \mathscr{H}_{\Gamma_d}[\![\boldsymbol{\eta}]\!]) \cdot \bar{\mathbf{t}}\,\mathrm{d}\Gamma \tag{6.14}$$

where $\mathbf{t}$ $(= \boldsymbol{\sigma}\mathbf{n})$ are traction forces acting at the surface $\Gamma_d$. Taking first variations $\hat{\boldsymbol{\eta}}\,([\![\boldsymbol{\eta}]\!]) = 0$ and then variations $[\![\boldsymbol{\eta}]\!]\,(\hat{\boldsymbol{\eta}}) = 0$, separate variational statements can be written as

$$\int_\Omega \boldsymbol{\nabla}^s\hat{\boldsymbol{\eta}} : \boldsymbol{\sigma}\,\mathrm{d}\Omega + \int_\Omega \hat{\boldsymbol{\eta}} \cdot \rho\ddot{\hat{\mathbf{u}}}\,\mathrm{d}\Omega + \int_{\Omega^+} \hat{\boldsymbol{\eta}} \cdot \rho[\![\ddot{\mathbf{u}}]\!]\ \mathrm{d}\Omega = \int_{\Gamma_u} \hat{\boldsymbol{\eta}} \cdot \bar{\mathbf{t}}\,\mathrm{d}\Gamma \tag{6.15}$$

$$\int_{\Omega^+} \boldsymbol{\nabla}^s[\![\boldsymbol{\eta}]\!] : \boldsymbol{\sigma}\,\mathrm{d}\Omega + \int_{\Gamma_d} [\![\boldsymbol{\eta}]\!]_{\Gamma_d} \cdot \bar{\mathbf{t}}\,\mathrm{d}\Gamma + \int_{\Omega^+} [\![\boldsymbol{\eta}]\!] \cdot \rho\ddot{\hat{\mathbf{u}}}\,\mathrm{d}\Omega \\ + \int_{\Omega^+} [\![\boldsymbol{\eta}]\!] \cdot \rho[\![\ddot{\mathbf{u}}]\!]\,\mathrm{d}\Omega = \int_{\Gamma_u} \mathscr{H}_{\Gamma_d}[\![\boldsymbol{\eta}]\!] \cdot \bar{\mathrm{t}}\,\mathrm{d}\Gamma \tag{6.16}$$

For a small volume crossed by a discontinuity inside a body (where $\bar{\mathbf{t}} = 0$), Eq. 6.16 can be rearranged as

$$\int_{\Gamma_d} [\![\boldsymbol{\eta}]\!]_{\Gamma_d} \cdot \bar{\mathbf{t}}\,\mathrm{d}\Gamma = -\left(\int_{\Omega^+} \boldsymbol{\nabla}^{\mathrm{s}}[\![\boldsymbol{\eta}]\!] : \boldsymbol{\sigma}\,\mathrm{d}\Omega + \int_{\Omega^+} [\![\boldsymbol{\eta}]\!] \cdot \rho\,\ddot{\mathbf{u}}\,\mathrm{d}\Omega\right) \tag{6.17}$$

which shows that the equation of motion is satisfied in a weak sense across a discontinuity.

Before proceeding, the assumptions for the boundary conditions are introduced. Any-

where the essential boundary conditions are imposed we assume that the enhanced displacement field is zero: $[\![\mathbf{u}]\!] = 0$. This allows us to apply the boundary conditions in the standard fashion for finite elements.

### 6.2.4 Discretized Weak Equations

Combining the weak form of the governing equation, the displacement field, and the strain field and following the Galerkin approach, the discretized displacements, gradients, and accelerations are expressed as

$$\begin{aligned}
\hat{\mathbf{u}} &= \mathbf{N}\mathbf{a} & \hat{\boldsymbol{\eta}} &= \mathbf{N}\mathbf{a}' \\
[\![\mathbf{u}]\!] &= \mathbf{N}\mathbf{b} & [\![\boldsymbol{\eta}]\!] &= \mathbf{N}\mathbf{b}' \\
\boldsymbol{\nabla}^s\hat{\mathbf{u}} &= \mathbf{B}\mathbf{a} & \boldsymbol{\nabla}^s\hat{\boldsymbol{\eta}} &= \mathbf{B}\mathbf{a}' \\
\boldsymbol{\nabla}^s[\![\mathbf{u}]\!] &= \mathbf{B}\mathbf{b} & \boldsymbol{\nabla}^s[\![\boldsymbol{\eta}]\!] &= \mathbf{B}\mathbf{b}' \\
\ddot{\hat{\mathbf{u}}} &= \mathbf{N}\ddot{\mathbf{a}} \\
[\![\ddot{\mathbf{u}}]\!] &= \mathbf{N}\ddot{\mathbf{b}}
\end{aligned}$$

where the primes indicate admissible variations. Substituting these relations in the weak form of the governing equation yields

$$\int_\Omega \mathbf{B}^T\boldsymbol{\sigma}\,\mathrm{d}\Omega + \int_\Omega \mathbf{N}^T\rho\mathbf{N}\ddot{\mathbf{a}}\,\mathrm{d}\Omega + \int_{\Omega^+} \mathbf{N}^T\rho\mathbf{N}\ddot{\mathbf{b}}\,\mathrm{d}\Omega = \int_{\Gamma_u} \mathbf{N}^T\bar{\mathbf{t}}\,\mathrm{d}\Gamma \tag{6.18}$$

$$\int_{\Omega^+} \mathbf{B}^T \boldsymbol{\sigma}\, \mathrm{d}\Omega + \int_{\Gamma_d} \mathbf{N}^T \bar{\mathbf{t}}\, \mathrm{d}\Gamma + \int_{\Omega^+} \mathbf{N}^T \rho \mathbf{N} \ddot{\mathbf{a}}\, \mathrm{d}\Omega + \int_{\Omega^+} \mathbf{N}^T \rho \mathbf{N} \ddot{\mathbf{b}}\, \mathrm{d}\Omega = \int_{\Gamma_u} \mathscr{H}_{\Gamma_d} \mathbf{N}^T \bar{\mathbf{t}}\, \mathrm{d}\Gamma \quad (6.19)$$

The stress rate in the continuum is expressed in terms of nodal displacement velocities as

$$\dot{\boldsymbol{\sigma}} = \mathbf{D}\dot{\boldsymbol{\epsilon}} = \mathbf{D}\left(\mathbf{B}\dot{\mathbf{a}} + \mathscr{H}_{\Gamma_d}\mathbf{B}\dot{\mathbf{b}}\right) \quad (6.20)$$

where $\mathbf{D}$ relates the instantaneous stress and strain rates. Constitutive relations are posed in a rate form to develop an efficient incremental solution procedure. The traction rate can be expressed in a similar form in terms of enhanced nodal velocities as

$$\dot{\mathbf{t}} = \mathbf{T}[\![\dot{\mathbf{u}}]\!] = \mathbf{T}\,\mathbf{N}\,\dot{\mathbf{b}} \quad (6.21)$$

$\mathbf{T}$ relates the instantaneous traction and discontinuity displacement jump rates. Now the weak governing equation derived in Eqs. 6.18 and 6.19 can be linearized as

$$\mathbf{M}\begin{Bmatrix} \ddot{\mathbf{a}}^{t+\mathrm{d}t} \\ \ddot{\mathbf{b}}^{t+\mathrm{d}t} \end{Bmatrix} + \mathbf{K}\begin{Bmatrix} \mathrm{d}\mathbf{a} \\ \mathrm{d}\mathbf{b} \end{Bmatrix} = \begin{Bmatrix} \mathbf{f}_{\mathrm{ext,a}}^{\,t+\mathrm{d}t} \\ \mathbf{f}_{\mathrm{ext,b}}^{\,t+\mathrm{d}t} \end{Bmatrix} - \begin{Bmatrix} \mathbf{f}_{\mathrm{int},a}^{\,t} \\ \mathbf{f}_{\mathrm{int},b}^{\,t} \end{Bmatrix} \quad (6.22)$$

where the stiffness matrix $\mathbf{K}$ is

$$\mathbf{K} = \begin{bmatrix} \int_{\Omega} \mathbf{B}^T\mathbf{D}\mathbf{B}\, \mathrm{d}\Omega & \int_{\Omega^+} \mathbf{B}^{\mathrm{T}}\mathbf{D}\mathbf{B}\, \mathrm{d}\Omega \\ \int_{\Omega^+} \mathbf{B}^{\mathrm{T}}\mathbf{D}\mathbf{B}\, \mathrm{d}\Omega & \int_{\Omega^+} \mathbf{B}^{\mathrm{T}}\mathbf{D}\mathbf{B}\, \mathrm{d}\Omega + \int_{\Gamma_d} \mathbf{N}^{\mathrm{T}}\mathbf{T}\mathbf{N}\, \mathrm{d}\Gamma \end{bmatrix} \quad (6.23)$$

the consistent mass matrix $\mathbf{M}$ is given as

$$\mathbf{M} = \begin{bmatrix} \int_{\Omega} \rho \mathbf{N}^T \mathbf{N}\, d\Omega & \int_{\Omega^+} \rho \mathbf{N}^T \mathbf{N}\, d\Omega \\ \int_{\Omega^+} \rho \mathbf{N}^T \mathbf{N}\, d\Omega & \int_{\Omega^+} \rho \mathbf{N}^T \mathbf{N}\, d\Omega \end{bmatrix} \tag{6.24}$$

and the force vectors are

$$\begin{aligned} \mathbf{f}_{ext,a} &= \int_{\Gamma_u} \mathbf{N}^T \bar{\mathbf{t}} d\Gamma \\ \mathbf{f}_{ext,b} &= \int_{\Gamma_u} \mathscr{H}_{\Gamma_d} \mathbf{N}^T \bar{\mathbf{t}} d\Gamma \\ \mathbf{f}_{int,a} &= \int_{\Omega} \mathbf{B}^T \boldsymbol{\sigma} d\Gamma \\ \mathbf{f}_{int,b} &= \int_{\Omega^+} \mathbf{B}^T \boldsymbol{\sigma} d\Gamma + \int_{\Gamma_d} \mathbf{N}^T \bar{\mathbf{t}} d\Gamma \end{aligned} \tag{6.25}$$

Having established the linearized discrete form for the governing equation, the next task is discussing the traction laws that have been used.

### 6.2.5 Traction-Separation Relations

Let us begin by defining the separation displacement $[\![\mathbf{u}]\!]$. For a two-dimensional model, the normal separation or opening displacement (Mode I) is denoted by $[\![\mathbf{u}]\!]_n$ and the shear displacement (Mode II) is denoted by $[\![\mathbf{u}]\!]_s$. The normal traction force $t_n$ transmitted

across a discontinuity is made an exponentially decaying function given by

$$t_n = f_t \,\mathrm{Exp}\left(-\frac{f_t}{G}[\![u]\!]_n\right) \tag{6.26}$$

where $f_t$ is the tensile strength of the material, and $G$ is the critical strain energy release rate. The shear traction denoted by $t_s$ acting along a discontinuity is also given by a similar exponential form:

$$t_s = f_t \,\mathrm{Exp}\left(-\frac{f_t}{G}[\![\mathbf{u}]\!]_s\right) \tag{6.27}$$

The relations for the traction forces on a discontinuity in terms of crack displacement are represented in terms of the nodal velocities (for rate dependent properties):

$$\left\{\begin{array}{c} \dot{t}_n \\ \dot{t}_s \end{array}\right\} = \underbrace{\left[\begin{array}{cc} -\frac{f_t^2}{G}\mathrm{Exp}\left(-\frac{f_t}{G}[\![u]\!]_n\right) & 0 \\ 0 & -\frac{f_t^2}{G}\mathrm{Exp}\left(-\frac{f_t}{G}[\![u]\!]_s\right) \end{array}\right]}_{\mathbf{T}} \left\{\begin{array}{c} [\![\dot{\mathbf{u}}]\!]_n \\ [\![\dot{\mathbf{u}}]\!]_s \end{array}\right\} \tag{6.28}$$

Simplified models with significant computational advantages have been used before ( Wells and Sluys (2001b)). The main assumption in these models is that the crack shear stiffness is assumed to be a constant. Numerical problems with this assumption like stress locking, are detailed in a study by Wells and Sluys (2001a)

## 6.3 Implementation

The main goal here is the addition of the extra degrees-of-freedom to specific nodes when a discontinuity passes through an element or a group of elements. Enhanced degrees of freedom are added to any node whose support has been crossed by the discontinuity. The advantage here is that as the crack grows, extra degrees of freedom can be added only to a certain group of elements, making this more efficient. To simulate a crack tip, it is important that there is no displacement jump at the crack tip. In this study, this is achieved by enforcing the crack to coincide with element boundaries and the nodes on this boundary are not enhanced. This is explained in Fig. 6.2. Another approach of al-

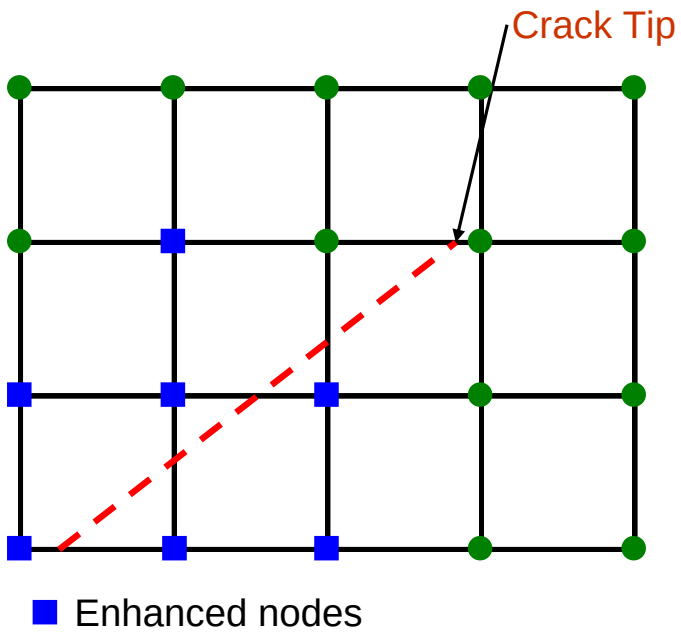


Figure 6.2: Elements crossed by discontinuity and the enhanced nodes.

lowing the crack tips inside the elements, by using the ramp functions, leads to numerical

convergence difficulties as shown in a detailed study by Wells and Sluys (2001b). The restriction of discontinuity tips to element boundaries, however, is not significant since within the cohesive zone concept no energy is dissipated upon crack extension, so the numerical results are less sensitive to the length of extension.

At the end of a load increment, the condition for the extension of a discontinuity is checked at each integration point in the element ahead of the crack tip. If the criterion is met, the normal vector to the discontinuity is calculated and a straight discontinuity is extended through an entire element. The condition for the extension of a discontinuity is then repeated until the criterion for introducing a crack is no longer met. At this point, the next load increment is applied. It is therefore possible for a discontinuity to propagate through several elements at the end of one load increment.

Numerical integration of elements that are crossed by the crack is also a matter of concern. The integration scheme in these elements is adjusted such that integration points are located on the discontinuity (two in this case) in order to integrate the traction forces. Also, for proper evaluation of the stiffness matrix on both sides of the discontinuity, each subdomain is integrated separately.

FORTRAN is used to get the element level matrices and to assemble this system of equations. Following the procedure given in the reference manual for COMPAQ VISUAL FORTAN 6.6, an intrinsic subroutine was established to call MATLAB from this software. The solution of the system of equations using the Newton-Raphson Method ( Jirásek and Bažant (2002)) was implemented in MATLAB. Iterations for establishing equilibrium

were done in MATLAB and the converged solution vector was then passed back to FORTRAN. The extra system files needed to integrate FORTRAN and MATLAB are well documented in the reference manual. Visual options in FORTRAN were used to plot the undeformed geometry, and this image was updated with the crack information at a pre-specified step number. Details of the workspace settings for using the Visual options in FORTRAN, with examples, are available in the reference manual.

## 6.4 Numerical Examples

The code needs to be verified against numerical and experimental results available in the literature. For this purpose, two problems from the study by Wells and Sluys (2001a) are chosen. First a three-point bending test is simulated using this technique and then reaction forces for a single-edged notched (SEN) beam is verified.

### 6.4.1 Three-point bending test

The geometry of the three-point bend specimen is shown in Fig. 6.3. An incremental displacement loading is applied at the center of the beam on the top edge. The material properties taken for this numerical study are: Young's modulus $E = 100$ MPa, Poisson's ration $\nu = 0.2$ ( Wells and Sluys (2001a) cite the value of $\nu$ as 0.0; the numerical value of 0.2 was established via correspondence with the Prof. Sluys),tensile strength $f_t = 1.0$ MPa, and fracture energy $G$=0.1 N/mm.

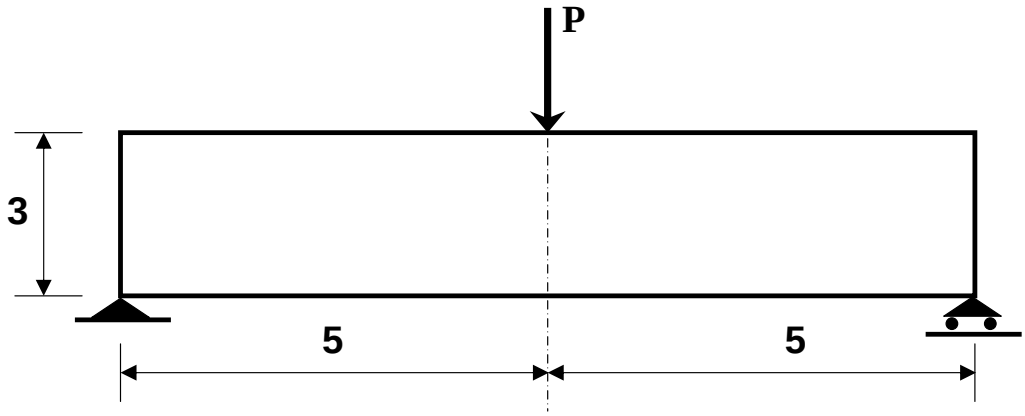


Figure 6.3: Geometry of three-point bend test. All dimensions in millimeters.

Fig. 6.4 shows the crack path obtained from the X-FEM approach developed here. As can be seen from the figure, the crack initiates at the center of the beam and propagates directly upwards towards the load point. To compare the load-displacement response, the curve given by Wells and Sluys (2001a) is digitized and the data from the present simulation is plotted. Even after taking into account errors induced due to digitization of the curve, the results match pretty well as shown in Fig. 6.5.

### 6.4.2 Single-edge Notched (SEN) beam

Experimentally, it has been observed that for an SEN beam (Fig. 6.6) a curved crack propagates from the notch towards the right side of the applied load ( Schlangen (1993)). Reasonable load-displacement curves for the SEN beam modeled with continuum models can be obtained, but the curved crack path is not captured. For the analysis of the SEN beam, the following material properties are used: Young's modulus $E$=3.5 $\times$ $10^4$

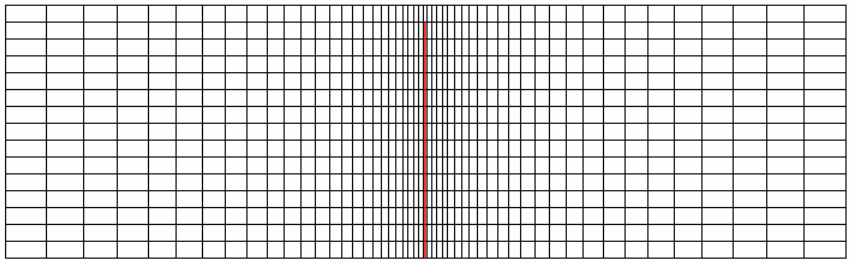

Figure 6.4: Crack path for a three-point bending test.

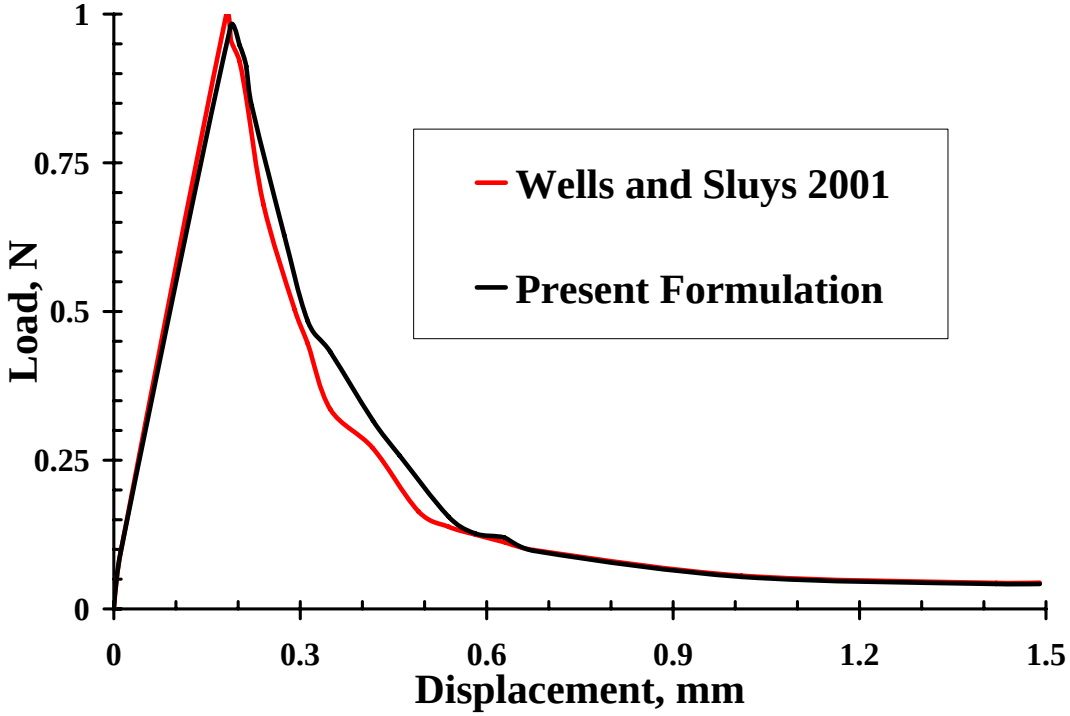


Figure 6.5: Load-displacement response for three-point bending test.

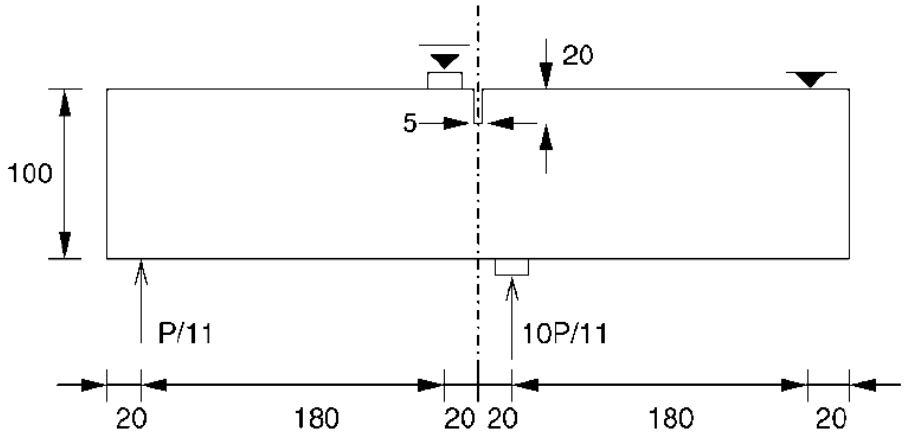


Figure 6.6: Single-Edge Notched (SEN) beam. All dimensions in millimeters.

MPa, Poisson's ratio $\nu = 0.2$, tensile strength $f_t = 3.0$ MPa, and fracture energy $G = 0.1$ N/mm. The material properties have been taken from Schlangen (1993). The calculation is performed under displacement control.

The finite element mesh along with the crack path are shown in Fig. 6.7. For the initiation of the crack, the principal stress criterion has been used. The crack path obtained using the current formulation is similar to the one observed experimentally. Comparing the load curves, the post peak load curve from the current simulation is closer to the experimental curve than the one obtained from the formulation used by Wells and Sluys (2001a). This improvement in the results is due to the fact that the current formulation does not assume the shear stiffness to be constant like the authors do in the aforementioned study.

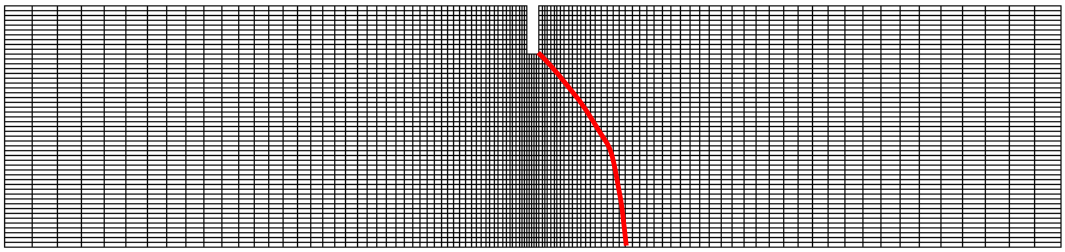

Figure 6.7: Crack path for an SENB. The crack is shown by a heavy red line.

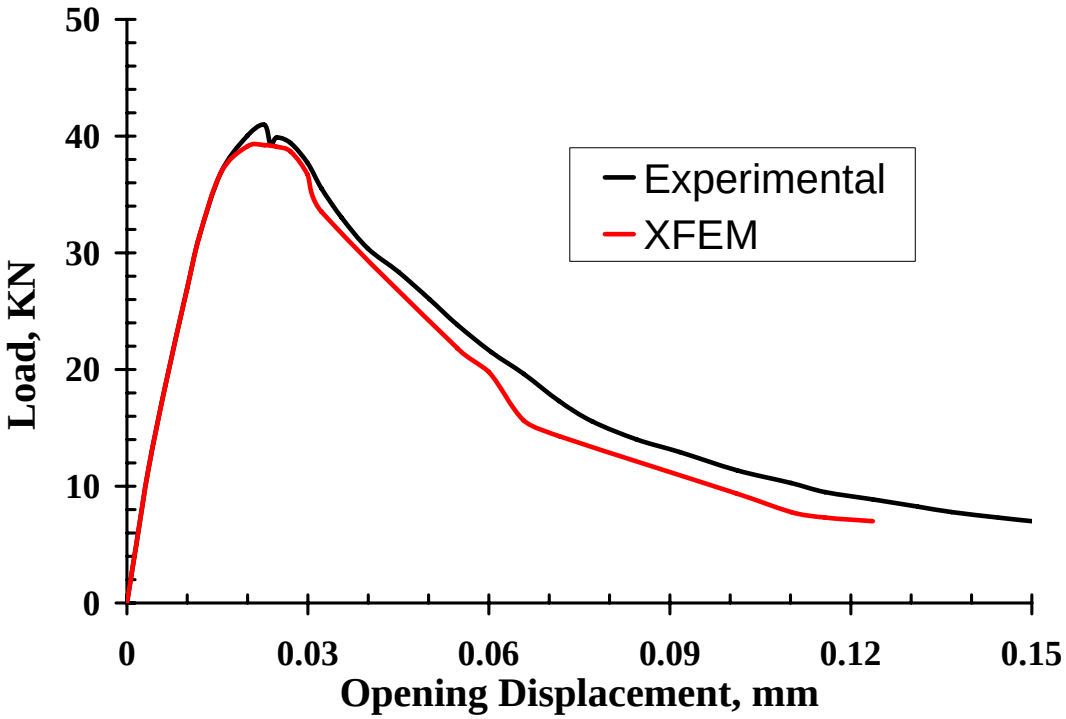


Figure 6.8: Load-opening displacement for SENB for experimental and numerical results

### 6.4.3 Dynamic Fracture of Functionally Graded Material

Advance material processing methods developed in recent years have made it possible to introduce compositional gradients in many material systems ( Bishop *et al.* (1993), Parameswaran and Shukla (2000)). The resulting materials with spatial variations in properties are collectively referred to as Functionally Graded Materials or FGM. A typical FGM includes nano- and/or micro-scale fillers suitably dispersed in a matrix material. Recently Kirugulige *et al.* (2005) studied the fracture related benefits of compositional grading under low-velocity loading conditions. For the monotonically graded glass-filled epoxy studied by the authors, they have shown that it is possible to lower crack tip loading rates, delay crack initiation, and enhance overall fracture toughness in graded structures.

Kirugulige *et al.* (2005) have tested two kinds of functionally graded material, 1) graded foam with monotonic volume fraction variation and 2) foam core with bilinear volume fraction variation for sandwich structures. Both the materials were tested in a three-point bend configuration. The impacting speed was 5.8m/s. The X-FEM code developed in this study is tested against both these experimental results.

#### 6.4.3.1 Monotonically Graded Foams

Graded syntactic foam sheets with volume fraction varying from 0% to 45% of micro-balloons in the epoxy binder were used for the experiments. For the details of the

manufacturing of these specimens and their testing, the reader is referred to the original paper by Kirugulige *et al.* (2005). The dimensions of the specimens tested were 152 mm × 45 mm × 8 mm. Variations of the Young's Modulus and the mass density along the thickness of the specimens were determined by the authors and is reproduced in Fig. 6.9.

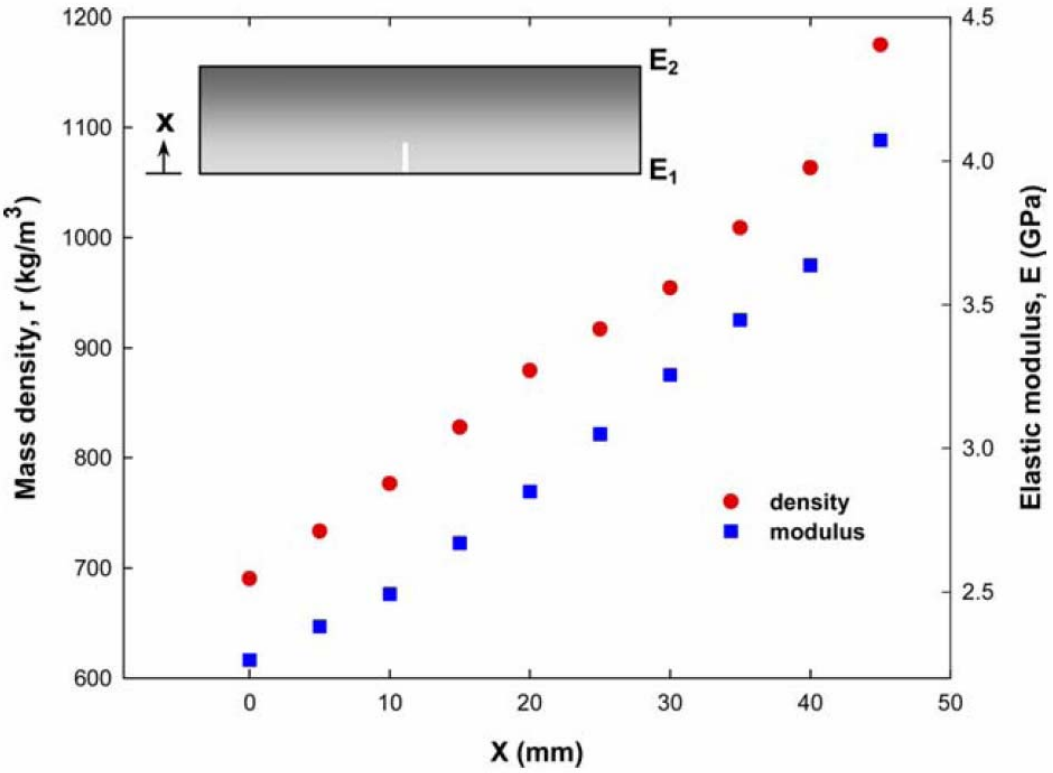


Figure 6.9: Property variations in graded foam with monotonic volume fraction variation.

Experiments on monotonically graded foam sheets included two types: (a) crack on the stiffer side of the core material with impact occurring on the compliant side and (b) crack on the compliant side of the core material with impact occurring on the stiffer side. Denoting the elastic modulus of the edge of the cracked sheet behind the crack tip as E1

and the one ahead of the crack as E2, the former corresponds to E2 < E1 and the latter to E2 > E1.

For the purpose of simulation, a mesh similar to the one shown in Fig. 6.4 was used. The crack path was vertical and the mesh and the crack path are the same as shown in Fig 6.4. Instantaneous crack length for the two different cases of monotonically graded foam sheets are shown in Fig. 6.10. As can be seen from this figure, the present approach captures the instantaneous crack length very well. Also, the crack initiation occurs earlier in the case of the specimen with a crack on the compliant side (E2 > E1) when compared to the one with a crack on the stiffer side (E2 < E1). For both simulations, the principal stress criterion was used for the crack initiation ($f_t = 63$ MPa) and the fracture energy was kept constant as $G = 0.3667$ N/mm.

#### 6.4.3.2 Foam Core for Sandwich Structures

The specimens used for the sandwich structures were 152 mm × 42 mm × 8 mm in dimensions. The core was created using two functionally graded foams discussed in the previous section bonded between epoxy face sheets (3mm thick). Also, for comparison a conventional sandwich structure of exactly the same dimensions but with a homogeneous core is tested. Both conventional and graded sandwich structures with their bilinear variation in properties are shown in Fig. 6.11

The simulation was carried out using the von-Mises criterion for crack initiation and the

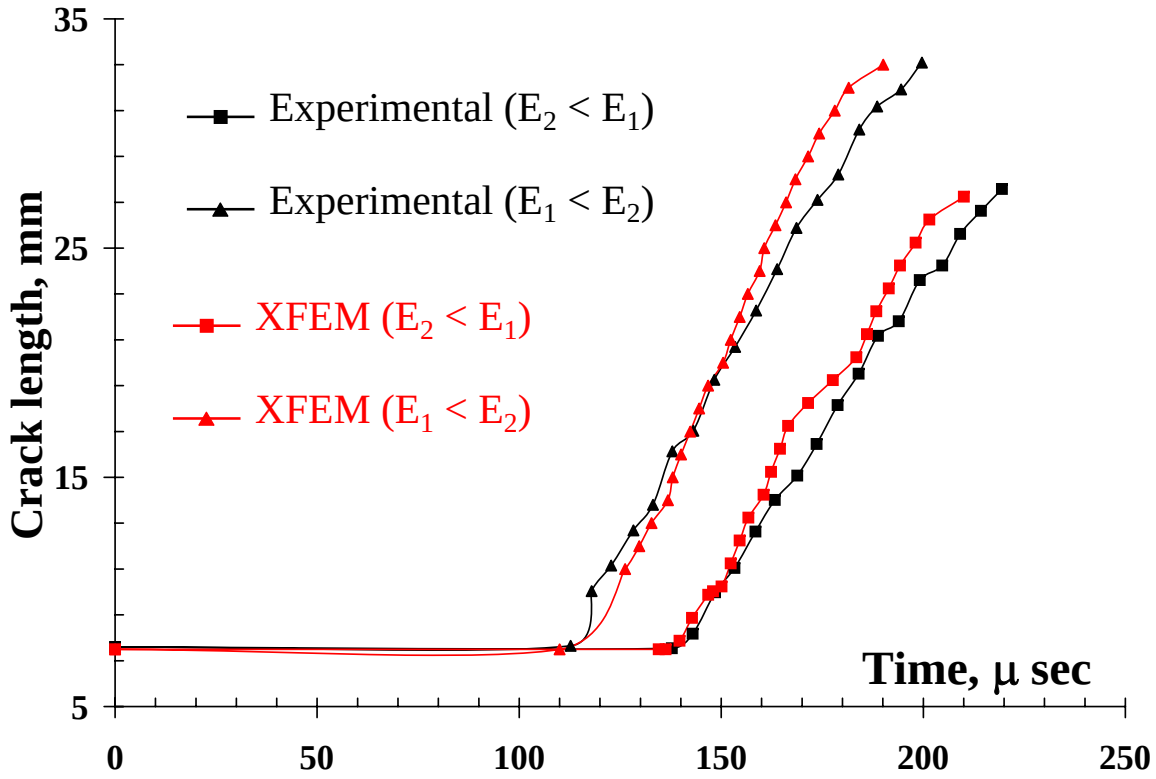


Figure 6.10: Crack growth comparison in a graded foam specimen under impact loading.

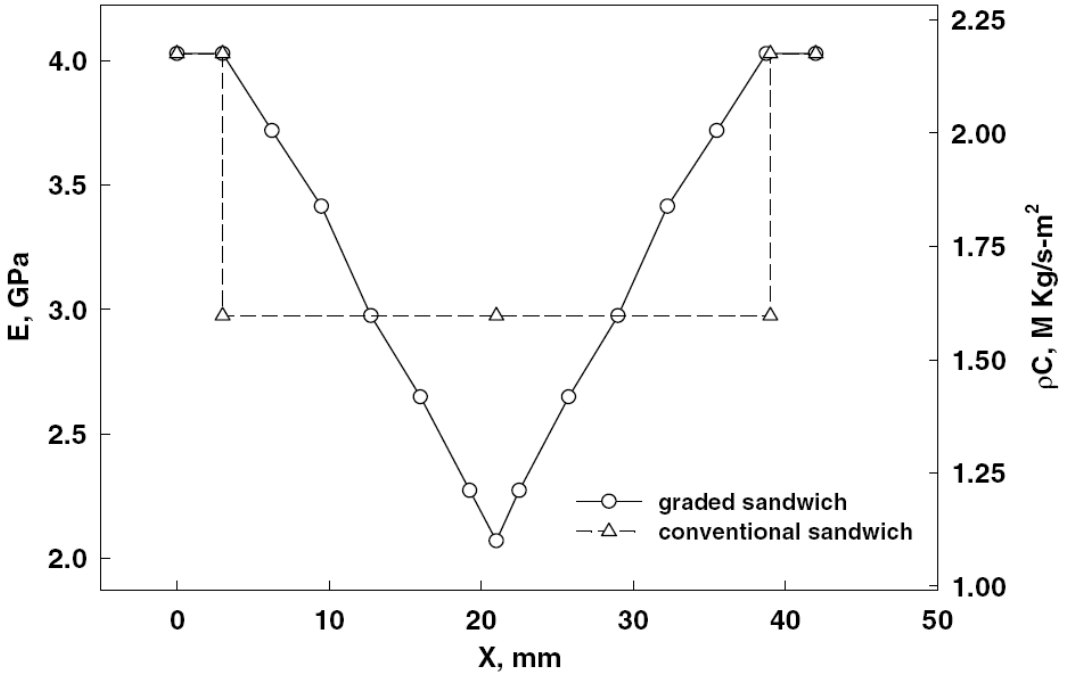


Figure 6.11: Variation of elastic modulus and elastic impedance along the specimen height.

failure stress was varied bilinearly in the core similarly to the elastic modulus variation shown in Fig. 6.11. The lowest failure stress was kept at 38 MPa at the center of the core and went up to 63 MPa at the interface of the core and the face sheets. The failure stress valus for the face sheets were kept as 68 MPa. In a similar fashion, the fracture energy was varied from 0.2 N/mm at the center to 1.6 N/mm at the interface. The epoxy face sheets had a fracture energy, $G$, of 1.8 N/mm.

The crack growth histories from the simulations and the experiments are compared in Fig. 6.12. The figure shows that there is not much difference between the crack growth histories for the conventionally manufactured sandwich specimen and the functionally graded sandwich specimen. The simulations using X-FEM capture the crack growth pattern quite accurately. However, a time lag can be seen between the experimental and numerical results for the crack initiation. This may be primarily because of the lack of information on the material properties for the epoxy face sheets. Personal correspondence with the authors failed to provide any further information on this aspect.

### 6.4.4 Double Cantilever Beam

The X-FEM technique has come a long way since the fundamental concept of partition-of-unity was put forth by Moës *et al.* (1999). However, the literature seems to be missing the application of this technique to the Double Cantilever Beam (DCB), which is another one of the most extensively used test configurations to estimate the fracture toughness

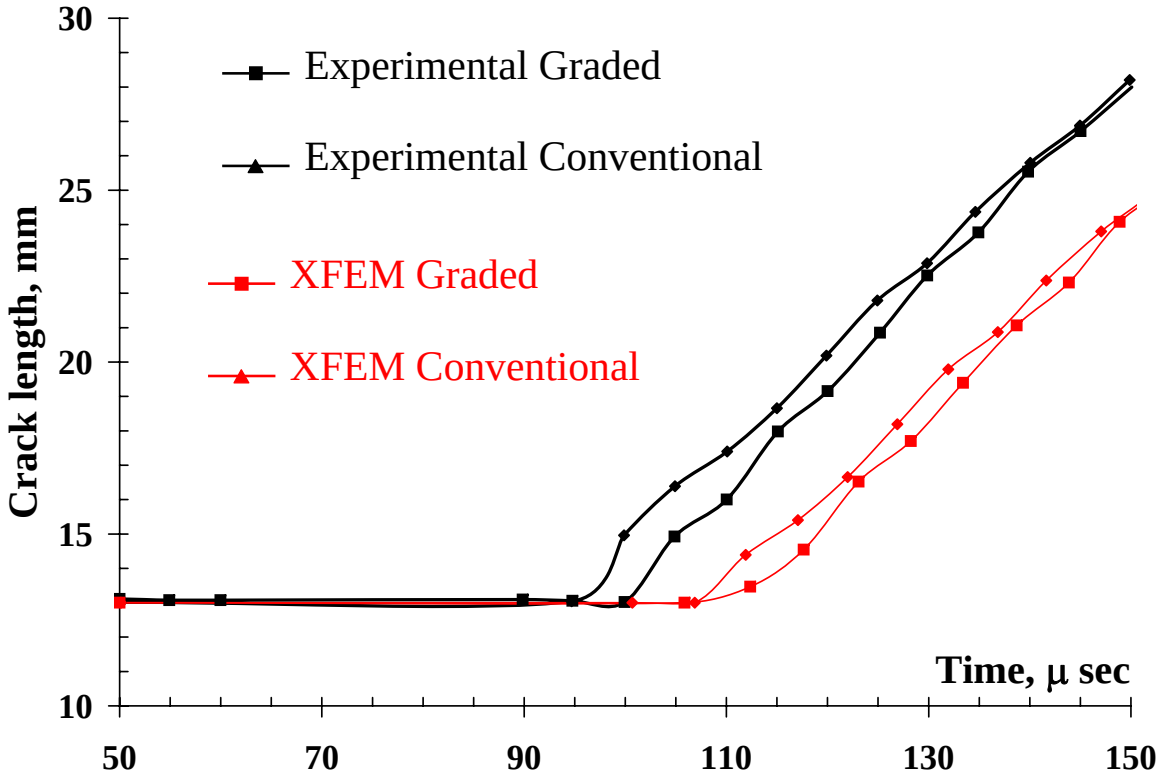


Figure 6.12: Crack growth comparison for conventional and graded sandwich beams.

for Mode I. In the previous chapters, DCB's have been the focus of this study. Here we extend the formulation of the X-FEM to analysis aluminum DCB's under quasi-static and dynamic conditions.

For the quasi-static case, the experiment discussed in Section 2.2.2 is simulated using the X-FEM technique. The material properties and the geometry of the specimen are not repeated here for the sake of brevity. Figure 6.13 shows part of the mesh used for modeling the adhesive. The pre-crack was induced by keeping the elements along the

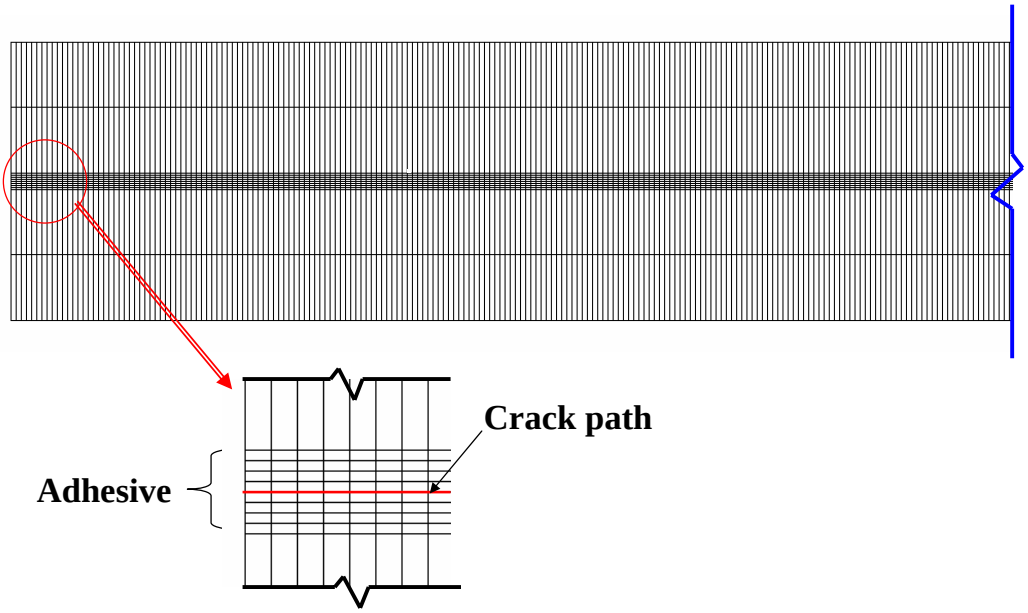


Figure 6.13: Aluminum DCB bonded with LESA adhesive. Adhesive thickness 0.8mm.

crack separated from each other. The edges of the elements along the pre-crack rest on each other but they do not share the same nodes, *i.e.*, there is no continuity between them. The crack propagated more or less along a straight line from the crack tip to the clamped end. The principal stress criterion was used for crack initiation. Figure 6.14 shows the

tip reaction forces and compares the results obtained from experiments, interface element approach, and the X-FEM approach. The comparison shows that the X-FEM approach predicts the tip reaction forces pretty well.

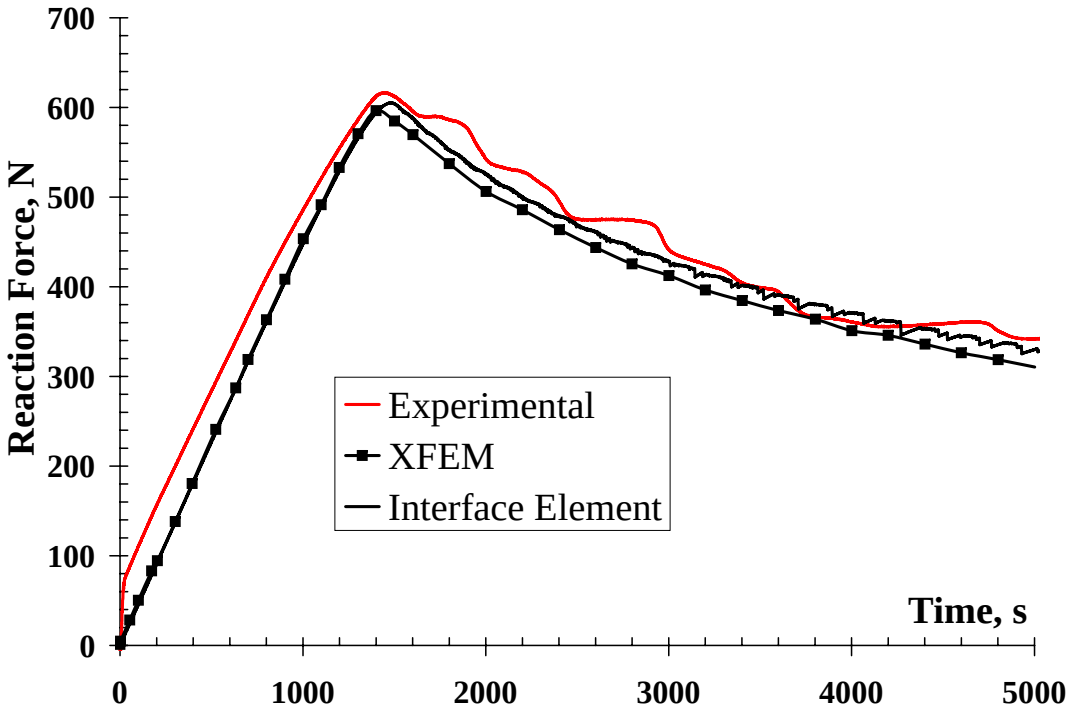


Figure 6.14: Reaction forces history for aluminum DCB bonded with LESA.

One of the major advantages which was noticed while running this simulation is that the interface element approach required about 48 hours to solve this same problem, whereas in spite of having more elements in the current approach, the time required to achieve the solution was about 5 hours. This is a major reduction in the analysis time. Also, it was not necessary to add any elements to the input file manually. The creation of the input file for the current approach hardly took any effort, which cannot be said for the

interface element approach even for the simple case of modeling the adhesive only with one layer of interface elements.

Experimentally it has been observed that the crack propagation is generally not straight, but follows a 'hacking' pattern. One of the things neglected in the above mentioned analysis is the fact that the material discontinuity has not been taken into account while calculating the criteria for the crack propagation. Referring to Section 2.5, the interface between the aluminum and the adhesive generally has a lower critical strain energy release rate than the adhesive itself. To achieve this distribution in the X-FEM approach, the concept of FGM is applied to the adhesive material. The adhesive is assumed to have the original critical energy release rate at the center and it varies linearly towards the interface with the value at the interface being 80% of the value at the center. Figure 6.15 shows the 'hacking' pattern observed in the crack path upon implementing the variation of the critical strain energy release rate. However, there is no significant numerical change in the peak reaction force predicted from this analysis. The post peak response shows some difference, but the percentage difference is less than 2% at any given instant of time. To re-emphasize the advantages of the present approach, using about 8,000 elements we were able to capture the crack path, whereas it took us about 80,000 elements, 10 times more than the current approach, in the interface approach to capture the crack path correctly. The CPU time savings were also enormous, including the time required to create an input file and the time required for the analysis.

Dynamic simulations of an aluminum DCB with the cohesive zone model implemented

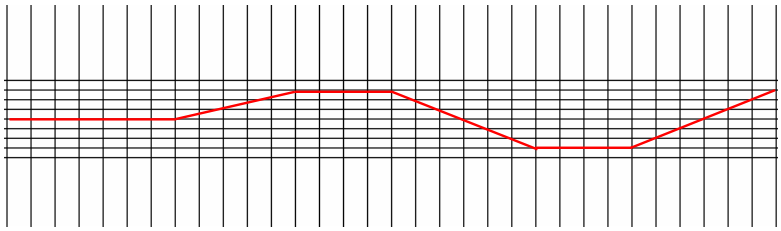

Figure 6.15: Crack path with functionally graded properties for the adhesive. Adhesive thickness 0.8mm.

through a material model in LS-DYNA discussed in Section 4.6 are simulated using the present X-FEM approach. The finite element mesh is similar to the one shown in Fig. 6.13. The variation of the critical fracture energy along the thickness of the adhesive is also implemented. Figure 6.16 compares the instantaneous crack lengths predicted from the present approach to those obtained experimentally and predicted from LS-DYNA.

The present formulation for X-FEM predicts the crack pattern and the tip reaction forces very well for both the quasi-static and dynamic aluminum DCB. Analysis of composite DCB's is more involved, due to the failure pattern of the composites. The current formulation is not capable of modeling the physics involved in the failure of composite panels. This is something that will be discussed in the next chapter where certain ideas for improving the current model are laid out under the future work section.

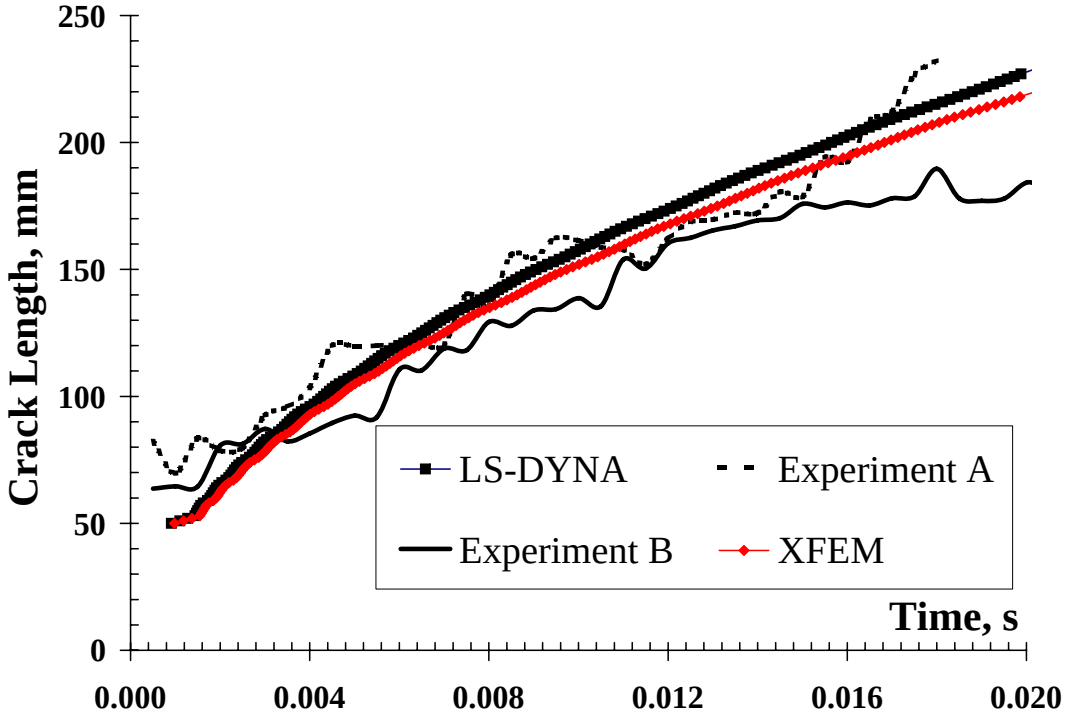


Figure 6.16: Crack growth history for a aluminum DCB simulated under dynamic conditions.

# Chapter 7

# Concluding Remarks and Future Work

The general aim of this dissertation was to formulate and implement a computational model for studying the mechanics of the crack growth in adhesively bonded joints, based on certain experiments carried out on standard test configurations for different modes of failure. To assess the theoretical developments, the failure of different structural configurations ranging from coupon tests to structures of realistic size were simulated. Different approaches like the interface element, smeared formulation, and the extended finite element have been presented to study the crack propagation, and the merits and demerits of each of them have been discussed. In this chapter, first, the conclusions of this dissertation are presented, and second, several suggestions are made for future work.

## 7.1 Concluding Remarks

Based on the techniques used, the concluding remarks are divided in three subsections. The first subsection will discuss the Cohesive Zone Model (CZM) applied through the interface element approach and the rate dependent models. The second subsection will discuss the implementation of the cohesive zone model through a material model in an explicit code and the analysis of the square composite tube in LS-DYNA. The last subsection will discuss the remarks on the Extended Finite Element Method (X-FEM), its advantages and its application to standard test configurations.

### 7.1.1 Interface element approach for CZM

An initial crack and self-similar progression of cracks is usually assumed with traditional fracture mechanics approaches. Theoretical and numerical tools to mathematically describe non-self-similar progression of cracks without having to specify an initial crack developed by Goyal (2002) were used. A cohesive-decohesive model, similar to the cohesive zone model known in fracture mechanics as the Dugdale-Barenblatt model, was adopted to represent the degradation of the material ahead of the crack tip. This model unifies strength-based crack initiation and fracture-based crack progression.

Stable and unstable crack growth observed in the experiments are defined. Crack growth is defined as stable or unstable based on the histories of the tip reaction forces and the instantaneous crack growth. In a displacement controlled experiment, the crack

growth is said to be ***unstable*** if the crack jumps in spite of no incremental displacement being applied. The interface element technique was not able to capture this unstable crack growth when the adhesive was modeled using only interface elements. A detailed modeling of the adhesive using a large number of bulk elements and interface elements captured the unstable crack, but it was computationally very expensive. In addition to the time it took to analyze, the time taken to prepare the input file was very high since a computer code had to be written to generate this input file.

Based on the compact tension test carried out on neat adhesive specimens, a procedure for the formulation of a rate dependent model has been suggested, and based on this procedure, two rate dependent models were formulated. The experiments showed that the critical strain energy release rate $G_c$ reduces with high rates of loading. This is contradictory to almost all rate dependent models available in the literature. One of the two rate dependent models failed to converge in an implicit code. The other, however, when implemented into ABAQUS along with the interface element formulation, captured the unstable crack growth, but was very expensive computationally. It took twice the time as that for the detailed model of the adhesive using bulk and interface elements. The creation of the input file was not as tedious, however.

Rate independent and rate dependent modeling were able to capture the unstable crack growth but are not computationally economical. The main concern here is that the analysis of realistic structural configurations using these formulations would be computationally very expensive, if not impossible, based on the computational resources needed

for analyzing a simple test configuration such as the DCB.

### 7.1.2 Material Definition approach for CZM

The cohesive zone model was implemented in the explicit commerical code LS-DYNA. Since this code does not have the facility to incorporate the user defined element, as ABAQUS does, the CZM was implemented through a user defined material model (UMAT). Both the rate independent and the rate dependent models were implemented in the commercial code. The procedure for writing a UMAT subroutine in LS-DYNA has been detailed because it is not easily available in the open literature. This may prove to be very useful to other researchers involved with studying dynamic fracture of new, advanced materials such as functionally graded materials, materials with nano-particles embedded in them, and composite materials in general.

The CZM model in LS-DYNA is verified against experimental results for the aluminum DCB. For beams that are not very stiff, like the 11-ply composite beam studied here, the interaction between the falling edge and the bearings (loss of contact) leads to the stick-slip behavior in the crack growth. End Loaded Split (ELS) specimens are also computationally simulated and the results are compared to the experimental data.

Furthermore, the composite tubes under axial crushing are studied using LS-DYNA. The main goal was to achieve the right failure mode. The tubes under axial loadings shattered in small pieces. This was simulated using the element deletion criteria in LS-

DYNA. Using the fracture energies obtained from the experiments, a bonded square composite tube was also simulated. The simulations and the experimental data were in good agreement and the main conclusion drawn from this study was that the bond/joint in the bonded tube was not the primary mode of failure. Contrary to the assumptions that the bond is the weakest part of any structure, the energy absorption and the failure modes of the bonded tube were identical to those for the unbonded tube.

### 7.1.3 Extended Finite Element

This innovative concept based on the partition-of-unity proposed by Moës *et al.* (1999) is implemented. The current approach available in the literature is extended to incorporate the inertia effects for dynamic cases. One of the main advantages here is that the creation of the input file is just like any other regular finite element method. No special elements need to be added. Since the crack path is independent of the finite element grid and can cross through the elements, the results are not as mesh dependent as in the case of the interface element approach. Several test configurations have been simulated and compared to experimental results. The results not only compare well to the experimental results, but also the simulations are computationally less expensive.

The crack is allowed to grow through the elements as against the conventional methods of allowing it to grow along the edges of the elements as is the case with the interface element approach. The technique is based on introducing additional degrees-of-freedom

known as the enhanced degrees-of-freedom. Additional degrees-of-freedom are added only to those nodes whose supports have been crossed by a discontinuity. This reduces the additional degrees of freedom required to model the discontinuity, thereby making the approach more efficient in terms of the needed computational resources.

One can foresee that for realistic structural problems this technique will prove to be more efficient as compared to the interface element approach. Placement of the zero thickness elements, *i.e.*, the interface elements proves to be a challenge in simple test configurations itself. X-FEM is implemented using an eight-noded quadrilateral isoparametric element. FORTRAN and MATLAB have been integrated to develop a complete package for X-FEM including the graphics which are being plotted using a FORTRAN code.

## 7.2 Future Work

In this section future research on the stochastic response of the adhesive properties, and extension of the X-FEM approach to incorporate multiple cracks, crack branching, rate dependency of adhesive materials, and analysis of composite materials are suggested.

### 7.2.1 Stochastic Response

As was shown throughout this dissertation, the interfacial material properties such as $T_c$, $G_c$, and $\beta$ may significantly affect the structural response. In most cases, one cannot

obtain the interfacial material properties, since these data as given in the literature are limited and incomplete. Hence, usually, the material properties are assumed based on the strength limits of the bulk material. For this reason, it is suggested that a stochastic analysis of the fracture process be conducted with statistical variations of the interfacial strength, critical energy release rate, and brittleness factor. Using the Stochastic Finite Element Method (SFEM), Kleiber and Hein (1992), as well as Polynomial Chaos (PC), Ghanem and Spanos (2003), Mulani *et al.* (2005b), and Mulani *et al.* (2005a), probabilistic crack growth behavior can be predicted. In the analysis, the interfacial material properties can be described by a Weibull or Gaussian distribution.

### 7.2.2 Extended Finite Element Method

Currently the X-FEM approach is implemented for plane strain conditions with a single crack propagating through the structure. Quite often, for realistic structures there can be more than one crack propagating through it. Also, it is possible for the crack tip to branch at a certain point and propagate through two different paths simultaneously. To extend the current approach, the criterion for the crack propagation (*i.e.*, the principal stress or the von-Mises stress) should not only be monitored in the element in front of the crack tip, but it should be monitored in a radial zone comprised of many elements in front of the crack tip.

The crack growth in polymer based adhesives is very sensitive to the loading rate, as

shown in this study. Rate dependent models formulated in this study can be incorporated in the X-FEM approach along with other models available in the literature to create a general purpose code to analyze any polymer-based adhesive. The inclusion of the rate dependency and multiple crack paths would also allow the prediction of unstable and stable crack growths.

Furthermore, the X-FEM approach can be extended to analyze the complex failure modes in composites. Interlaminar stresses must be predicted precisely, to incorporate the delamination failure mode. Prediction of the interlaminar stresses is a field of research all by itself and there has been tremendous progress in this field over the last few years. Two sets of Heaviside functions could be used to achieve the modeling of failure modes in composites. The additional discontinuity would be introduced due to the formation of two sub-laminates after delamination. Since the crack path can go through the elements, matrix/fiber failure can also be modeled using the X-FEM approach. The interface element approach to study composites is very tedious to model and also computationally very expensive.

# Bibliography

Al Galib, D. and A. Limam (2004). Experimental and numerical investigation of static and dynamic axial crushing of circular aluminum tubes. *Thin-Walled Structures, 42*, 1103–1137.

Alfaiate, J., A. Simone, and L. J. Sluys (2003). Non-homogeneous displacement jumps in strong embedded discontinuities. *International Journal of Solids and Structures, 40*, 5799–5817.

Alfaiate, J., G. N. Wells, and L. J. Sluys (2002). On the use of embedded discontinuity elements with crack path continuity for mode-I and mixed mode fracture. *Engineering Fracture Mechanics, 69*, 661–686.

Allix, O. and A. Corigliano (1999). Geometrical and interfacial nonlinearities in the analysis of delamination in composites. *International Journal of Solids and Structures, 36*, 2189–2216.

Allix, O. and P. Ladevèze (1992). Interlaminar interface modelling for the prediction of delamination. *Composite Structures, 22*, 235–242.

Ashcroft, I. A., D. J. Hughes, and S. J. Shaw (2001). Mode I fracture of epoxy boned

composite joints: 1 quasi-static loading. *Composite Structures, 21*, 87–89.

ASTM (1999). Standard test method for fracture strength in cleavage of adhesives in bonded metal joints. *ASTM D3433,*, 228–234.

Atkins, A. G., C. S. Lee, and R. M. Caddell (1975). Time-temperature dependent fracture toughness of PMMA Part 2. *Journal of Materials Science, 10*, 1394–1404.

Aubery, D. W., G. N. Welding, and T. Wong (1969). Failure mechanisms in peeling in pressure-sensitive adhesive tape. *Journal of Applied Polymer Science, 13*, 2193–2207.

Aubrey, D. W. (1978). Viscoelastic basis of peel adhesion. Volume 222, pp. 191–205. Adhesion 3, Edited by K. W. Allen, Applied Science, London,.

Barenblatt, G. I. (1962). The mathematical theory of equilibrium of cracks in brittle fracture". *Advances in Applied Mechanics, 9*, 55–129.

Beer, G. (1985). An isoparametric joint/interface element for the finite element analysis". *International Journal for Numerical Methods in Engineering, 21*, 585–600.

Belytschko, T., Y. Y. Lu, and L. Gu (1994). Element-free Galerkin methods. *International Journal for Numerical Methods in Engineering, 37*, 229–256.

Béquelin, P. and H. H. Kausch (1995). A technique for studying the fracture of polymers from low to high loading rate. *Impact and Dynamic Fracture of Polymers and Composites J. G. Williams and A. Pavan, eds., Mechanical Engineering Publications Limited, London,*, 3–19.

Bilek, Z. and S. Burns (1974). Crack propagation in wedged double cantilevered beam specimens. *Journal of the Mechanics and Physics of Solids, 22*, 85–95.

Bishop, A., M. Navaratnam, R. D. Rawlings, and H. B. McShane (1993). Functionally gradient material produced by a power metallurgical process. *Journal of Materials Science Letters, 12*, 1516–1518.

Blackman, B., J. Dear, A. Kinloch, H. Macgillivray, Y. Wang, J. Williams, and P. Yayla (1995). The failure of fibre composites and adhesively bonded fibre composites under high rates of test. Part I Mode I loading experimental studies. *Journal of Materials Science, 30*, 5885–5900.

Blackman, B., J. Dear, A. Kinloch, H. Macgillivray, Y. Wang, J. Williams, and P. Yayla (1996). The failure of fibre composites and adhesively bonded fibre composites under high rates of test. Part III: Mixed-mode I/II and mode II loadings. *Journal of Materials Science, 31*, 4467–4477.

Blackman, B., A. Kinloch, Y. Wang, and J. Williams (1996). The failure of fibre composites and adhesively bonded fibre composites under high rates of test. Part II: Mode I loading-dynamic effects. *Journal of Materials Science, 31*, 4451–4466.

Cantwell, W. J. and S. J. Youd (1997). Rate effects in the fracture of glass fibre chopped strand mat composites. *Composites:Part B 28*, 635–640.

Chang, F. K. and K. Y. Chang (1987). A progressive damage model for laminate composites containing stress concentrations. *Journal of Composite Materials, 21*,

834–855.

Chen, J., M. Crisfield, A. Kinloch, E. Busso, F. Matthews, and Y. Qiu (1999). Predicting progressive delamination of composite material specimens via interface elements". *Mechanics of Composite Materials and Structures, 6*, 301–317.

Corigliano, A. and S. Mariani (2001). Parameter identification of a time-dependent elastic-damage interface model for the simulation of debonding in composites. *Composites Science and Technology, 61*, 191–203.

Corigliano, A. and S. Mariani (2002). Identification of a constitutive model for the simulation of time-dependent interlaminar debonding processes in composites. *Computer Methods in Applied Mechanics and Engineering, 191*, 1861–1894.

Corigliano, A., S. Mariani, and A. Pandolfi (2003). Numerical modeling of rate-dependent debonding processes in composites. *Composite Structures, 61*, 39–50.

Corigliano, A. and M. Ricci (2001). Rate-dependent interface models: formulation and numerical applications. *International Journal of Solids and Structures, 38*, 547–576.

Danyluk, M. J., P. H. Geubelle, and H. H. Hilton (1998). Two-dimensional dynamic and three-dimensional fracture in viscoelastic materials. *International Journal of Solids and Structures, 35*, 3831–3853.

de Borst, R. (2003). Numerical aspects of cohesive-zone models. *Engineering Fracture Mechanics, 70*, 1743–1757.

de Borst, R. and J. Rots (1989). Occurrence of spurious mechanisms in computations

of strain-softening solids. *Engineering Computations, 6*, 271–280.

Dugdale, D. S. (1960). Yielding of steel sheets containing slits. *Journal for the Mechanics and Physics of Solids, 8*, 100–104.

Durate, C. A. and J. T. Oden (1996). H-p clouds: an h-p meshless method. *Numerical Methods for Partial Differential Equations, 12*, 673–705.

Eckold, G. (1994). Design and manufacture of composite structures. *McGraw-Hill, NY.*.

Farley, G. and R. Jones (1992). Crushing characteristics of continous fibre-reinforced composite tubes. *Journal of Composite Materials, 26*, 37–50.

Fineberg, J., S. P. Gross, M. Marder, and H. L. Swinney (1991). Instability in dynamic fracture. *Physics Review Letters, 67*, 457–460.

Fineberg, J., S. P. Gross, M. Marder, and H. L. Swinney (1992). Instability in the propagation of fast cracks. *Physics Review, 45*, 5146–5154.

Fleming, M., Y. A. Chu, B. Moran, and T. Belytschko (1997). Enriched element-free Galerkin methods for crack tip fields. *International Journal for Numerical Methods in Engineering, 40*, 1483–1504.

Gardon, J. L. (1963). Peel adhesion. I. Some phenomenological aspects of the test. *Journal of Applied Polymer Science, 7*, 625–641.

Ghanem, R. G. and P. D. Spanos (2003). Stochastic finite elements. A spectral approach. *Dover Publications,*.

Goyal, V., N. Jaunky, E. Johnson, and D. Ambur (2002). Intralaminar and interlaminar progressive failure analyses of composite panels with circular cutouts. In *Proceedings of the 43rd AIAA/ASME/ASCE/AHS/ASC Structures, Structural Dynamics, and Materials Conference, April 22-25, 2002, Paper AIAA-2002-1745*.

Goyal, V., E. Johnson, C. Dávila, and N. Jaunky (2002). An irreversible constitutive law for modeling the delamination process Using Interface Elements. In *Proceedings of the 43rd AIAA/ASME/ASCE/AHS/ASC Structures, Structural Dynamics, and Materials Conference, April 22-25, 2002, Paper AIAA-2002-1576*.

Goyal, V. K. (2002). Analytical modeling of the mechanics of nucleation and growth of cracks. Ph.D. Thesis, Virginia Polytechnic Institute and State University, Blacksburg, VA.

Goyal-Singhal, V. and E. Johnson (2001). Computational issues in modeling the delamination process using interface finite elements. In *Proceedings of the American Society for Composites, 16th Technical Conference, (9-12 September 2001, Blacksburg, VA) Technomic Publishing Co., Inc., Lancaster PA*.

Hakeem, M. I. and M. G. Phillips (1979). Unstable crack propagation: A fractographic study using PMMA in liquid environments. *Journal of Materials Science, 14*, 2901–2905.

Hilber, H. M., T. J. R. Hughes, and R. Taylor (2001). Mixed-mode fracture analyses of plastically-deforming adhesive joints. *International Journal of Fracture, 110*, 175–187.

Hull, D. (1991). A unified approach to progressive crushing of fibre-reinforced tubes. *Composites Science and Technology, 40*, 377–421.

Jirásek, M. and Z. P. Bažant (2002). Inelastic Analysis of Structures. *John Wiley and Sons, New York*.

Kim, K. S. and J. Kim (1988). Elasto-plastic analysis of the peel test for thin film adhesion. *Journal of Engineering Materials and Technology, 110*, 266–273.

Kinloch, A. J. and J. G. Williams (1980). Crack blunting mechanisms in polymers. *Journal of Materials Science, 15*, 987–996.

Kinloch, A. J. and M. L. Yuen (1989a). The mechanical behavior of polyimide-copper laminates Part I: locus of failure studies. *Journal of Materials Science, 24*, 2183–2190.

Kinloch, A. J. and M. L. Yuen (1989b). The mechanical behavior of polyimide-copper laminates Part II: peel energy measurements. *Journal of Adhesion, 30*, 151–170.

Kirugulige, M. S., R. Kitey, and H. V. Tippur (2005). Dynamic fracture behavior of model sandwich structures with functionally graded core: a feasibility study. *Composites Science and Technology, 65*, 1052–1068.

Kleiber, M. and T. D. Hein (1992). The stochastic finite element method, basic perturbation technique and computer implementation. *John Wiley & Sons, New York,*.

Knauss, W. G. (1973). On the steady propagation of a crack in a viscoelastic sheet: Experiments and analysis. Deformation and Fracture of High Polymers. Kausch,

H.H. and Jaffe, R. (Eds.). Plenum Press, New York, 501541.

Knauss, W. G. (1974). On the steady propagation of a crack in a viscoelastic sheet: Experiments and analysis. In *Deformation and Fracture of High Polymers (Edited by H. H. Kausch et. al.), Plenum Press, New York.)*, pp. 501–541.

Kobayashi, T. and J. W. Dally (1977). Relation between crack velocity and the stress intensity factor in birefringent polymers. In *Fast Fracture and Crack Arrest ASTM STP 627*, pp. 257–273.

Kubair, D. V., P. H. Geubelle, and Y. Y. Huang (2003). Analysis of a rate-dependent cohesive model for dynamic crack propagation. *Engineering Fracture Mechanics, 70*, 685–704.

Landis, C. M., T. Pardoen, and J. W. Hutchinson (2000). Crack velocity dependent toughness in rate dependent materials. *Mechanics of Materials, 32*, 663–678.

Lankford, J. (1981). Mechanisms responsible for strain-rate dependent compressive strength in ceramic materials. *Journal of the American Ceramic Society, 64*, 33–34.

Leevers, P. S. (1986). Crack front shape effects on propagation stability in thermosetting polyesters. *Theoretical and Applied Fracture Mechanics, 6*, 45–55.

LS-DYNA (2003). LS-DYNA Theory Manual Version 970. *Livermore Software Technology Corporation, Livermore, CA*.

Malvern, L. (1969). Introduction to the mechanics of continuous medium.

Mamalis, A. G., D. E. Manolakos, M. B. Ioannidis, and D. P. Papapostolou (2005). The static and dynamic axial collapse of CFRP square tubes: Finite element modelling. *Composite Structures, In Press*.

Mataga, P. A., L. B. Freund, and J. W. Hutchinson (1987). Crack tip plasticity in dynamic fracture. *Journal of the Physics and Chemistry of Solids, 11*, 985–1005.

Maugis, D. and M. Barquins (1987). Stick-slip and peeling of adhesive tapes. Volume 12, pp. 205–222. Adhesion, edited by K. W. Allen, Applied Science, London.

Melenk, J. M. and I. Babuska (1996). The partition of unity finite element method: Basic theory and applications. *Computer Methods in Applied Mechanics and Engineering, 139*, 289–314.

Mi, Y., M. A. Crisfield, and G. A. O. Davies (1998). Progressive delamination using interface elements. *Journal of Composite Materials, 32*, 1246–1272.

Moës, N. and T. Belytschko (2002). Extended finite element method for cohesive crack growth. *Engineering Fracture Mechanics, 69*, 813–833.

Moës, N., J. Dolbow, and T. Belytschko (1999). A finite element method for crack growth without remeshing. *International Journal for Numerical Methods in Engineering, 46*, 131–150.

Mulani, S. B., R. K. Kapania, and R. W. Walters (2005a). Stochastic eigenvalue problem with polynomial chaos. *AIAA Journal, Under Review*.

Mulani, S. B., R. K. Kapania, and R. W. Walters (2005b). Stochastic fundamental

eigenvalue problem with polynomial chaos. *AIAA Journal, Under Review*.

Needleman, A. (1987). A continuum model for void nucleation by inclusion debonding. *Journal of Applied Mechanics, 54*, 525–531.

Needleman, A. (1990a). An analysis of decohesion along an imperfect interface. *International Journal of Fracture, 42*, 21–40.

Needleman, A. (1990b). An analysis of tensile decohesion along an interface. *Journal of the Mechanics and Physics of Solids, 38*, 289–324.

Nemes, J. A. and P. W. Randles (1994). Constitutive modeling of high strain-rate deformation and spall fracture of graphite / peek composites. *Mechanics of Materials, 19*, 1–14.

Ortiz, M. and A. Pandolfi (1999). Finite - deformation irreversible cohesive elements for three - dimensional crack - propagation analysis. *International Journal for Numerical Methods in Engineering, 44*, 1267–1282.

Parameswaran, V. and A. Shukla (2000). Processing and characterization of a model functionally gradient material. *Journal of Materials Science, 35*, 21–29.

Phillips, D. C., J. M. Scott, and M. Jones (1978). Crack propagation in an amine-cured epoxide resin. *Journal of Materials Science, 13*, 311–322.

Plummer, C. J. G., M. Mauger, P. Béquelin, and J. Varlet (2004). Fracture resistance of mineral reinforced polyamide 6. *Polymer, 45*, 1147–1157.

Popelar, C. H. and M. F. Kanninen (1980). A dynamic viscoelastic analysis of crack

propagation and crack arrest in a double cantilever beam testing specimen. Crack Arrest Methodology and Applications. American Society of Testing and Materials, ASTM STP 711, Philadelphia, 5-23.

Potter, K. D. (2001). Heavily loaded bonded composite structure: Design, manufacture and test of 'I' beam specimens. *Composite Structures, 51*, 389–399.

Rahul-Kumar, P., A. Jagota, S. J. Bennison, and S. Saigal (2000a). Cohesive element modeling of viscoelastic fracture application to peel testing of polymers. *International Journal of Solids and Structures, 37*, 1873–1897.

Rahul-Kumar, P., A. Jagota, S. J. Bennison, and S. Saigal (2000b). Interfacial failures in a compressive shear strength test of glass/polymer laminates. *International Journal of Solids and Structures, 37*, 7281–7305.

Rahul-Kumar, P., A. Jagota, S. J. Bennison, S. Saigal, and S. Muralidhar (1999). Polymer interfacial fracture simulations using cohesive elements. *Acta Materialia, 47*, 4161–4169.

Ravi-Chandar, K. and M. Balzano (1988). On the mechanics and mechanisms of crack growth in polymeric materials. *Engineering Fracture Mechanics, 30*, 713–727.

Rice, J. (1978). The mechanics of quasi-static crack growth. In *Proceedings of the 8th U.S. National Congress on Mechancis)*, pp. 191–216.

Rose, J. H., J. Ferrante, and R. J. Smith (1981). Universal binding energy curves for metals and bimetallic interfaces . *Physical Review Letters, 47*, 675–678.

Schlangen, E. (1993). Experimental and numerical analysis of fracture processes in concrete. *PhD Thesis, Delft University of Technology,*.

Scott, J. M., G. M. Wells, and D. C. Phillips (1980). Low temperature crack propagation in epoxide resin. *Journal of Materials Science, 15*, 1436–1448.

Selby, K. and L. E. Miller (1975). Fracture toughness and mechanical behavior of an epoxy resin. *Journal of Materials Science, 10*, 12–24.

Simón, J. C. (2004). Response and failure of adhesively bonded automotive composite structures under impact loads. M.S. Thesis Virginia Polytechnic Institute and State University, Blacksburg, VA.

Simone, A., H. Askes, H. J. Peerlingsd, and L. J. Sluys (2003). Interpolation requirements for implicit gradient-enhanced continuum damage models. *Communications in Numerical Methods in Engineering, 19*, 563–572.

Simone, A., G. N. Wells, and L. J. Sluys (2003). From continuous to discontinuous failure in a gradient-enhanced continuum damage model. *Computer Methods in Applied Mechanics and Engineering, 192*, 4581–4607.

Singh, R. P. and V. Parameswaran (2003). An experimental investigation of dynamic crack propagation in a brittle material reinforced with a ductile layer. *Optics and Lasers in Engineering, 40*, 289–306.

Tsai, S. W. and E. M. Wu (1971). A general theory of strength for anisotropic materials. *Journal of Composite Materials, 5*, 58–80.

Wang, S. (1980). An analysis of delamination in angle-ply fiber reinforced composites. *Journal of Applied Mechanics, 47*, 64–70.

Webb, T. W. and E. C. Aifantis (1995). Oscillatory fracture in polymeric materials. *International Journal of Solids and Structures, 32*, 2725–2743.

Wells, G. N. and L. J. Sluys (2001a). A new method for modelling cohesive cracks using finite elements. *International Journal for Numerical Methods in Engineering, 50*, 2667–2682.

Wells, G. N. and L. J. Sluys (2001b). Discontinous analysis of softening solids under impact loading. *International Journal for Numerical and Analytical Methods in Geomechanics, 25*, 691–709.

Wells, G. N., L. J. Sluys, and R. de Borst (2002). Simulating the propagation of displacement discontinuities in a regularized strain softening material. *International Journal for Numerical Methods in Engineering, 53*, 1235–1256.

Wu, C. (1987). Nonlinear analysis of edge effects in angle-ply laminates. *Computers and Structures, 25*, 1093–1104.

Xu, C., T. Siegmund, and K. Ramani (2003a). Rate-dependent crack growth in adhesives, I. Modeling approach. *International Journal of Adhesion and Adhesives, 23*, 9–13.

Xu, C., T. Siegmund, and K. Ramani (2003b). Rate-dependent crack growth in adhesives, II. Experiment and analysis. *International Journal of Adhesion and Adhe-*

*sives, 23*, 15–22.

Xu, X.-P. and A. Needleman (1993). Void nucleation by inclusion debonding in a crystal matrix. *Modelling and Simulation in Materials Science and Engineering, 1*, 111–132.

Xu, X.-P. and A. Needleman (1994). Numerical simulations of fast crack growth in brittle solids. *Journal of the Mechanics and Physics of Solids, 42*, 1397–1434.

Xu, X.-P. and A. Needleman (1995). Numerical simulations of dynamic interfacial crack growth allowing for crack growth away from the bond line. *International Journal of Fracture, 74*, 253–275.

Xu, X.-P. and A. Needleman (1996). Numerical simulations of dynamic crack growth along an interface. *International Journal of Fracture, 74*, 289–324.

Yamini, S. and R. J. Young (1977). Stability of crack propagation in epoxy resins. *Polymer, 18*, 1075–1080.

Zhang, X., H. Liu, and Y. Mai (2003). Rate-dependent bridging law and its application to dynamic crack growth in brittle-matrix composite materials. *Composites:Part A In Press.*

Zhang, X., Y. Mai, and R. G. Jeffrey (2003). A cohesive plastic and damage zone model for dynamic crack growth in rate-dependent materials. *International Journal of Solids and Structures, 40*, 5819–5837.

# Vita

Dhaval Pravin Makhecha was born in Pune, Maharashtra, India on the $8th$ of May 1977. He completed his primary and secondary education from S.M. Choskey High School, Pune in 1992. He pursued his Diploma in Civil Engineering and later Bachelor's degree in Civil Engineering from Bharathi Vidyapeth, Pune University and completed his Bachelor's degree in 1998. Dhaval started his graduate studies in Civil Engineering (Structures) at Pune University in 1998. During the first semester he was accepted as a Senior Research Fellow at the Institute of Armament Research (IAT) a national lab under the Defense Research and Development Organization (DRDO). The thesis research conducted at IAT under the guidance of Dr. Manickam Ganapathi involved analysis of composite structures under thermo-mechanical loading. He defended his Master's thesis in the Spring of 2000 and continued to work in IAT. Doctoral studies began in the Fall of 2001 under the guidance of Dr. Rakesh Kapania at the Aerospace and Ocean Engineering Department at Virginia Tech. While pursuing his PhD he has taught the senior design lab and the Vibrations and Control course.